# DOCTOR OF PHILOSOPHY

## Advanced fibre-based endoscopy for biophotonics applications

Oliveira Teixeira Leite, Ivo Jorge

*Award date:*
2018

UNIVERSITY OF DUNDEE

DOCTORAL THESIS

---

# Advanced fibre-based endoscopy for biophotonics applications

---

*Author:*
Ivo Teixeira LEITE

*Supervisors:*
Prof. Tomáš ČIŽMÁR
Prof. Sir Alfred CUSCHIERI

*A thesis submitted in fulfillment of the requirements for the degree of Doctor of Philosophy*

*in the*

Complex Photonics Group
School of Science and Engineering

November 2018

# Declaration of Authorship

I, Ivo Teixeira LEITE, declare that this Thesis titled, "Advanced fibre-based endoscopy for biophotonics applications" and the work presented in it are my own. I confirm that:

- This work was done wholly or mainly while in candidature for a research degree at this University.
- Where any part of this Thesis has previously been submitted for a degree or any other qualification at this University or any other institution, this has been clearly stated.
- Where I have consulted the published work of others, this is always clearly attributed.
- Where I have quoted from the work of others, the source is always given. With the exception of such quotations, this Thesis is entirely my own work.
- I have acknowledged all main sources of help.
- Where the Thesis is based on work done by myself jointly with others, I have made clear exactly what was done by others and what I have contributed myself.

Signed:

Date: 16-Nov-2018

*"A vida é o que fazemos dela. As viagens são os viajantes. O que vemos, não é o que vemos, senão o que somos."*

Fernando Pessoa, *Livro do Desassossego*

*"Life is whatever we make it. The traveler is the journey. What we see is not what we see but who we are."*

Fernando Pessoa, *The Book of Disquiet*

UNIVERSITY OF DUNDEE

# *Abstract*

School of Science and Engineering

Doctor of Philosophy

**Advanced fibre-based endoscopy for biophotonics applications**

by Ivo Teixeira LEITE

Despite the tremendous advances witnessed in light microscopy over the past two decades, non-invasive optical imaging is still limited to penetration depths smaller than 1 mm into tissue. Multiple scattering caused by the refractive index inhomogeneities of biological matter rapidly distort any optical wavefront propagating through, rendering tissues opaque. Such turbidity restricts imaging, as well as other biophotonics techniques, to the most superficial layers of tissue.

A perspective strategy to overcome the turbidity of living matter exploits holographic light control in multimode optical fibres. This allows devising minimally invasive imaging probes with footprints far bellow those of conventional endoscopes, as well as enhanced spatial resolution up to the diffraction limit determined by the numerical aperture (NA) of the fibre.

In this Thesis, high-resolution focussing is demonstrated with unprecedented ability across novel specialty fibres offering very-high NAs, by devising a system and methodologies which allow counteracting the severe mode-dependent loss affecting such fibres. The high quality and NA of the generated foci is capable of 3D optical confinement of dielectric microparticles, thus enabling the delivery of holographic optical tweezers introduced through a bare optical fibre with cross-section comparable to a single cell. The holographic methods developed allow the manipulation of complex 3D arrangements of particles, as well as their independent positioning with nanometre-scale precision in all three dimensions.

Separately, a multimode fibre based deep-brain fluorescence imaging is demonstrated in animal models *in vivo*, allowing the identification of neuronal structures at depths exceeding 2 mm and resolving fine details down to $\approx$1 µm resolution.

# *Acknowledgements*

I wish to address my deepest gratitude to all my colleagues, friends, and family who contributed directly or indirectly to the realisation of this work.

First, I would like to thank my main supervisor, Prof. Tomáš Čižmár, for his invaluable mentorship and for setting the highest standards, both personal and professional alike, for the scientist I aspire to become. The general guidance and support from Prof. Sir Alfred Cuschieri, my second supervisor, were also greatly appreciated.

I wish to acknowledge everyone involved in the PHOQUS Initial Training Network programme for having provided outstanding conditions for my doctoral studies. In particular, I would like to thank the project coordinator, Prof. Kees Weijer, project managers Ms. Wendy Phillips and Mrs. Janette Moore, and the extraordinary group of PhD students which I am proud to have been part of.

A special thanks to Sergey, with whom I spent two years in the lab and in the office. We embarked in this journey together, and together we experienced the full spectrum of emotions over failed and successful attempts in our work.

I would also like to acknowledge the influential role played by others at earlier stages of my path: Dr. María-Cruz Navarrete and Dr. Natalia Díaz-Herrera at the Complutense University of Madrid, Prof. José Luís Santos, Dr. Ariel Guerreiro, Dr. Pedro Jorge, Dr. José Miguel Teixeira, and Dr. Aurelio Hierro Rodriguez at the University of Porto and INESC TEC, and Prof. Edik Rafailov and Dr. Andrei Gorodetsky at Aston University. All of you made me want to take my journey through Science further.

The wonderful friends I was lucky to find in Scotland made everything easier. Thank you, Daniel, Filipa, Galli, Lale, Nuno, Olivia, Piotr, Salvo, Sascha, Sebi, Sergey, Valentina, Valerie, Tom, Tushar, Ty, and Vrushali. A special word of gratitude goes to my extended family in Dundee – Joana, Pedro Ernesto, Ricardo and Rosinha – for being precisely this.

Lastly, I wish to thank my Family for the loving support I have always received. In particular my parents, Fernanda and Jorge, as well as Augusta. My successes are also yours.

And thank you Patrícia, for loving me back.

Jena, 16$^{th}$ July 2018,
Ivo

# Contents

# List of Figures

# List of Abbreviations

| | |
|---|---|
| **CCD** | **C**harge-**c**oupled **D**evice |
| **DMD** | **D**igital **M**icromirror **D**evice |
| **FFT** | **F**ast **F**ourier **T**ransform |
| **FP** | **F**ocal **P**oint |
| **HOT** | **H**olographic **O**ptical **T**weezers |
| **LC-SLM** | **L**iquid-**c**rystal-based **S**patial **L**ight **M**odulator |
| **LED** | **L**ight-**e**mitting **D**iode |
| **MDL** | **M**ode-**d**ependent **L**oss |
| **MEMS** | **M**icro-**e**lectro-**m**echanical **S**ystems |
| **MMF** | **M**ulti**m**ode **F**ibre |
| **NA** | **N**umerical **A**perture |
| **PC** | **P**rincipal **C**omponent |
| **PCA** | **P**rincipal **C**omponent **A**nalysis |
| **PR** | **P**ower **R**atio |
| **PSD** | **P**ower **S**pectral **D**ensity (function) |
| **SLM** | **S**patial **L**ight **M**odulator |
| **TM** | **T**ransmission **M**atrix |

*Às minhas Avós,*
*Maria de Lurdes e Maria Eduarda*

# Chapter 1

# Introduction

This chapter situates the Thesis in the broader context of biomedical imaging, and provides an overview of the topics onto which it builds upon. Additionally, it lays out the aims and objectives of the present work and summarises the structure of the Thesis.

The contents of this chapter partially comprise the review article: S. Turtaev, **I. T. Leite**, and T. Čižmár, *Multimode fibres for micro-endoscopy*, Optofluidics Microfluidics and Nanofluidics 2, 31–35 (2015).

## 1.1 Motivation

Optical, or light, microscopy has become an ubiquitous technology in the Life and Biomedical sciences since the seventeenth century. As the main driver of modern Biology, it opened the door to the discovery of the cell and bacteria, and later the study of sub-cellular structures. Optical microscopes were the highest resolution imaging tools available until the advent of electron microscopy in the early 1930s. Nevertheless, light microscopy did not lose in popularity, still remaining today as the primary technology for observations in the Life Sciences. There are, of course, good reasons for this. Optical microscopy can provide quantitative information, yields high sensitivities down to the femtomolar scale and offers a plethora of endogenous and exogenous contrast mechanisms (e.g. fluorescence and Raman), all combined with very high spatial resolutions [1, 2]. Very importantly, it is compatible with studies of living matter *in vivo* and *in vitro* at several scales from cells to tissues and organisms, owing to the possibility of maintaining the samples in physiological conditions and by using non-ionising radiation.

Observations using light are, however, typically limited to the most superficial layers of living tissues or to thin, transparent samples of fixed tissue analysed by histology. The high complexity of most biological tissues, with inhomogeneities in refractive index at all length scales, gives rise to multiple scattering which rapidly degrades the optical wavefronts, rendering tissues turbid, or opaque. Techniques such as confocal and multi-photon microscopies, as well as optical coherence tomography, can reject this undesired scattered light and select only the non-interacting photons which remained unaffected by scattering. The proportion of such *ballistic* photons decays exponentially with tissue depth (Beer-Lambert law) with a characteristic length corresponding to the mean free path of the photons – i.e. their average distance travelled between two consecutive scattering events. For most tissues, this mean free path lies typically in the order of 50–100 µm for visible and near-infrared light [3].

The mean free path of photons is larger for longer wavelengths, meaning that they can penetrate deeper into tissue. However, the attainable diffraction-limited spatial resolution will be proportionally smaller. Interestingly, this seems to give rise to a trade-off between penetration depth and achievable spatial resolution affecting all commonly employed non-invasive techniques which allow *in-vivo* investigations [2–4], as revealed by Fig. 1.1. As a rule of thumb, most non-invasive imaging methods allow resolving details around two orders of magnitude smaller than the imaging depth. In the optical realm, remarkably, a few techniques can slightly escape this trend. Multiphoton microscopy is capable of increased penetration depths up to 1 mm owing to the deeper penetration of longer wavelengths combined with optical sectioning arising from the non-linear probability of two- or three-photon absorption [5–8], while a variety of super-resolution techniques is able to exceed the resolution of diffraction limit and observe life at the molecular level [9–12]. Still, an immense technological gap separates us from undertaking detailed sub-cellular observations at centimetres of depth.

A new strategy has emerged in the last decade, taking inspiration in the principles of adaptive optics from astronomy, to harness the scattered photons. Even though extremely complex, scattering is a deterministic and linear process and as such does not destroy coherence, even in the highly- or multiple-scattering regime [2]. By controlling the spatial modes of a wavefront by means of digital holography using a spatial light modulator (SLM), it is possible to manipulate coherent light across distances within highly-scattering media far exceeding the photons' mean free path, to create diffraction-limited foci [13, 14] or transmit images [15, 16]. This gave rise to a new discipline in the domain of Optics, so-called

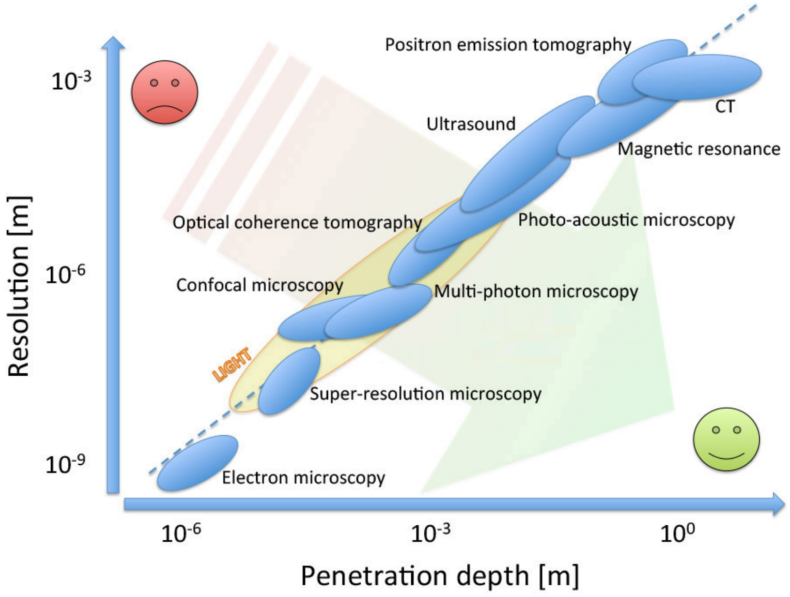


FIGURE 1.1: Trade-off between depth of penetration and attainable spatial resolution for some of the most widespread non-invasive biomedical imaging technologies. Figure reproduced from [4].

*photonics of complex media*. However, focussing (or in general, controlling) light inside such turbid media requires some sort of feedback from within acting as a *guide star* – a term which remains from its origins. Despite significant progress in this direction in recent years [17], e.g. exploiting combinations with photoacoustics [18, 19], completely non-invasive imaging at depth still lies in the distant future [2, 4].

The alternative imaging approaches rely on the use of endoscopes, slender instruments transmitting images from remote, hardly-accessible locations. Rigid endoscopes are generally comprised of large rod-lenses to relay images between its two extremities, an improvement introduced by Harald Hopkins to the previous designs based on numerous relay lenses [20, 21]. Flexible endoscopes (*fiberscopes*) on the other hand, rely on image transfer through flexible fibre bundles – a concept first demonstrated also by Hopkins [22]. These are typically combined with a micro-objective lens or gradient-index lens that creates an image on the facet of the fibre bundle; there it is separated into individual guiding cores that transport light to the opposite extremity where the image can be observed or recorded. Nevertheless, the instrument footprint in both cases is rarely below 1 mm, which is far too large to be introduced deep inside the most sensitive tissues, particularly in scientific research using awake animal models.

A perspective approach for devising ultra-narrow endoscopes has recently emerged, exploiting hair-thin multimode optical fibres as the image-guiding medium [23–25]. Multimode fibres (MMFs) can be made with diameters in the order of tens of micrometres, thus reducing the instrument footprint by orders of magnitude. However, light propagation in MMFs is a complex and often unpredictable process. An incident optical field is coupled into its many waveguide modes, all of which propagate with different phase velocities and that can also couple between each other through imperfections or bending of the fibre. The resulting output field is a superposition of such modes, which now feature complex and unpredictable phase relations, and in general bears no resemblance to the initial field. This leads to the degradation beyond recognition of any image transmitted through distances as small as hundreds of micrometres. Although originating from a different physical mechanism, such turbid behaviour shares much from that of highly-scattering media introduced above. In both cases, the apparently randomising process is linear and deterministic; as such, the same strategies for wavefront shaping can be employed to control the spatial modes of the transmission medium. Importantly however, in a MMF one generally has access to both the input and output fields when characterising the light propagation prior to its implantation within a sample, thus obviating the need for a guide star.

Holographic control of light propagation in MMFs has allowed demonstrating focussing [26–28] and beam-shaping [23, 27, 29], different modalities of microscopy [23–25, 30–32], as well as micro-fabrication [33, 34] and optical manipulation [27, 35]. Nevertheless, there are still many obstacles in the way before this technology can be routinely found in applications requiring imaging, or other biophotonics techniques, deep inside living tissues. These include, but are not limited to, spatial resolution achievable, imaging speed, flexible operation, and simultaneous control over spatial and temporal dispersion. Addressing these challenges can bring us closer to unravel the mysteries hiding deep within the complexity of living matter.

## 1.2 Fundamental concepts

### 1.2.1 Fibre optics

Optical fibres are narrow, flexible waveguides with diameters usually in the range from 0.1 mm to 1 mm which allow transmitting light signals over long distances – up to hundreds of kilometres – with very little attenuation. They typically have cylindrical symmetry and are made from transparent materials such as glass (most frequently, pure or doped silica) or plastic.

In its simplest and most widespread conception, an optical fibre comprises a homogeneous, cylindrical *core* surrounded by an also homogeneous *cladding* with lower refractive index – this is a so-called *step-index fibre*. In this case, light remains confined to the core region by total internal reflection, without energy transmission to the cladding. The refractive index contrast between the core and cladding materials dictates the maximum spatial frequencies which are allowed to propagate through the fibre. Using the geometrical optics description, the index contrast dictates the maximum propagation angle at which light rays can travel within the core, which has the critical value $\phi_c = \cos^{-1}(n_2/n_1)$ (where $n_1$ and $n_2$ are, respectively, the refractive indices of the core and cladding) as seen directly from Snell's law. This is usually described in terms of the numerical aperture (NA) of the fibre, which defines both the acceptance angle when coupling light into the fibre as well as the divergence of the output beam at the opposite facet. The NA, defined as $n_1 \sin \phi_c$, is then given by:

$$\mathrm{NA} = \sqrt{n_1^2 - n_2^2}, \tag{1.1}$$

and thus depends solely on the choice of the core and cladding materials.

Each propagation angle within the fibre corresponds to a guided mode characterised by a particular spatial distribution of the optical field satisfying the boundary conditions of the waveguide, which correspond to the electromagnetic field being smooth – i.e. continuous and with continuous gradient – across the core-cladding interface. In the ray-optics description, this corresponds to the light rays satisfying a condition of constructive interference between consecutive reflections at the core-cladding boundary. Thus, only a discrete number of guided modes can travel in the fibre with a discrete number of propagation angles, all of which below the critical value. If the refractive contrast and/or the core diameter

are small enough, it may be the case that only one guided mode – the *fundamental mode* – in each orthogonal polarisation state is sustained by the fibre. In such case, the fibre is termed *single-mode fibre*, and it can be shown that single-mode operation occurs for $v \lesssim 2.405$, where $v = k_0 a\mathrm{NA}$ is called the *reduced frequency* or $v$-number ($k_0$ is the wavenumber in free space and $a$ is the core radius) [36, 37]. When $v \gtrsim 2.405$, the fibre sustains more than one guided mode, and is thus called *multimode fibre*. For $2.405 \lesssim v \lesssim 10$, an optical fibre is sometimes referred to as a *few-mode fibre*. Larger $v$-numbers amount to an increasing number of guided modes. In the limit $v \gg 1$ (in practice, $v \gtrsim 20$), the number of modes sustained by the fibre is approximately given by $N \simeq v^2/2$, including both orthogonal polarisation states [36, 37].

By definition, these guided modes (also called *eigenmodes* or *propagation-invariant modes*) preserve their field distributions during transmission through the fibre, and each of them propagates with a distinct phase velocity, or propagation constant[1]. Thus, an eigenmode $\psi_j$ after travelling a distance $z$ in the fibre accumulates a phase $e^{i\beta_j z}$, where $\beta_j$ is its propagation constant. Moreover, it can be shown that the set of fibre eigenmodes forms a complete and orthonormal basis for the fields allowed to propagate in the fibre, which can thus be expressed as $\mathbf{E} = \sum_j E_j \psi_j$. If the optical fields at the input and output of the fibre, $\mathbf{E}_{\mathrm{in}}$ and $\mathbf{E}_{\mathrm{out}}$, are expressed in the basis formed by the fibre eigenmodes, $\psi_j$, then they are related by a diagonal matrix:

$$\begin{bmatrix} E_1^{\mathrm{out}} \\ E_2^{\mathrm{out}} \\ \vdots \\ E_N^{\mathrm{out}} \end{bmatrix} = \begin{bmatrix} e^{i\beta_1 z} & 0 & \cdots & 0 \\ 0 & e^{i\beta_2 z} & \cdots & 0 \\ \vdots & \vdots & \ddots & \vdots \\ 0 & 0 & \cdots & e^{i\beta_N z} \end{bmatrix} \begin{bmatrix} E_1^{\mathrm{in}} \\ E_2^{\mathrm{in}} \\ \vdots \\ E_N^{\mathrm{in}} \end{bmatrix} \tag{1.2}$$

where $E_j^{\mathrm{in}} = \langle \psi_j | \mathbf{E}_{\mathrm{in}} \rangle$ and $E_j^{\mathrm{out}} = \langle \psi_j | \mathbf{E}_{\mathrm{out}} \rangle$ are the coordinates of the input and output field in the basis of fibre eigenmodes.

In a real fibre, inhomogeneities and impurities originating in the fibre manufacturing process, as well as micro- and macro-bends in the fibre conformation, give rise to *mode mixing* in the fibre, i.e. exchange of power between the eigenmodes. This will be represented by non-diagonal elements in the transmission matrix (1.2), leading to highly complex and seemingly unpredictable phase relations between the output modes. Nevertheless, it has been shown recently that given sufficiently accurate knowledge of the parameters of the fibre (including

[1] Their exact field distributions and dispersion equation are derived in Appendix A.

departure from ideal index profile), of the 12 degrees of freedom in alignment, as well as the macro-bending conformation of the fibre, such diagonal transmission matrix can be numerically predicted and adequately describe optical propagation over fibre lengths up to 30 cm [38].

From an experimental perspective, the basis of propagation-invariant modes is not a convenient choice for practical implementations. However, any basis of orthogonal modes of sufficient dimension can be employed; moreover, the input and output modes do not need to be expressed in the same basis. The frequent choice is usually a square grid of diffraction-limited points or truncated plane-waves with different propagation angles, since in the first case they can be made conjugate to individual pixels of a CCD detector or spatial light modulator, or their far-field can be conjugate to the pixels' grid in the latter case. In general, of course, such choice will lead to a non-diagonal transmission matrix of complex values.

### 1.2.2 Photonics of complex media

Complex media, also known as *turbid* or *highly-scattering* media, are materials having refractive index inhomogeneities spanning across the length scales comparable to, or smaller than, the wavelength of light [39]. Light travelling in such a medium is scattered one or multiple times in random directions, rapidly distorting the incident wavefront. Image transmission is lost in this way, and the medium appears opaque. Common examples of complex media include fog, white paint, unfiltered beer (including the foam), and biological tissue.

Soon after high-quality digital diffractive elements became available at the turn of the millennium, various approaches to control multiple light scattering have been developed [40]. They commonly employ spatial light modulators (SLMs) to manipulate the incident wavefront projected on the complex medium in such a way as to achieve a desired output field distribution despite light distortion within the media due to scattering.

First experiments demonstrated the possibility of focussing behind highly-scattering layers by means of a computer-controlled feedback algorithm [13, 14]. This work inspired a multitude of different other wavefront shaping techniques which followed soon after, including iterative methods [41], time reversal or phase conjugation [42], and the transmission matrix approach[43, 44].

Possibly the most well-established method to control light scattering in complex media relies on the empirical acquisition of its transmission matrix (TM).

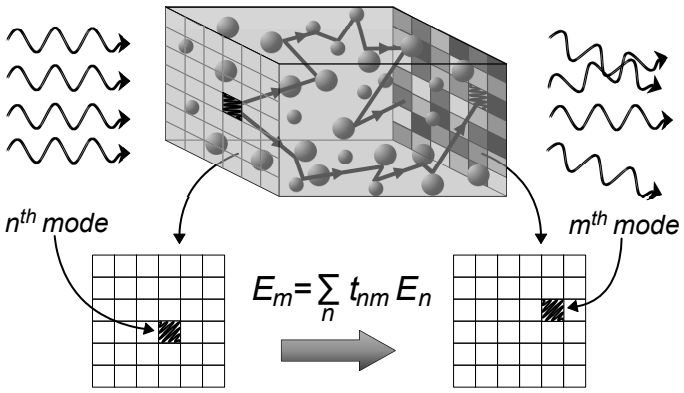


FIGURE 1.2: Wave propagation in complex media. Wavefronts transmitted through a complex, or turbid medium are distorted due to multiple scattering events. The spatial output modes $E_m$ are related to the input modes $E_n$ through a transmission matrix which completely describes optical propagation through the medium.

Since in the majority of cases scattering can be considered a linear process, optical propagation within a complex medium can be described in terms of a matrix of complex coefficients. Arbitrarily complex incident and transmitted fields can be decomposed in sets of input and output orthogonal spatial modes, which are mutually related by the TM, as illustrated schematically in Fig. 1.2. With the knowledge of the TM of the medium, one can simply calculate which phase and amplitude input distributions need to be provided in order to synthesise a desired light output. Images transmitted coherently through complex media are typically scrambled beyond recognition into seemingly random speckle patterns, but the original image can be recovered by deploying the TM [15].

It should be noted, however, that only a small portion of the TM of a complex medium can be acquired in practice. For visible light, the number of transverse modes carrying energy across the medium is in the order of 10 million modes per square millimetre [40], a value by far exceeding the number of spatial degrees of freedom controllable with an SLM. As a consequence, most light remains uncontrolled, thus forming a speckled background.

### 1.2.3 Holographic light control in multimode fibres

When light is launched into a multimode fibre (MMF), the incident optical field is projected onto its numerous waveguide modes, each of which travelling with a different propagation constant (or equivalently, different phase velocity). This

phenomenon is commonly known as *intermodal dispersion*, or simply *modal dispersion*. Moreover, the presence of impurities and inhomogeneities within the fibre, as well as macro or micro-bends, causes these modes to couple to one another and exchange energy – a mechanism called *mode mixing*. Both processes concur to distort the wavefront of the incident field, and upon coherent propagation of just a few hundreds of micrometres the resulting field is a complex speckle pattern bearing little to no resemblance with the initial distribution. Although arising from distinct physical mechanisms, the apparently randomising nature of light propagation in multimode fibres is somewhat analogous to optical transmission through complex media. As such, in most applications MMFs can be regarded as complex media, and the same principles for controlling light propagation by wavefront shaping can be employed. Nevertheless, a few key differences should be emphasised. In an MMF, the number of channels transporting energy across (its waveguide modes) is typically comparable to the number of spatial degrees of freedom controllable with an SLM. Thus, it is in general possible to control the total power propagating through an MMF using complex (i.e. both amplitude and phase) modulation. When only the phase information is used (phase-only modulation), control over only $\pi/4 \simeq 78.5\%$ of the power can be generally achieved [27]; however, special cases exist where this can vary significantly. Additionally, the cylindrical symmetry of MMFs gives rise to both a *rotational memory effect*, where rotating an incident input field precisely around the fibre axis gives rise to a rotated output field by the same amount [45], as well as an *axial memory effect* preserving the axial components of incident wavevectors [23]. The polarisation state is also usually well-preserved in most high-quality MMFs, especially for circularly-polarised light [38].

Analogies of the first wavefront shaping feedback algorithms shown in complex media [26, 27, 35], the empirical measurement of the transmission matrix [23, 24], as well as principles of digital phase conjugation [25, 28] have been successfully exploited for beam-shaping and imaging through MMFs. Fluorescence imaging [23, 25, 35] and micro-manipulation [27, 35] can be performed by scanning a focussed light at the distal end of a MMF, as depicted in Fig. 1.3a. Scanner-free wide-field imaging has also been demonstrated. Here, the acquired TM is used to retrieve the optical field at the distal fibre facet from the speckle pattern, either by physical inversion of the TM using a SLM [23] or by numerical post-processing [24], as depicted in Fig. 1.3b.

Most methods above have only been demonstrated using narrow-band laser light. This, unfortunately, stands in the way of introducing advanced methods of

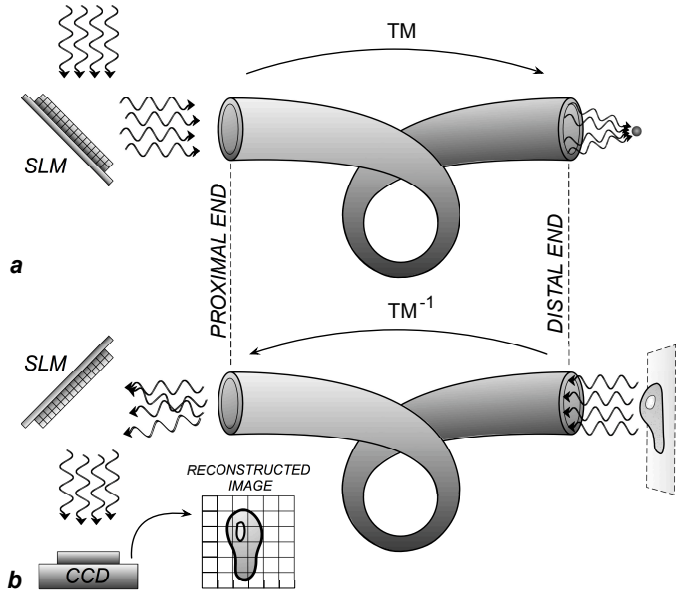


FIGURE 1.3: Multimode fibres as complex media. **a,** Focussing light through a multimode fibre (MMF). With the knowledge of the transmission matrix (TM) of the fibre, it is possible to spatially modulate the wavefront at the proximal end such that the optical field is tightly focussed at a certain working distance from the distal fibre facet, producing an aberration-free diffraction-limited spot. **b,** Wide-field imaging through an MMF. Once the TM of the MMF has been determined, the optical field at a given distance from the distal end of the fibre can be retrieved from the speckle pattern emerging at the proximal end.

microscopy based on multi-photon excitation. In the pulsed regime, both the material and modal dispersions broaden the pulse in the time domain. Nevertheless, purely spatial encoding can be used to optimise both the spatial and temporal domains simultaneously, allowing the delivery of sub-picosecond pulses through MMFs up to 30 cm in length. Two-photon absorption [32] and, later, two-photon microscopy [46], have been demonstrated using this strategy.

### 1.2.4 Optical trapping and manipulation

Optical tweezers, a tightly focused laser beam, allow for stable and contactless 3D confinement and manipulation of micro- and nano-objects [47–49]. Many exciting applications of this concept have been demonstrated across the domain of biophysics, particularly due to their ability to precisely exert and measure subpiconewton forces on single molecules or molecular assays [50]. So far, optical

tweezers have made many contributions to our understanding of molecular motors and the functionality of biological polymers driving the mechanics of cells [51–53]. Holographic optical tweezers (HOT) are currently the most advanced optical manipulation technique in which a multitude of trap sites can be simultaneously manoeuvred in all three dimensions through the use of wavefront shaping [54–56].

Due to the optically turbid nature of living matter, applications of optical tweezers are often limited to studies *in vitro*, with a few exceptions where investigations *in vivo* were bound to the superficial layers of tissues [57–59]. As before, the turbidity of tissues can be overcome by deploying optical fibres as minimally-invasive light guides to provide optical access at depth.

Fibre-based manipulation schemes date back to the early 1990s [60]. Static three-dimensional optical traps have been constructed using single-mode fibres in combination with elaborate terminations [61–63]. The first systems capable of one-dimensional manipulation were realised in counter-propagating dual-fibre schemes [64, 65] and, later by using few-mode fibres, enabled the controlled rotation of cells [66, 67].

Early studies of holographic light control through MMFs also brought the possibility of two-dimensional (lateral) confinement and manipulation [27, 35]. Due to the limited NA of commercially-available MMFs, however, the resulting foci could not provide full 3D confinement of micro-objects. Confined particles therefore had to be prevented from escaping the optical traps along the optical axis, which was achieved by trapping against a sample boundary (coverslip).

## 1.3 Aim

The aim of the present Thesis is to further develop the current state of the art in the topic of multimode fibre-based micro-endoscopy, by addressing some of its current challenges.

Specifically, the main objectives of this Thesis are:

- Development of experimental designs and methodologies of holographic light control capable of high-resolution focussing using novel types of very-high-NA multimode fibres;
- Demonstration of three-dimensional optical trapping and manipulation of dielectric micro-particles, employing the methods mentioned above, through minimally invasive endoscopic probes;

- Development of methodologies towards practical implementations in *in-vivo* biomedical settings, including generation and independent positioning of multiple optical tweezers.

Additional objectives relate to supporting the research activities lead by Sergey Turtaev. These are:

- Acceleration of the wavefront shaping optimisation procedures and raster-scanning fluorescence imaging via single-fibre endoscopes by exploiting digital micromirror devices as spatial light modulators;
- Design, development and demonstration of a minimally-invasive single-fibre endoscope for real-time deep-brain imaging in animal models *in vivo*.

## 1.4 Thesis outline

This Thesis consists of seven chapters, organised as follows:

Chapter 1 motivates the need for ever-smaller endoscopic probes and the potential of holographic micro-endoscopy exploiting multimode fibres in biophotonics settings. It also provides the reader with a general overview of the topics onto which the work presented in this Thesis builds upon. The general aim and specific objectives of the Thesis are summarised, and its structure presented.

Chapter 2 is devoted to the comparison of the currently most popular technologies for spatial modulation of light, liquid-crystal-based spatial light modulators (LC-SLMs) and digital micromirror devices (DMDs), in three typical scenarios: aberration correction in an optical system, focussing light transmitted across a highly-scattering medium, and generating diffraction-limited foci through a multimode fibre.

A new class of very-high-NA optical fibres is introduced in Chapter 3, as well as a design and methodologies for harnessing the full NA from such fibres and generate distal foci with unprecedented NA.

The ability to generate high-NA focussed outputs virtually free of optical aberrations is exploited in Chapter 4 for demonstrating holographic optical tweezers delivered by a lensless fibre, capable of three-dimensional trapping and manipulation of complex arrangements of dielectric micro-particles independently. The influence of bending of the fibre is also touched upon.

Chapter 5 addresses the characterisation of the fibre-based holographic optical tweezers. A methodology for particle tracking is presented which, based on

symmetry and principal component analysis of high-speed 2D video recordings, allows reconstructing the 3D trajectory of the Brownian motion of a trapped particle. This allowed estimating the strength of the optical tweezers, and studying their stiffness versus power characteristics. A methodology allowing the precise positioning of the optical tweezers at the nanometre-scale is also demonstrated. Lastly, the effect of temperature on the transmission matrix and its impact on defocus is briefly analysed.

In Chapter 6, deep-brain *in-vivo* fluorescence imaging is demonstrated using a minimally invasive micro-endoscopy system capable of real-time image acquisition and of resolving micrometre-sized neuronal structures.

Finally, Chapter 7 concludes the Thesis by summarising the results obtained and discussing their potential impact to the state of the art, as well as presenting a personal vision on the future developments in the field of holographic micro-endoscopy.

# Chapter 2

# Liquid-crystal and MEMS based spatial light modulation

Digital micromirror devices (DMDs) based on micro-electro-mechanical systems (MEMS) technology have recently emerged as practical alternatives to the well-established nematic liquid-crystal based spatial light modulators (LC-SLMs) for applications in photonics, primarily due to their modulation rates which can be orders of magnitude higher. This, however, comes at the expense of limited modulation depth as well as diffraction efficiency.

In this chapter, the beam-shaping fidelity of both technologies for spatial light modulation is compared in three distinct scenarios commonly encountered in the discipline of complex photonics: aberration correction of an optical system, focussing through a highly-scattering medium, and generating diffraction-limited foci across a multimode fibre.

The contributions from the author of this Thesis to the work presented in this chapter consisted of: (i) implementation of the holographic methods using the LC-SLM, (ii) measurements performed with LC-SLM based wavefront shaping, and (iii) contribution to the interpretation of the overall results.

The contents of this chapter comprise the following publication: S. Turtaev, **I. T. Leite**, K. J. Mitchell, M. J. Padgett, D. B. Phillips, and T. Čižmár, *Comparison of nematic liquid-crystal and DMD based spatial light modulation in complex photonics*, Optics Express 25(24), 29874–29884 (2017).

## 2.1 Need for speed

When considering imaging applications, and particularly those relying on raster-scanning focussed light behind a complex medium [23, 25, 35], the SLM

refresh rate becomes a critical attribute. Nematic liquid-crystal based SLMs (LC-SLMs) [68, 69] have been employed in numerous pioneering experiments involving these imaging modalities but, with refresh rates limited to 10–200 Hz, acquisition of a single frame containing a few kilopixels of data typically takes several minutes [35]. Even in case of the faster LC-SLMs alternative based on ferroelectric liquid crystals, which at the cost of a binary modulation depth have increased switching rates up to the kHz level [70], the still relatively low frame rates represent a severe obstacle for the majority of potential practical imaging applications. The combination of LC-SLMs with a faster beam-steering technology has been demonstrated to accelerate acquisition rates by over two orders of magnitude, but significantly compromises the maximum achievable pixel resolution [23].

Digital micromirror devices (DMDs) [71], which are based on micro-electro-mechanical systems (MEMS) technology, have emerged as a powerful solution to this problem, offering the fastest modulation rates (up to tens of kHz) among all solutions presently available in the market. Unlike LC-SLMs, which are typically capable of phase modulation with a depth of 8–12 bits, DMDs operate as purely binary amplitude modulators, posing a limit to the precision and efficiency with which each spatial degree of freedom can be controlled [72, 73]. Nevertheless, it has been shown that, by employing a DMD in the off-axis regime [41, 74], it is possible to perform beam shaping through both diffusive media [75] and multimode fibres [24, 76] at very high speeds.

## 2.2 Methods

The aim of these experiments was to investigate the comparative performance of a LC-SLM and a DMD as diffractive elements in typical scenarios of the ballistic, highly-scattering, and intermediate regimes, corresponding to aberration correction of an optical system, focussing through a ground-glass diffuser, and focussing through a multimode fibre. As such, the design of the experiments allowed interchanging the two SLMs, in order to maintain the same experimental conditions, as well as identical parameters in the holographic methods used. The performance of both modulators was assessed from recorded images of the generated foci, by using a figure-of-merit appropriate for each case.

The speed of the wavefront shaping optimisation methods was limited by the refresh rate of the modulator in case of the LC-SLM (Meadowlark HSPDM512,

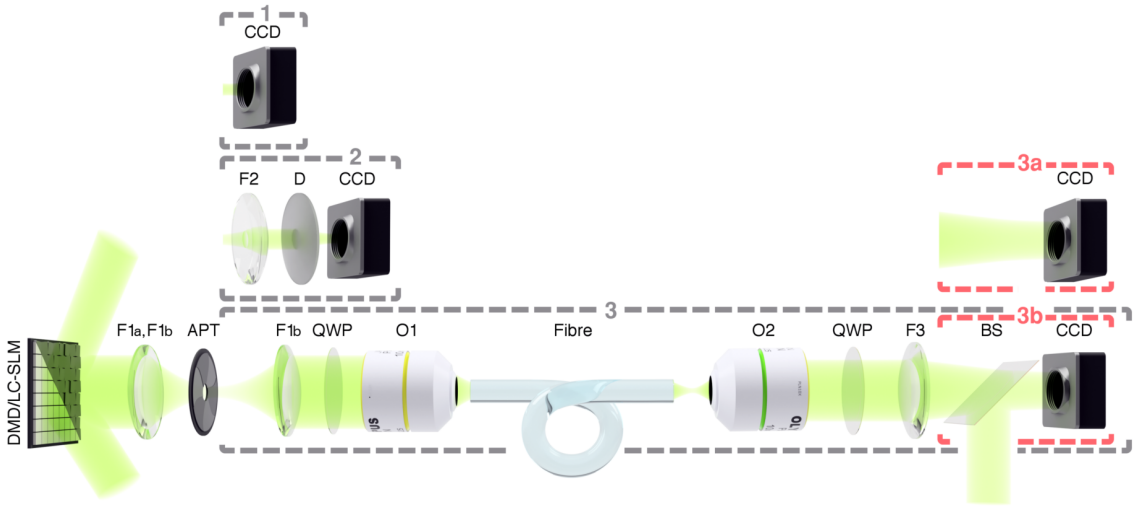


FIGURE 2.1: Modular experimental setup for comparison of LC-SLM and DMD based spatial modulation of light in the ballistic, highly-scattering, and intermediate regimes. **1,** Wavefront correction in the ballistic regime. **2,** Focussing in the highly-scattering regime. **3,** Focussing through a multimode fibre with internal (a) and external (b) phase reference.

512 × 512 resolution), and by the 400 Hz acquisition rate of the CCD camera (Basler piA640-210gm) when using the DMD (ViALUX V7001, 1024 × 768 resolution) which could operate at ≈23 kHz.

## 2.3 Experimental setup

The experimental setup was designed in a modular fashion, as illustrated in Fig. 2.1. The SLM (DMD or LC-SLM) was illuminated by a highly coherent, linearly-polarised laser beam at the 532 nm wavelength (CrystaLaser CL532-075-S). The SLM was employed in the off-axis regime, whereby a high-frequency spatial modulation was applied to the SLM and the resulting first diffraction order was isolated by an aperture APT at the Fourier plane of lens F1a or F1b. In all experiments, the active region of both the DMD and LC-SLM was limited to 512 × 512 individual elements.

For the study in the ballistic regime (configuration 1 in Fig. 2.1), the CCD camera was placed at the focal plane of lens F1a (500 mm focal length). In this case, the aperture APT used to isolate the first diffraction order was placed as close as possible to the CCD detector.

In configuration 2, used for studying the focussing performance in the highly-scattering regime, a collimating lens F2 (25 mm focal length) formed a demagnifying telescope, together with lens F1a, to reduce the beam diameter on the surface of ground glass diffuser D (placed in a plane conjugate to the SLM), in order to increase the power reaching the CCD.

For the study of focussing performance through a multimode fibre, the SLM was imaged onto the back-aperture of microscope objective O1 (Olympus Plan N, 10×, 0.25 NA) via the $4f$ system composed by the pair of identical lenses F1b (200 mm focal length), whereas the input fibre facet was placed in the focal plane of O1. Microscope objective O2 (Olympus Plan N, 20×, 0.4 NA) together with tube lens F3 (200 mm focal length) imaged the distal fibre endface onto the CCD. Quarter-wave plates QWP were employed to couple circularly-polarised light into the multimode fibre, since such modes have been shown to be better preserved upon propagation owing to the cylindrical symmetry of the waveguide [38]. For the measurement of the transmission matrix of the system, configuration 3a made use of an internal phase reference, which is transmitted through the fibre. In configuration 3b, an external phase reference was provided directly from the laser source via beamsplitter cube BS. The optical fibre used was a 300 mm-long step-index multimode fibre with 0.22 NA and 50 µm-diameter core (Thorlabs FG050UGA). At the 532 nm wavelength, the fibre sustains approximatly 2100 modes, i.e. ≈1050 per orthogonal polarisation state.

## 2.4 Holographic methods

### 2.4.1 Interferometric measurement of the transmission matrix

The optimisation method used is equivalent to measuring part (or the whole) transmission matrix (TM) of the complex medium, depending on the number of independent modes in the medium, as well as the dimension of the basis of input modes (i.e. the number of spatial degrees of freedom controlled). The TM is measured interferometrically, i.e. by superimposing the output optical fields with a coherent phase reference in order to assess both their amplitude and phase information. This procedure does not depend on the particular orthogonal basis of input modes chosen, provided each input mode can be generated in sequence. With the basis of output modes conveniently chosen as a square grid of diffraction-limited foci conjugate to individual pixels of a CCD camera, the interferometric response can be recorded for all output modes simultaneously.

The input and output modes, $\Psi^{\text{in}}_{k,l}$ and $\Psi^{\text{out}}_{u,v}$, are connected via a matrix of complex coefficients:

$$\Psi^{\text{out}}_{u,v} = \sum_{k,l} t^{k,l}_{u,v} \Psi^{\text{in}}_{k,l}, \tag{2.1}$$

where $(k,l)$ and $(u,v)$ label the input and output modes, respectively. Each element $t^{k,l}_{u,v}$ of the transmission matrix can be represented in the polar form as:

$$t^{k,l}_{u,v} = |t^{k,l}_{u,v}| e^{i\phi^{k,l}_{u,v}}, \tag{2.2}$$

where $i = \sqrt{-1}$ is the imaginary unit, the amplitude $|t^{u,v}_{k,l}|$ is a positive number and the phase $\phi^{u,v}_{k,l}$ has real values in the interval $[-\pi, \pi]$.

In the off-axis regime, where a high-frequency grating gives rise to distinct orders of diffraction, the phase of the first diffraction order can be conveniently changed by a lateral translation of the grating. Using the SLM to change the phase difference $\Delta\phi$ between a given input mode $(k',l')$ and the reference field $\Psi^{\text{ref}}$ leads to a harmonic signal of the intensity $I^{k',l'}_{u,v}$ in each position of the grid of output modes:

$$I^{k',l'}_{u,v} = |t^{k',l'}_{u,v} \Psi^{\text{in}}_{k',l'} \cdot e^{i\Delta\phi} + \Psi^{\text{ref}}|^2. \tag{2.3}$$

Since the TM is measured in the basis of input modes $\Psi^{\text{in}}_{k,l}$, then in this representation one has $|\Psi^{\text{in}}_{k',l'}| = 1$ and $\phi^{\text{in}}_{k',l'} = 0$ for the amplitude and phase of the probed input mode. Expanding the previous equation leads to:

$$I^{k',l'}_{u,v} = |t^{k',l'}_{u,v}|^2 + |\Psi^{\text{ref}}|^2 + 2|t^{k',l'}_{u,v}||\Psi^{\text{ref}}| \cos(\phi^{k',l'}_{u,v} - \phi^{\text{ref}} + \Delta\phi), \tag{2.4}$$

where $\phi^{\text{ref}}$ is the phase of the reference signal. Thus, the complex field (i.e. both amplitude and phase) at each position $(u,v)$ of the calibration plane can be retrieved by changing the phase difference $\Delta\phi$ in $n$ steps $\delta\phi$ (i.e. $\Delta\phi = q\delta\phi$, with $q = 1, \ldots, n$) using the recorded intensity $(I^{k',l'}_{u,v})_q$ for each step:

$$\sum_{q=1}^{n} (I^{k',l'}_{u,v})_q e^{iq\delta\phi} = 2|t^{k',l'}_{u,v}||\Psi^{\text{ref}}| e^{i(\phi^{k',l'}_{u,v} - \phi^{\text{ref}})}. \tag{2.5}$$

This is equivalent to measuring the row $(k',l')$ of the TM since the reference signal is assumed to have uniform amplitude $|\Psi^{\text{ref}}|$ across the grid $(u,v)$ of output modes.

For the experiments presented in this chatper, $\delta\phi = \pi/2$ and $n = 4$ or 8, corresponding to changing the phase in steps of $\pi/2$ over one or two phase periods.

### 2.4.2 Subdomain based optimisation

The wavefront correction technique used in the setup configurations 1, 2, and 3a was based on the decomposition of the initial laser field at the plane of the SLM into a series of orthogonal input modes, each corresponding to a different square region (subdomain) of the SLM chip [77]. The size of the subdomains was varied from $32 \times 32$ down to $4 \times 4$ pixels, yielding a number of controlled spatial modes ranging from 256 ($16 \times 16$ subdomains) up to 16384 ($128 \times 128$ subdomains). By modulating a particular subdomain with a linear grating, part of the reflected power is transferred from the zeroth diffraction order into the first diffraction order. In case of the LC-SLM, this was achieved using a diagonal blazed grating with a spatial period of 4 pixels (both horizontally and vertically) – the maximum permitted by the smallest ($4 \times 4$) subdomains used – which allowed 42% of the optical power to be redirected into the first diffraction order. Due to the discretisation of the blazed grating, larger spatial periods (and, accordingly, larger subdomains) can increase the diffraction efficiency of the LC-SLM, but come at the expense of a smaller number of spatial degrees of freedom controlled for a given resolution of the SLM. A binary amplitude grating [78] with the same periodicity of 4 pixels was applied to the DMD, resulting in a diffraction efficiency of only 8% under the same conditions.

When using an internal phase reference, a particular input mode (subdomain) is selected as a reference, and all remaining input modes are examined one by one as follows. Both the reference mode and a mode under "test" propagate through the optical system and interfere at the calibration plane (either a plane conjugate to the CCD, or the CCD itself). The phase of the "tested" mode can be modified by translating laterally the grating applied to the corresponding SLM subdomain, resulting in change of the recorded intensity by the CCD, which has a sinusoidal dependence on the phase difference between the two modes. The phase of this sinusoidal curve reveals the optimal phase at which the mode under test interferes constructively with the reference. Repeating this procedure for all input modes and subsequently switching them all "on" with the optimal phase applied, results in optimum focussing, as all modes interfere constructively in simultaneous.

The interferometric measurements for each subdomain were performed with phase-steps of $\pi/2$. To assess the influence of temporal fluctuations in the efficiency of the SLM during the optimisation procedure, the interferometric measurements were obtained both for a phase sweep of one and two full cycles (i.e. $2\pi$ and $4\pi$). Well-known sources of such fluctuations in LC-SLMs include transfer delay time, response time and flicker [79], which affect the accuracy of the interferometric measurements and, in consequence, the quality of the resulting wavefront correction. To mitigate the influence of transfer delay and response time, a waiting time of 25 ms was implemented between uploading the phase hologram on the LC-SLM and image acquisition by the CCD camera. Additionally, the particular model used is known to exhibit low, although still apparent, phase flicker.

Having measured the transmission matrix $t^{k,l}_{u,v}$ of the complex medium, a given output mode $(u', v')$ is generated by applying the complex modulation encoded in its corresponding column $t^{k,l}_{u',v'}$. In case of phase-only modulation, however, only its phase information is used:

$$\phi_{u',v'}(k,l) = \arg\left(t^{k,l}_{u',v'}\right), \tag{2.6}$$

where $\arg()$ denotes the argument, or phase, of a complex number.

The binary amplitude hologram encoding the target phase (2.6) applied to the DMD is given as:

$$H(x,y) = \frac{1}{2} + \frac{1}{2}\mathrm{sgn}\left(\cos\left[\phi(x,y) + \phi_{\mathrm{tilt}}(x,y)\right]\right), \tag{2.7}$$

where $x$ and $y$ represent the positions (in pixel units) of each individual element of the SLM, $\mathrm{sgn}()$ denotes the sign function, $\phi(x,y)$ is the target phase $\phi(k,l)$ expressed in pixel units, and $\phi_{\mathrm{tilt}}(x,y)$ the phase tilt, given by:

$$\phi_{\mathrm{tilt}}(x,y) = 2\pi\left(f_x x + f_y y\right), \tag{2.8}$$

where $f_{x,y} = 1/\Lambda_{x,y}$ are the spatial frequencies and $\Lambda_{x,y}$ the periods (in pixel units) along the $x$ and $y$ directions of the underlying linear grating applied (in this case, $\Lambda_x = \Lambda_y = 4$).

The phase hologram applied to the LC-SLM is given by:

$$H(x,y) = \pi\,\mathrm{sawtooth}\left[\phi(x,y) + \phi_{\mathrm{tilt}}(x,y)\right], \tag{2.9}$$

with $\phi_{\text{tilt}}$ given by Eq. (2.8), and where sawtooth() is the "sawtooth" function with unit amplitude and period $2\pi$, defined as:

$$\text{sawtooth}\,(x) = -\frac{2}{\pi}\tan^{-1}\left[\cot\left(\frac{x}{2}\right)\right], \tag{2.10}$$

which is used to wrap the phase to values in the interval $]-\pi, \pi]$ with a blazed grating.

### 2.4.3 Fourier-domain based optimisation

The comparative performance of the modulators was also investigated under an alternative optimisation approach using a different basis of input modes. This was realised exclusively for the last case-study – generating diffraction-limited foci across a multimode fibre – making use of an external phase reference (configuration 3b of the experimental setup shown in Fig. 2.1).

Here, the input modes are formed by quasi-plane waves truncated by the SLM chip, each being transmitted at a different angle corresponding to a specific wavevector. Each such truncated plane wave forms a focussed spot at a different location of the input facet of the MMF. This square grid of foci thus forms a new orthogonal basis of input modes. As in the subdomain based optimisation, the optimal phase to be applied to each input mode is found by analysing the interference with the external reference at the CCD plane. This technique is slightly more demanding in the post-processing stage than the subdomain method, since the reconstruction of the desired wavefront is made in the Fourier domain [38, 80]. However, it brings the advantage of making a more efficient use of the optical signal during the TM measurement. Firstly, each tested mode makes use of light reflected by the entire SLM chip, rather than from an individual subdomain, thus improving the signal-to-noise ratio of the interferometric measurements. Secondly, the basis of input modes can be reduced to only the truncated plane waves which result in focussed spots incident onto (and therefore coupled into) the fibre core. Neglecting all remaining input modes minimises the number of measurements required, thus decreasing significantly the optimisation time. Finally, the employment of a uniformly distributed external reference signal eliminates the effect of "blind" spots resulting from the speckled nature of internal references [27].

In this case, the complex modulation generating a given output mode $(u', v')$ is reconstructed in the Fourier domain by reshaping its corresponding column

$t^{k,l}_{u',v'}$ and shifting it to the location of the first diffraction order. In order words, we build an $M \times M$ matrix of complex elements, $h_{u',v'}(x,y)$, which is zero everywhere with the exception of the elements:

$$h_{u',v'}\left(\frac{M}{2}+Mf_x+k,\frac{M}{2}+Mf_y+l\right)=t^{k,l}_{u',v'} \tag{2.11}$$

for $k,l=-\sqrt{N}/2,\ldots,\sqrt{N}/2-1$, where $N$ is the number of input modes used, and $M^2$ is the number of individual elements in the active area of the SLM (in these experiments, $M=512$ for both types of modulators).

The phase hologram applied to the LC-SLM is then obtained as:

$$H_{u',v'}(x,y)=\arg\left(\mathcal{F}^{-1}\left[h_{u',v'}(x,y)\right]\right), \tag{2.12}$$

where $\mathcal{F}^{-1}$ denotes the inverse Fourier transform, implemented using a fast Fourier transform (FFT) algorithm. The binary amplitude hologram to be applied to the DMD is obtained by binarising the previous phase modulation, i.e.:

$$H_{u',v'}(x,y)=\frac{1}{2}+\frac{1}{2}\mathrm{sgn}\left(\cos\left[\arg\left(\mathcal{F}^{-1}\left[h_{u',v'}(x,y)\right]\right)\right]\right). \tag{2.13}$$

**Tracking the phase drift**

Acquiring the TM corresponds to repeating the procedure detailed in Subsection 2.4.1 for all input modes, i.e. all combinations of $(k,l)$. This procedure can take from just 2.5 s – for 256 input modes, 4 measurements per mode (one phase period) using the DMD at a modulation rate of 400 Hz – up to 55 min – in case of 16384 input modes, 8 measurements per mode (two phase periods) using the LC-SLM at a modulation rate of 40 Hz. During this period, an external phase reference usually experiences variations due to an unavoidable degree of instability in the system, which translates into an error in the measurement of $\phi^{k,l}_{u,v}$ [Eq. (2.5)]. Such instabilities do not affect the TM measurements using an internal phase reference, which benefit from the robustness of common-path interferometry. It is therefore critically important to measure and correct for the phase drift between the reference and input modes during TM acquisition when making use of an external phase reference [27].

### 2.4.4 Alignment of the fibre endfaces

In order to identify the location of the input fibre core, the fibre facet was raster-scanned with focal points, corresponding to truncated plane-waves at the SLM, while measuring the output power leaving the distal facet by integrating the intensity reaching the CCD. This enabled identifying which input spatial modes were efficiently coupled into the fibre and, in the case of the Fourier-domain based optimisation, also defining the size of the basis of input modes used in the TM acquisition. The axial alignment was adjusted by maximising the contrast in coupling efficiency between the input modes which were coupled into the fibre core and those which were incident onto the cladding. The alignment of the distal fibre facet was straightforward, since it was imaged directly onto the CCD. The fibre extremities were held by $x, y$-micropositioners, allowing the precise alignment in the transverse directions, whereas the axial alignment was adjusted by $z$-micropositioners holding each microscope objective.

## 2.5 Results

### 2.5.1 Wavefront correction in the ballistic regime

Aberrations in optical systems corrupt a propagating wavefront and thus, in the focal plane, smear out the focus, decreasing its peak intensity. To evaluate the performance of wavefront correction implemented with both types of SLMs, the metric quantifying the quality of the focus produced was the improvement in peak intensity, i.e. the ratio between the maximum intensities after and before applying the wavefront correction. This was calculated at the particular CCD pixel for which the correction was performed.

Figure 2.2 shows that, for both modulators, increasing the number of spatial modes in the wavefront correction algorithm results, in general, in an enhanced peak intensity. For both types of SLMs, the main cause of aberrations in the system was the surface curvature of the modulators themselves. The phase maps in the insets of Figs. 2.2a,b, measured for 1024 modes, show that the surface of the DMD chip is considerably more curved than that of the LC-SLM. This can also be seen directly from the images of the uncorrected focus (leftmost insets) which noticeably suffers from stronger aberrations in the case of the DMD. Nevertheless, the wavefront shaping technique corrects for these, as well as any other, sources of aberrations present in the optical system.

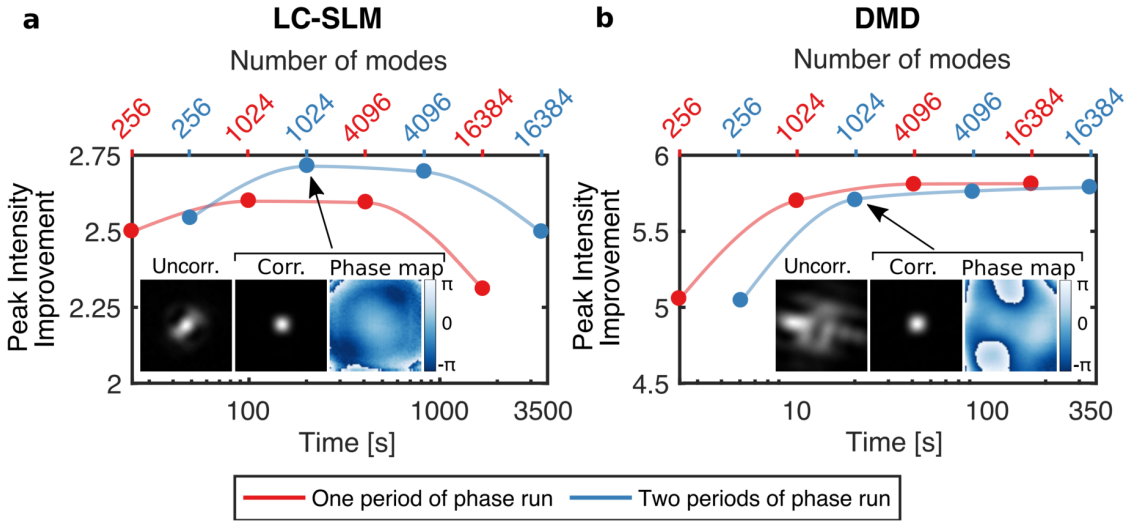


FIGURE 2.2: Wavefront correction in the ballistic regime: aberration correction of an optical system. Peak intensity improvement as a function of optimisation time and number of spatial modes controlled, measured for a LC-SLM (**a**) and a DMD (**b**). The insets show the uncorrected and corrected foci, as well as the map of measured phase aberrations in each case. The standard deviations are smaller than the size of the symbols.

In the case of the LC-SLM, the peak intensity reached its maximum value when using a correction based upon the measurement of 1024 spatial modes (i.e. corresponding to a grid of $32 \times 32$ subdomains). However, when the number of spatial modes was increased to 16384 (i.e. a $128 \times 128$ grid of subdomains, each consisting of $4 \times 4$ individual pixels), the peak intensity of the focus fell considerably below the maximum value. This can be understood by considering the scattering in liquid-crystals: the portion of light diffracted from such small subdomains is comparable in power to the amount of light which is scattered from the rest of the LC-SLM chip. This relatively strong background signal, compared to the small portion of light from a single subdomain, reduces the accuracy of the measurements. In the most critical case, this signal interferes destructively with the reference, leading to the failure of the method in that particular point, thus corrupting the wavefront correction calculated.

In the case of the DMD, the peak intensity of the focus also reached a value close to its maximum for a correction using 1024 modes, from which point it remained nearly constant for higher number of spatial modes. Since there is less randomly scattered light from the DMD in comparison to the LC-SLM, further

increasing the number of spatial modes does not increase or decrease the quality of the optimisation procedure.

Another aspect addressed was the effect of increasing the number of phase sweeps in the interferometric measurement of the TM. In Fig. 2.2, the measurements shown in red correspond to optimisations using one phase cycle, whereas those shown in blue correspond to wavefront correction using two phase cycles. In case of the LC-SLM, increasing the number of phase sweep cycles lead to a significant improvement in peak intensity and, of course, doubled the optimisation time since the number of measurements was increased two-fold. The improvement in peak intensity is more pronounced for larger number of input modes. This implies that there is a random error in the measurements which becomes more significant for smaller subdomains, but which is reduced by averaging over a larger number of measurements. This random error may originate in the "flicker" associated with LC-SLMs: these devices typically operate by switching the polarity of the electric field across the liquid-crystal layer; therefore, even when a displayed pattern is not changed, flicker can occur due to this continuous switching, which periodically alters the phase of each pixel by a small amount. As expected, the absence of flicker in the DMD modulator results in no difference in performance for optimisation procedures using one or two phase sweep cycles.

### 2.5.2 Focussing through a ground-glass diffuser

In the highly-scattering regime, where the medium transforms a coherent beam into a speckle pattern, the wavefront correction technique allows redistributing light towards a chosen target point behind the diffuser. In such complex scattering media, the number of channels (i.e. the number of distinct possible routes of light propagation) by far exceeds the number of input spatial modes (e.g. subdomains) that is possible to control using an SLM. Therefore, in addition to the target focal spot, this leads unavoidably to the formation of a diffuse speckled background arising from the uncontrolled light. The ratio between the peak intensity at the target spot and the average background level, known as *enhancement*, is the metric most frequently used to assess the quality of an optimisation procedure in this context [13, 40]. In this regime, the maximum attainable enhancement grows linearly with the number of spatial modes controlled [13]. For instance, a focus with enhancement of 54 was obtained in the first demonstration of light control using the optical transmission matrix framework, using a total of

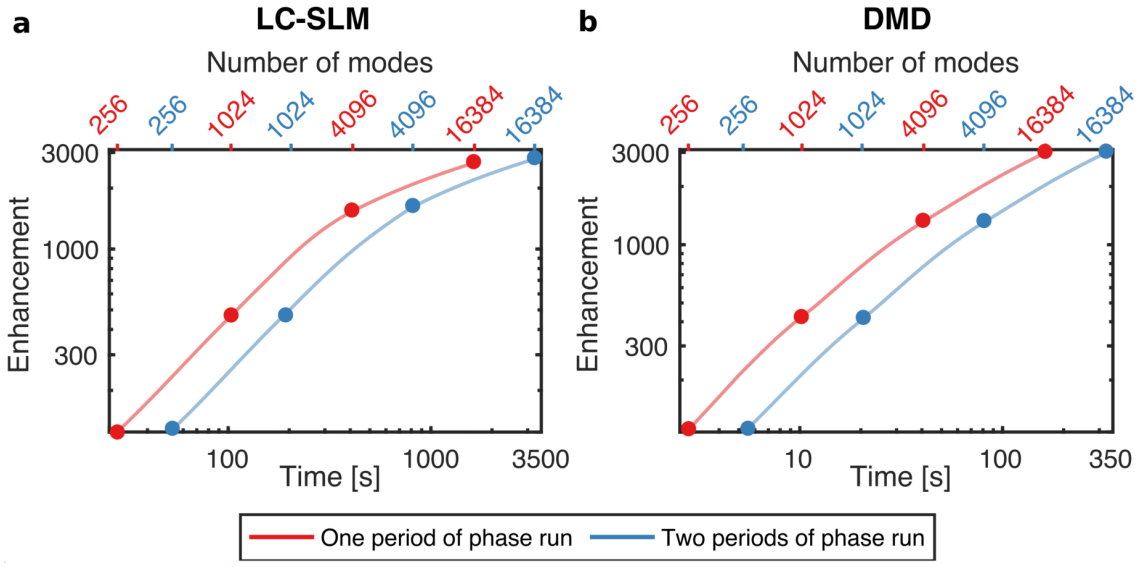


FIGURE 2.3: Holographic beam-shaping in the highly-scattering regime: focussing through a ground-glass diffuser. Enhancement as a function of optimisation time and number of spatial modes controlled, measured for a LC-SLM (**a**) and a DMD (**b**). The standard deviations are smaller than the size of the symbols.

256 controlled channels (corresponding to a TM with size $16 \times 16$) [43]. More recently, enhancements exceeding $10^5$ have been shown employing a 1 megapixel DMD [81].

Figure 2.3 shows the enhancement measured as a function of the number of spatial modes controlled, for both the LC-SLM and DMD. The relative standard deviations of the measurements have not exceeded 2%. The values and trends are very similar for both types of modulators. As in the previous case, the interferometric measurements using two phase cycles does not improve the quality of the wavefront shaping procedure for the DMD, but brings a slight improvement for the LC-SLM as it suppresses the adverse effect of phase flicker.

### 2.5.3 Focussing through a multimode fibre

Focussing through a multimode fibre can be regarded as an intermediate regime between the ballistic and highly-scattering (including diffusive) regimes, since it can be seen as a turbid medium with number of channels (number of waveguide modes) comparable to the number of degrees of freedom controllable by an SLM. Another particular aspect of MMFs is their ability to deliver almost all the coupled light to the distal facet, in contrast to other turbid media. For this reason,

the metric assessing the performance of the wavefront shaping procedure used in this case was the ratio between the power in the focal spot compared to the total output power leaving the distal fibre facet. Using this *power ratio* (PR) allows estimating the proportions of light contributing to a signal and to background noise in a particular application.

The performance of both types of modulators was compared using two implementations of the wavefront shaping procedure, which differed on the choice of spatial input modes (subdomains or truncated plane waves) and usage of an internal or external phase reference. In both cases, the results shown were obtained from three consecutive runs of the optimisation procedure (TM measurements) and $7 \times 7$ diffraction-limited foci generated sequentially across a square grid at the distal fibre facet.

**Subdomain based optimisation** Figure 2.4a shows the power ratio as a function of number of sampled modes resulting from the same subdomain based wavefront optimisation method used in the previous two subsections. For both types of SLM, the PR seems to start reaching saturation at around 4000 spatial modes. Noticeably however, the PR is $\approx$10–15% higher for the DMD-based measurements compared to those obtained with the LC-SLM, as well as shows much smaller dispersion around the average values. As in the previously studied regimes, this is likely a consequence of the detrimental effects of scattering from the liquid crystals in the LC-SLM, which are not present in the DMD. In each measurement of the PR, when applying a spatially pre-shaped wavefront, the portion of uncontrolled light within the acceptance angle of the fibre propagates to the distal facet, giving rise to an uncontrollable background. It was not possible to directly observe this effect in the previous two experiments, dealing with the ballistic and highly-scattering regimes: in first case a normalised quality metric was used and, therefore, the measurements obtained using the LC-SLM and DMD cannot be compared in absolute values; in the latter, only a very small amount of uncontrolled light reflected off the SLM reached the CCD detector.

**Fourier-domain based optimisation** The performance of the Fourier-domain based wavefront optimisation method for both modulators is shown in Fig. 2.4b. In both cases, the PR reaches a plateau at $\approx$1000 modes, from which point it increases very slowly with the number of spatial modes controlled. This coincides with the number of guided modes sustained by this multimode fibre per polarisation state – note that only one polarisation state was controlled in this experiment.

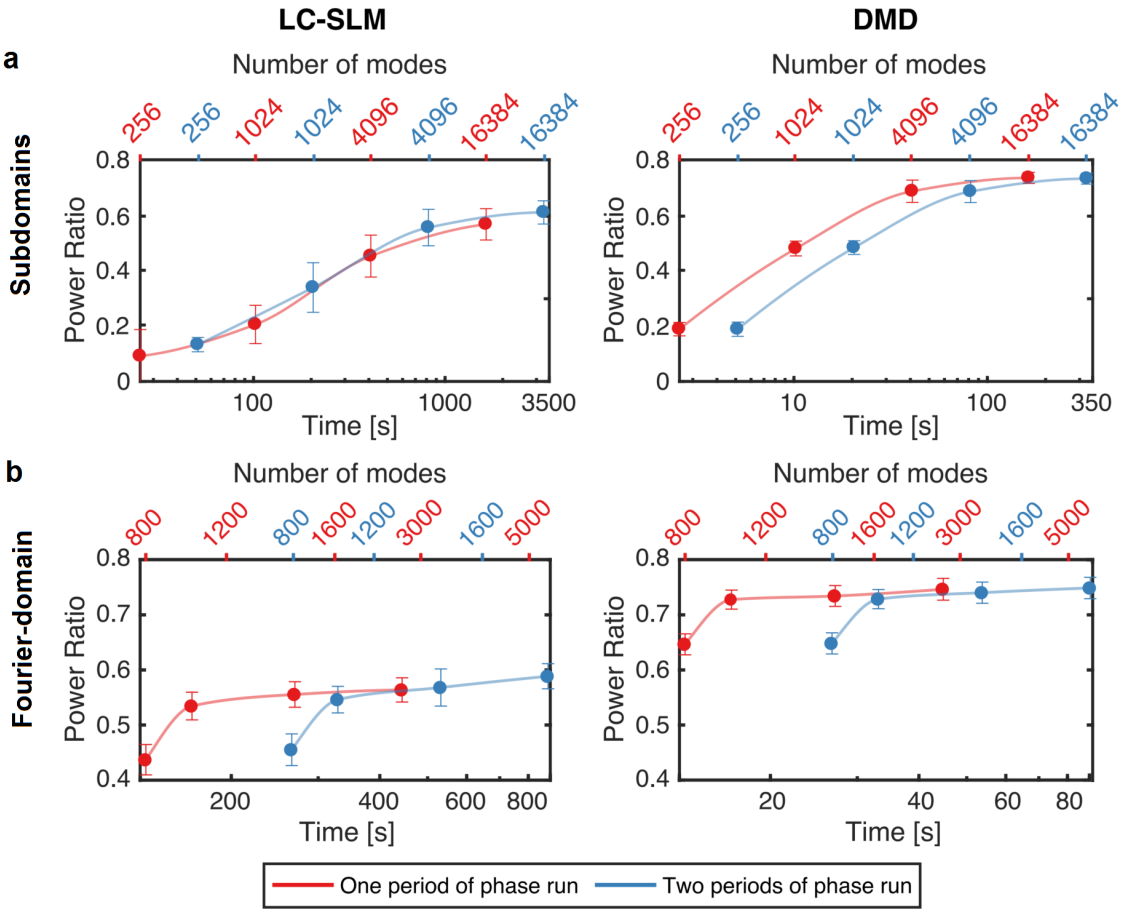


FIGURE 2.4: Holographic beam-shaping in the intermediate regime: focussing through a multimode fibre. Power ratio as a function of optimisation time and number of spatial modes controlled for both subdomain (**a**) and Fourier-domain (**b**) based approaches, for a LC-SLM and a DMD.

Noticeably, this plateau in the PR was reached within approximately one tenth of the optimisation time required by the subdomain based optimisation procedure. Moreover, such improvement in optimisation time did not compromise the quality of the foci produced, as the maximum PR values measured were equivalent with either basis of input spatial modes. As previously seen with the subdomain based optimisation, also in the Fourier-domain based optimisation the DMD generated foci at the distal end of the MMF had PR up to 15% higher than those produced using the LC-SLM. This is because, despite the higher signal-to-noise ratio during the optimisation procedure, the LC-SLM still suffers from significant uncontrolled scattering collected by the MMF which reduces the PR level.

As before, increasing the number of phase sweeps in the interferometric measurement of the TM significantly improves the quality of the wavefront shaping procedure in case of the LC-SLM, especially before the PR reaches saturation, whereas no differences are observed in case of the DMD.

## 2.6 Discussion

While LC-SLMs have been the standard choice in wavefront-shaping applications for over a decade, and are still the most frequently used modulators in applications of complex photonics, alternative MEMS-based DMDs have started to increase in popularity in the last few years. DMDs are usually chosen because of their faster modulation rates, at the cost of modulation depth and overall diffraction efficiency.

This study showed that in the off-axis regime, despite the limited depth of modulation, DMDs may outperform LC-SLMs not only in modulation rate but, importantly, also in beam-shaping fidelity. One reason for their superior beam-shaping performance is that DMDs do not suffer from the scattering affecting LC-SLMs, which corrupts the optimisation procedures and contributes to uncontrollable background signals. This is particularly crucial when focussing light through MMFs, where the LC-SLM based system could achieve a power ratio of 60% at the target focal point, whereas the DMD based system operating in an identical regime reached a power ratio of 75%. In potential applications of this technology to imaging, this translates to a direct improvement in image contrast.

Another inherent drawback of LC-SLMs is phase flicker, which decreases the precision of the phase measurements during the optimisation procedure. Although this effect can be averaged out by increasing sampling for each input mode, this results in longer optimisation durations. Additionally, other possible sources of quality loss, such as cross-talk between pixels, can be expected when using LC-SLMs [82].

This study also showed that, when characterising a multimode fibre, using the Fourier-domain based optimisation procedure in place of the subdomain-based approach can decrease the optimisation time by one order of magnitude.

Due to their minimal modulation depth, DMDs offer reduced diffraction efficiencies when compared to LC-SLMs. This translates into a smaller power efficiency in off-axis implementations. Indeed, only 8% of the total power was found in the first diffraction order when using the DMD, in contrast to 42% in the case

of the LC-SLM. In many applications this can be compensated by increasing the power of the laser source; however, there are cases where the photon budget cannot be compromised, and the advantages of DMDs would not trade-off well.

# Chapter 3

# High-resolution Focussing through a High-NA Multimode Fibre

The ability of imaging and focussing through a multimode fibre (MMF) is limited in resolution by its numerical aperture (NA), which sets the upper limit for the spatial frequencies which are allowed to propagate through. Rather than merely bringing an incremental improvement to the resolution of previously demonstrated techniques such as raster-scanning imaging, increasing the available NA has the potential to unlock a variety of other imaging modalities and biophotonics techniques, such as optical tweezers, delivered through single-fibre probes.

This chapter introduces a new class of all-solid, high-NA MMFs, and describes how they can be exploited for high-resolution focussing with unprecedented output NA. Such fibres are, however, significantly affected by mode-dependent loss (MDL) – i.e. difference in attenuation among the several waveguide modes – which reduces the NA of the foci generated. A method for measuring the mode-dependent transmission of the fibres is presented, as well as a strategy for redistributing the optical power in the proximal far-field in such way as to maximise the output NA at the distal fibre output.

The high-NA MMF introduced in this chapter was designed and manufactured by Xin Jiang and Philip St.J. Russell at the Max Planck Institute for the Science of Light (Erlangen, Germany).

The contributions from the author of this Thesis to the work presented in this chapter consisted of: (i) designing and building the experimental setup, (ii) implementation of the wavefront shaping algorithms, (iii) measurements of MDL and implementation of the MDL-compensation methodology, and (iv) analysis of the results.

The contents of this chapter form part of the following publication: **I. T. Leite**,

S. Turtaev, X. Jiang, M. Šiler, A. Cuschieri, P. St. J. Russell, and T. Čižmár, *Three-dimensional holographic optical manipulation through a high-numerical-aperture soft-glass multimode fibre*, Nature Photonics 12(1), 33–39 (2018).

## 3.1 All-solid high-NA optical fibre

The vast majority of commercially available optical fibres are based on well established designs and manufacturing technologies which have been developed mainly for applications in telecommunications. However, attributes such as low-cost and low-attenuation which are greatly appreciated for kilometre-scale networks are in general not beneficial for applications in micro-endoscopy – where the length scales involved are in the order of centimetres – as they are generally associated with unnecessarily large cladding dimensions and low NA. The NA of fibres available commercially is typically limited to 0.3 for core diameters below 200 µm. Silica-core polymer-cladding large-mode-area fibres with core diameters ranging from 200 µm up to 1500 µm are available with NAs as high as 0.5; in this case, however, the number of guided modes far exceeds the number of spatial modes controllable with the current technology for spatial light modulation.

The NA of standard MMFs can be enhanced by means of engineered terminations. One approach is to combine the fibres with micro-fabricated optical components, either mounted onto or directly fabricated at the fibre endface. Examples include multi-lens micro-objectives around 100 µm in size manufactured by two-photon direct laser writing [83], and 50 µm-sized parabolic reflectors produced by two-photon polymerisation, which increased the ouput NA of a fibre from 0.22 to approximately 0.93 [84]. The drawback of this approach is typically seen in the resulting extended footprint of the fibre probe compared to the field of view where the enhanced NA is obtainable. An alternative strategy consists in introducing a highly-turbid layer to the distal facet of the MMF [85, 86]. Multiple scattering events within the turbid medium facilitate the conversion of higher spatial frequencies into lower order modes which are able to propagate in the MMF, thus resulting in an enhancement of the effective output NA of the combined structure. In such approach however, the increased amount of output modes significantly outnumbers the input modes. This poses limits to the control of the output fields, resulting in strong random background signals which interfere with the foci.

Another possibility is, of course, to devise alternative fibre designs which can render high NAs. Air-clad fibres are a class of photonic-crystal fibres in which

air holes surround a central solid core which is suspended by small "bridges" or "webs" preventing the structure from collapsing. Owing to the high air-filling fraction, the effective index of the cladding material can be made close to 1 which, for a silica core (refractive index ≈1.45) should yield an NA of approximately 1 [87, 88]. In practice however, the NA of the fibre depends strongly on the width of the bridges; if they are comparable to, or greater than, the wavelength, light will be mostly confined to the silica bridges instead of the air holes, and the effective index of the cladding will be close to that of silica, thus resulting in a low NA. For instance, the fibres reported by Wadsworth *et al.* showed NAs in excess of 0.9 at the 1.5 µm wavelength, decreasing to 0.65 at 450 nm [87]. The bridges should be less than five times smaller than the wavelength in order to reach the highest possible NA values [88]. Such small bridge widths typically cause deficits in the mechanical stability of the fibre structure, especially when designed to work in the visible range [89]. Nevertheless, lensless focussing by means of wavefront shaping through air-clad fibres has been shown in the visible spectrum (at the 633 nm wavelength) with output NAs up to 0.61 [90]. Such fibres may however be inadequate for applications in biological scenarios because, in addition to their fragility, changes to light propagation induced by liquids entering the hollow fibre channels render such fibres unsuitable for use in aqueous environments.

Taking these trade-offs into account, the ideal candidate for *in-vivo* applications would be an all-solid, step-index MMF having a very high refractive index contrast between the core and cladding materials capable of yielding a very-high NA. The lowest refractive indices available in transparent materials are around 1.3 which, for a core of silica glass, yields a maximum NA of approximately 0.6 [87]. Non-silica based glasses, so-called "soft glasses", are characterised by lower melting and processing temperatures compared to silica and, importantly, a wider range of refractive indices is available in this category of glass materials [91, 92].

A step-index MMF from such compound "soft-glasses", capable of offering uniform high NA across the entire fibre core, was developed by collaborators at the Max Planck Institute for the Science of Light. Two lead-silicate glasses having remarkably different refractive indices comprise the core and cladding materials (respectively, dense flint Schott SF57 and very-light flint Schott LLF1). The NA of this fibre, estimated by Eq. (1.1) using the optical parameters of these glass materials [93], exceeds the value of 1 at wavelengths below 620 nm and 0.96 at 1064 nm, as shown in Fig. 3.1. The fibre features a core diameter of 20 µm and at 1064 nm supports ≈1600 guided modes.

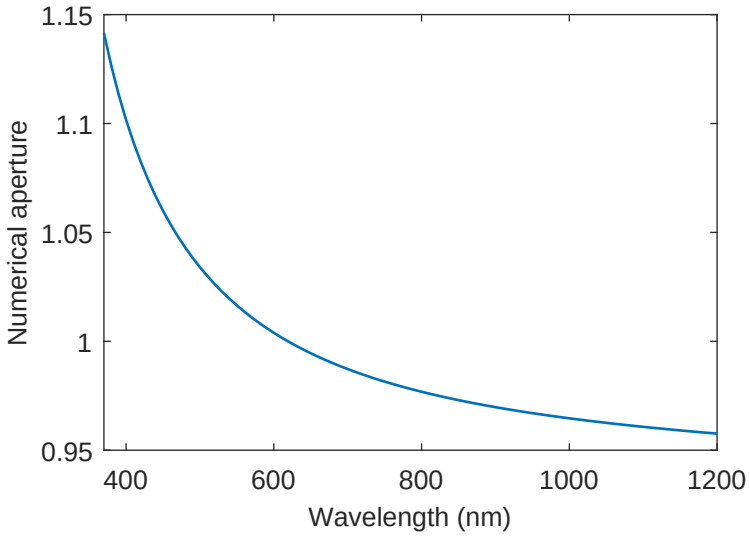


FIGURE 3.1: Estimated numerical aperture of the soft-glass fibre in the visible and near-infrared spectrum. The numerical aperture was calculated by Eq. (1.1) using the refractive indices of the glass materials (core: Schott SF57, cladding: Schott LLF1) obtained from [93].

### 3.1.1 Fibre manufacturing

#### Fibre drawing

The step-index lead-silicate fibre had core and cladding formed from Schott SF57 and LLF1 glass respectively, with refractive indices 1.8117 and 1.5346 at 1064 nm, resulting in an NA of 0.96 at this wavelength. The glass transformation temperatures ($T_g$, corresponding to a viscosity of $\approx 10^{12}$ Pa s) are 414 °C for SF57 and 431 °C for LLF1, and for successful fibre drawing it is crucial that the furnace temperature is chosen such that the viscosity of the "harder" cladding glass lies in the range $10^5$ Pa s to $10^6$ Pa s. The fibre preform was prepared by a multi-step rod-in-tube process, and the fibre was drawn at ≈725 °C, corresponding to the viscosity of $10^{5.7}$ Pa s for the LLF1 glass, and $10^{3.4}$ Pa s for the SF57 glass. The fibre drawing was carried out following the procedure developed for photonic crystal fibres [94, 95], including a custom-designed heating element to provide a highly uniform temperature distribution around the preform. During drawing, the end-face of the preform was connected to a vacuum pump so as to close the gaps between the rod and jacket tube. An outer UV-cured polymer coating increases the mechanical robustness of the fibre. Figure 3.2a shows a scanning electron micrograph (SEM) of the final fibre structure.

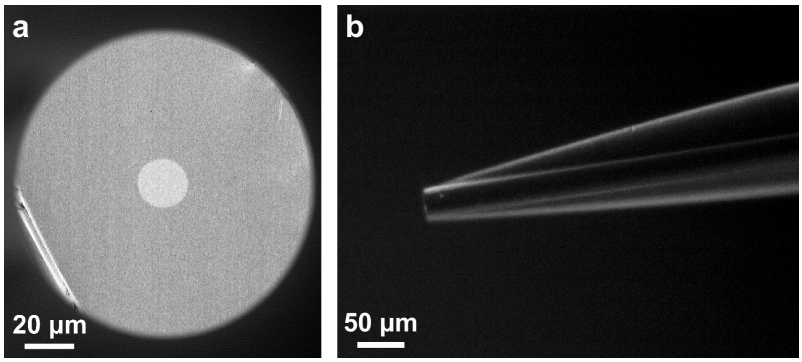


FIGURE 3.2: All-solid step-index multimode fibre based on compound "soft glasses". **a,** SEM image of the fibre endface. The diameters of the core and cladding are 20 µm and 125 µm, respectively. **b,** Micrograph of a post-processed fibre probe where the cladding thickness has been reduced to 35 µm (at the tip) by side-polishing.

**Post-processing of the fibre probes**

To reduce the lateral instrument footprint, the fibres were post-processed into a flat-cone termination, as shown in Fig. 3.2b, where the cladding thickness was reduced from 125 µm to 35 µm at the tip. The fibres were held by a fibre clamp (Thorlabs SM1F1-250) fixed onto a stepper motor allowing for rotation (≈5 rpm) around their axis. An xy-translation mount (Thorlabs CXY1) is used for the fine adjustment correcting for eccentricity in the rotation. A fibre polishing sheet (Thorlabs LF3D) has been cut into the circular shape with 4 cm-diameter and fixed onto a fast-rotating stage (≈500 rpm). The rotating polishing sheet was then brought into contact with the fibre under a grazing angle (≈5°) to polish out the cladding. A low-magnification microscope objective together with a tube lens and a CCD camera were used to monitor the fibre post-processing in real time.

## 3.2 Mode-dependent loss

Attenuation, or transmission loss, in an optical fibre is caused primarily by both scattering and material absorption, and can in most cases by accounted for by an imaginary component in the (now, complex) propagation constants $\tilde{\beta}_{lm} = \beta_{lm} + i\alpha_{lm}$, with $\alpha_{lm}$ designated as the attenuation coefficient. Here, the mode indices $l, m$ are included because, in general, not all waveguide modes in an MMF experience the same degree of attenuation, an effect known as mode-dependent loss (MDL) [88, 96]. On the one hand, higher-order modes travel effectively

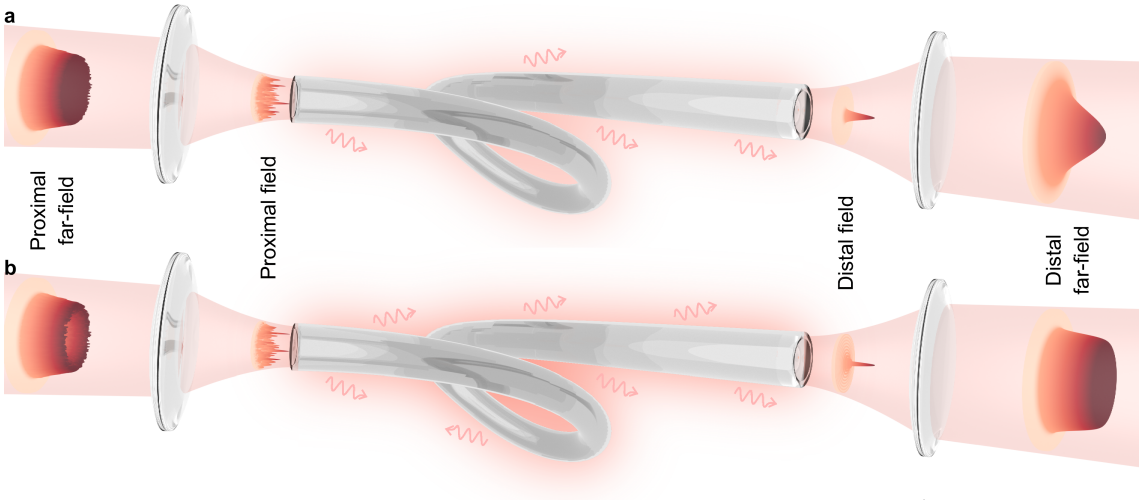


FIGURE 3.3: Mode-dependent loss in multimode fibres. **a,** The presence of mode-dependent loss (MDL) in multimode fibres (MMFs) preferentially attenuates the higher-order waveguide modes, which carry the higher transverse spatial frequencies. **b,** The MDL can be pre-compensated in the proximal far-field so as to equalize the power spectrum in the distal far-field.

longer in the fibre, and are therefore subjected to higher material absorption. On the other hand, inhomogeneities or impurities in the core or cladding acting as scattering centres can interact differently with distinct mode distributions and also give rise to loss.

In highly multimode fibres, the waveguide modes can be grouped into families having similar propagation constants, *mode groups*, that do not exchange power among each other. Even in deformed fibres, intermodal coupling occurs predominantly within each mode group, not between mode groups, which preserves the identity of each mode group during propagation. In step-index MMFs, each mode group occupies a different annular zone in the proximal far-field and, due to the propagation invariance and absence of coupling, it will also be found at the same annular zone at the distal far-field after leaving the fibre. Due to MDL, those mode groups with smaller propagation constants (thus, carrying the higher transverse spatial frequencies) experience higher loss. The resulting non-uniformity in the distal far-field thus impairs the full exploitation of the available NA, as illustrated in Fig. 3.3a. Owing to the preservation of mode group identity upon propagation through the MMF, this limitation can be tackled by redistributing the power in the proximal far-field (intensifying the higher-order mode groups) in such a way as to achieve a uniform power distribution in the distal

far-field, as depicted in Fig. 3.3b, and thus harness the full NA of the fibre.

## 3.3 Methods

The experimental system was designed to exploit the high-NA MMF introduced above in Section 3.1, which was significantly affected by MDL. In conventional designs, as that shown in Fig. 2.1 (configuration 3), the SLM is relayed onto the back focal plane of the coupling objective, i.e. a plane conjugate to the proximal far-field. The only way to achieve the power distribution required to compensate for the MDL in this arrangement would be to discard the excessive power in the central zones, which would be associated with a significant power loss. Thus, the design used projected the SLM onto the fibre facet, as by altering the spatial content of the holographic modulation in this arrangement it is possible to redistribute the power at will between the central and peripheral zones of the proximal far-field without incurring in such prohibiting power loss.

This system employed a LC-SLM for the holographic modulations, as a high power efficiency was critical for the experiments detailed in the following Chapters 4 and 5.

### 3.3.1 Experimental layout

The experimental setup used in these experiments is depicted schematically in Fig. 3.4. It consisted of two decoupled parts, the first dividing the laser beam into a signal and a reference beams and coupling them into single-mode polarisation-maintaining fibres (PMF1 and PMF2, respectively). Besides carrying the signal and reference beams to the main subset of the system, PMF1 and PMF2 served also as Gaussian spatial filters.

Lenses L1 and L2 formed a telescope to demagnify the size of the beam originating from the laser source (IPG Photonics YLR-10-1064-LP-SF, 1.064 µm wavelength, continuous-wave Yb fibre laser), and half-wave plate HWP1 aligned its polarisation with the polarisation axis of the Faraday optical isolator OI. Half-wave plate HWP2 together with polarising beamsplitter cube PBS1 allowed controlling the total amount of power propagating in the optical system (the excess power was diverted towards beam block BB), whereas half-wave plate HWP3 and polarising beamsplitter cube PBS2 allowed adjusting the power ratio between the signal and reference beams, which were coupled into PMF1 and PMF2 via aspheric lenses L3 and L4, respectively.

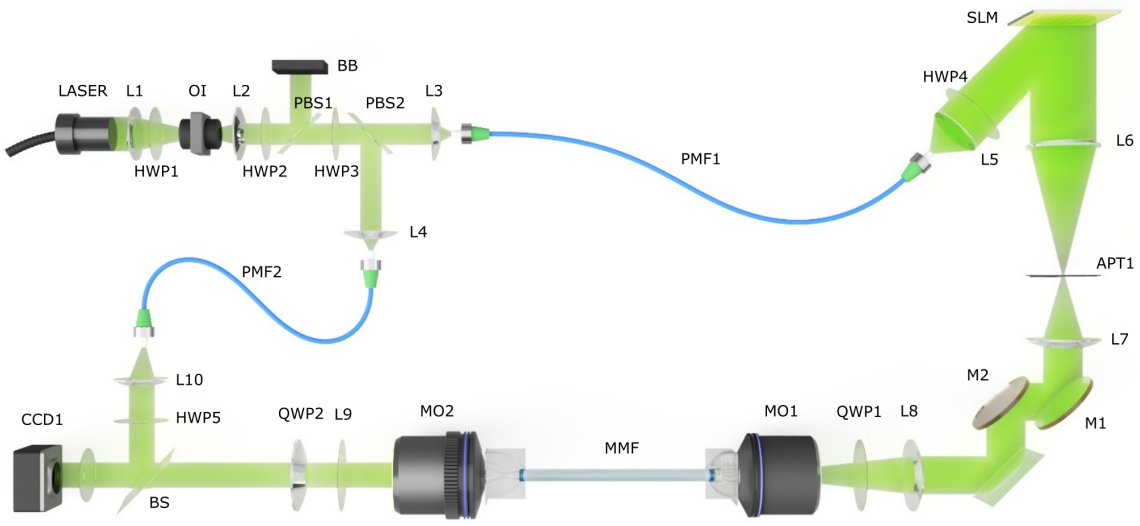


FIGURE 3.4: Experimental setup for high-resolution focussing through a multimode fibre.

The signal beam leaving PMF1 was collimated and expanded by lens L5 to overfill the liquid-crystal spatial light modulator SLM (BNS HSPDM512-800-1064) under a small angle of incidence. Half-wave plate HWP4 was used to align the polarisation of the signal beam with the polarisation axis of the SLM. Aperture APT1, placed in the far-field of the SLM, isolated the first diffraction order while blocking the remaining. Lenses L6 and L7 were placed in a $4f$ configuration and imaged the first diffraction order of the holograms generated at the SLM onto dielectric mirror M1. Lens L8 and oil-immersion microscope objective MO1 (Olympus UPlanFL, 100×, 1.30 NA) were also placed in a $4f$ configuration and further relayed the holograms from M1 to the input facet of the multimode fibre MMF. The combination of L6, L7, L8 and MO1 chosen ensured the necessary demagnification (370×) of the phase holograms such that their image size matched the dimensions of the MMF core. M1, being conveniently placed in a plane conjugate to the input fibre facet, served as a steering mirror to finely adjust normal incidence onto MMF.

The distal end of the MMF was immersed in a water droplet held by a custom-made cuvette which was in contact with water-immersion microscope objective MO2 (Olympus UPLSAPO60xW, 60×, 1.20 NA) through a water-index-matching medium. MO2 in combination with tube lens L9 imaged the MMF output facet (or, in general, any desired calibration plane at a given distance from the endface) onto camera CCD1 (Basler piA640-210gm) with a magnification of 67×. MO2

was mounted on a piezo nanopositioner (Mad City Labs Nano-F100) allowing a precise focussing adjustment.

Quarter-wave plates QWP1 and QWP2 were used to convert the polarisation state of the signal beam from linear-to-circular and circular-to-linear, respectively, as circularly-polarised modes are shown to be better preserved upon propagation in MMFs [38].

Non-polarising beamsplitter cube BS combined the signal and reference beams at CCD1 for the interferometric measurement of the transmission matrix. Half-wave plate HWP5 was used to align the polarisations of the signal and reference beams.

### 3.3.2 Holographic methods

**Measurement of the transmission matrix** The transmission matrix was measured using the procedure introduced in Subsection 2.4.1, choosing a set of $38 \times 38$ truncated plane waves as the basis of input modes (Fourier-domain based approach, Subsection 2.4.3). The output modes were heavily oversampled, consisting of a square grid of $100 \times 100$ points at the calibration plane which were conjugate to individual pixels in the CCD detector. For each input mode, the interferometric response was sampled in steps of $\pi/2$ over two full phase cycles, i.e. $\delta\phi = \pi/2$ and $n = 8$ in Eq. (2.5).

**Measuring the mode-dependent loss** Due to the strong MDL inherent to the MMF used, different mode-groups (i.e. waveguide modes having similar propagation constants) experience distinct degrees of attenuation upon propagation. This translates into a non-uniform power distribution in the spectrum of the output modes which limits the available NA, as illustrated schematically in Fig. 3.3. In order to pre-compensate the MDL all input plane-wave modes, labelled as $(k, l)$, were sequentially coupled into the fibre, and the output power at the CCD for each one of them was integrated. This allowed measuring the intensity map $I^{k,l}$, which has been normalised to the maximum value, containing the information of the optical transmittance of the different mode groups. Figure 3.5 shows the azimuthally-averaged intensity distribution $I^{k,l}$ for different fibre lengths, as a function of the normalised spatial frequency $n \sin\theta = {}^{k_t}/_{k_0}$, where $k_t = \sqrt{k_x^2 + k_y^2}$

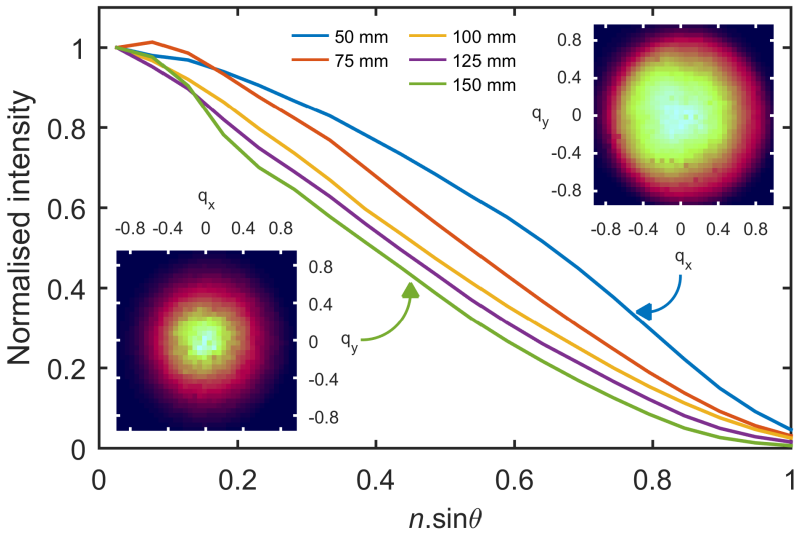


FIGURE 3.5: Measurements of the mode-dependent transmission. Azimuthally averaged measurements of the mode-dependent transmission for fibre segments of varying length, from 50 mm to 150 mm. The inset figures show normalized measurements of the spatial-frequency dependent intensity for fibres with length 50 mm (top-right) and 150 mm (bottom-left).

is the transverse component of the wave-vector and $k_0 = 2\pi/\lambda$ its *in vacuo* magnitude. The insets in Fig. 3.5 display the mode-dependent transmission $I^{k,l}$ measured for the longest and shortest fibres (150 mm and 50 mm long), as a function of the normalised spatial frequencies $q_{x,y} = k_{x,y}/k_0$.

**Generating a single diffraction-limited focus** Upon measurement of the transmission matrix $t^{k,l}_{u',v'}$, where $k$ and $l$ are the positions indices in Fourier space of the input modes $(k, l = -19, \ldots, 18)$ and $u$ and $v$ are the position indices of the output modes in the calibration plane $(u, v = 1, \ldots, 100)$, a single diffraction-limited focus can be generated at a particular position $(u', v')$ by applying to the LC-SLM the phase-only modulation given by Eqs. (2.11) and (2.12). The fact that a phase-only modulation is used instead of the measured complex modulation (i.e. amplitude and phase) results in a noisy background, as only $\pi/4 \simeq 78.5\%$ of the output power can be controlled in this manner [27]. On the other hand, the implementation of amplitude modulation would involve further power loss and decrease the overall efficiency, thus reducing the available output power.

To pre-compensate the MDL, this design of the system allows to perform spectral amplitude modulation, implemented in the Fourier domain as:

$$h_{u',v'}\left(\frac{M}{2}+Mf_x+k,\frac{M}{2}+Mf_y+l\right)=\frac{t^{k,l}_{u',v'}}{\sqrt{I^{k,l}}} \tag{3.1}$$

in place of Eq. (2.11).

### 3.3.3 Calibration of the imaging pathway

In order to characterise the focussing ability, it is necessary to accurately determine the size of the generated foci, which requires knowledge of the magnification of the imaging pathway. The microscope objective lens used (Olympus UPLSAPO60xW, 3 mm focal length) together with the chosen tube lens (200 mm focal length) should yield a magnification of 67×. However, its actual value might differ from this, possibly owing to small differences from the nominal values in the focal lengths, but especially due to the fact that the wavelength used (1064 nm) might lie outside the designed working spectrum of the microscope objective.

The actual magnification was calibrated using a negative 1951 USAF resolution target. Each element of this resolution chart is composed of vertical or horizontal bars, with widths equal to their separation. Images of several groups of the target were recorded using the imaging pathway of the system, and those with vertical bars were fitted to:

$$f\left(x,y\right)=\sum_{m=0}^{5}\left(-1\right)^m\frac{a}{2}\mathrm{erf}\left(b\left[\left(x-\left[x_0+mw\right]\right)\cos\alpha+y\sin\alpha\right]\right)+c \tag{3.2}$$

where erf() is the error function, $x$ and $y$ are the image coordinates (in pixel units), and $a$, $b$, $c$, $\alpha$, $x_0$ and $w$ are the free parameters of the fitted surface. In particular, $w$ corresponds to the line width and separation (in pixel units) of the projected image of the element onto the CCD detector. Elements with horizontal bars were fitted to a surface given by an analogous expression by replacing $x \leftrightarrow y$.

Figure 3.6 plots the actual line separation (in line pairs per mm) of each element of the resolution target against their corresponding line separation measured at the CCD detector. The magnification of the imaging pathway, given by the slope of the linear fit, was estimated as $65.7 \pm 0.5$ with a 95% confidence interval.

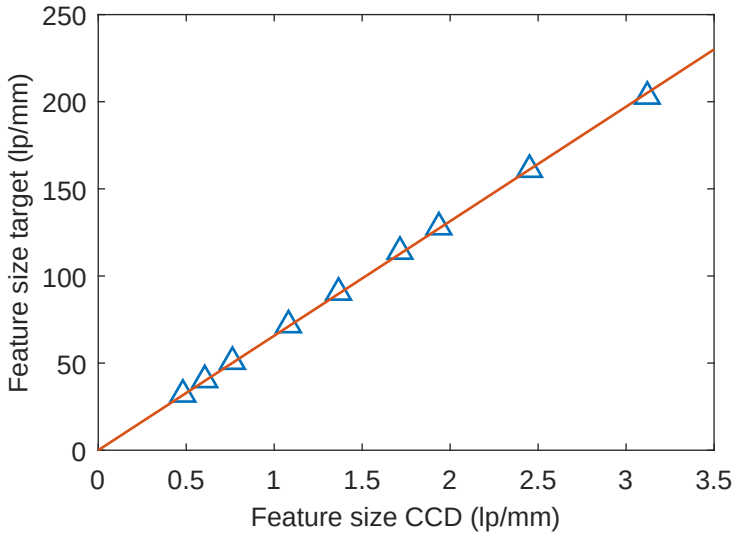


FIGURE 3.6: Calibration of the imaging pathway. Actual size of the elements of the 1951 USAF resolution target, in lines per millimetre (lp/mm), versus the size of their corresponding image at the CCD detector. The magnification is given by the slope of the fitted line, which is $65.7 \pm 0.5$ (with a 95% confidence interval).

## 3.4 Results

To assess the achievable NA of the system as well as the impact of the MDL compensation, 91 focal-point (FP) modes were sequentially generated across the distal fibre facet for each measurement of the TM (Fig. 3.8a). The procedure was repeated for several TM measurements and for varying length of the same fibre segment which was successively re-cleaved to reduce its size in increments of 25 mm.

Since the intensity distribution of each FP mode spanned over the 8-bit dynamic range of the CCD camera, three images were taken for each FP mode with exposure times of 0.1 ms, 1 ms, and 10 ms (Fig. 3.7a) in order to reconstruct its intensity distribution $I(x, y)$, where $x$ and $y$ denote the Cartesian coordinates of the image in pixel units. One of such intensity distributions is shown in Fig. 3.7b,c, prior and after MDL compensation. The FP mode shown was generated at a radial distance 2.25 µm (from the fibre axis) and distance 2.0 µm from the fibre facet, through a 50 mm long fibre. Each intensity distribution $I(x, y)$ is fitted to a 2-D Airy disk distribution:

$$f(x, y) = a \left( \frac{2J_1(\rho)}{\rho} \right)^2 + b, \tag{3.3}$$

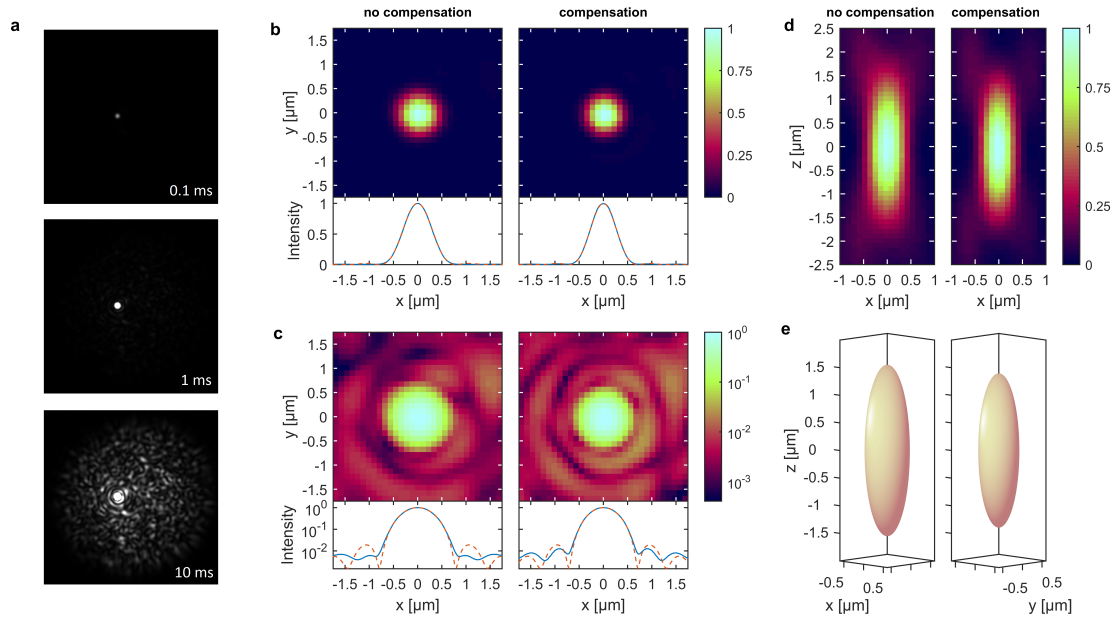


FIGURE 3.7: High-resolution focussing through a multimode fibre. **a,** Three images taken with different exposure times (0.1 ms, 1 ms, and 10 ms) for reconstructing the intensity profile of the focal-point (FP) mode. **b,c,** Transverse intensity profile of a FP mode, with and without MDL compensation, and comparison of the azimuthally-averaged intensity profile with the fitted Airy disk intensity distribution. The NA of the FP mode is enhanced from $0.82 \pm 0.01$ (prior to MDL compensation) up to $0.91 \pm 0.01$ (after MDL compensation). **d,** Longitudinal profile of the intensity distribution of the same FP mode. **e,** Ellipsoid fitted to the level surface with intensity corresponding to $1/e$ of the maximum value. The fibre length was 50 mm.

where $J_1$ is the Bessel function of the first kind of order one, and

$$\rho = \frac{\sqrt{(x-c)^2 + (y-d)^2}}{e}, \tag{3.4}$$

with $a$, $b$, $c$, $d$, and $e$ being free parameters ($a$ measures the amplitude, $b$ the average speckle background, $c$ and $d$ the Cartesian coordinates of the centre of the distribution, and $e$ its width). In Fig. 3.7b,c, the fitted distribution $f(x,y)$ is also compared with the azimuthally averaged $I(x,y)$. With the knowledge of the pixel size in the CCD (7.4 μm) and the calibrated magnification of the imaging pathway (65.7×), the diameter of the Airy disk, taken as first-zero-ring in Eq. (3.3), can be estimated as $d_{\text{Airy}} = 2 \cdot 3.8317 \cdot 7.4\,\mu\text{m} \cdot e/65.7$. The corresponding effective NA can then be retrieved as $\text{NA} = {}^{1.22\lambda}/_{d_{\text{Airy}}}$, where $\lambda$ is the wavelength in free space (1064 nm).

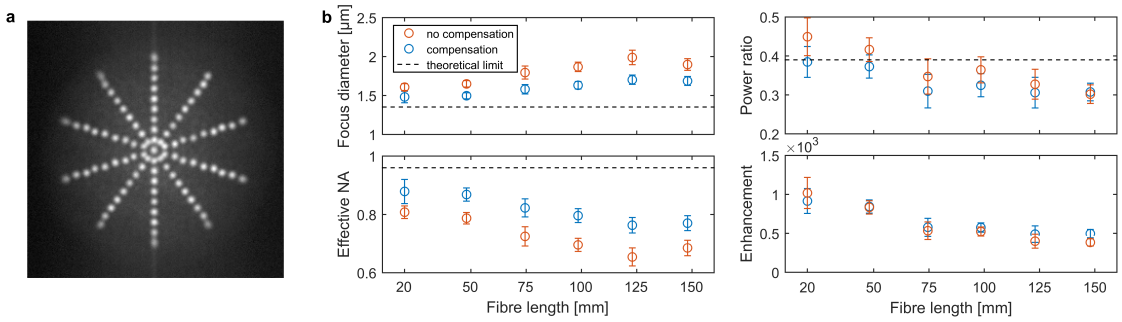


FIGURE 3.8: Influence of MDL compensation on focussing through a high-NA multimode fibre. **a,** Summed image of 91 points sequentially created across the distal fibre facet. **b,** Influence of the MDL compensation on the Airy disk diameter, effective NA, power ratio, and enhancement for varying length of the MMF.

By scanning the imaging objective axially in steps of 100 nm, it was possible to reconstruct the 3-D intensity profile of the FP mode shown in Fig. 3.7b,c. Figure 3.7d shows the longitudinal profile of this FP mode, where the spot size in the axial direction is approximately 3.8 times larger than its lateral dimension, both with and without MDL compensation. Figure 3.7e shows the 3-D structure of this FP mode as an ellipsoid fitted to the level surface corresponding to $1/e \simeq 0.37$ of the maximum intensity.

In addition to the achievable NA, which determines the volumetric confinement of light, other parameters quantifying the uncontrolled background are also important in view of proposed applications. The *power ratio* (PR) is the fraction of total output power at the distal fibre facet which is contained in the FP mode, and can be estimated as $\mathrm{PR} = \sum_{x,y}[f(x,y) - b] / \sum_{x,y} I(x,y)$. The *enhancement*, defined as the ratio between the maximum intensity of the generated FP mode and the average speckle background, can be calculated as $\eta = a+b/b \simeq a/b$. Figure 3.8b summarises the results of this study, showing the focus diameter (defined as the first zero-ring in the Airy disk), effective NA, power ratio, and enhancement for each fibre length tested. The MDL-compensation increased the NA in average by 0.09. However, the ability to generate FP modes with higher NA decreases with increasing fibre lengths. As the optical loss grows exponentially with the fibre length, the transmitted power by the higher-order mode groups becomes comparable to the noise level in case of the longer fibres. This translates into increasingly larger errors in the measurement of the MDL, thus limiting the efficiency of the compensation for the higher spatial frequencies which leads to a decreasing

available NA with increasing fibre length. The power ratio across all fibre lengths is around $(33 \pm 4)\%$ with and $(37 \pm 5\%)$ without MDL compensation. The theoretical limit for the power ratio in the case of phase-only modulation is shown to be $\pi/4 \simeq 78.5\%$ [27]. However, in the presence of complete polarisation mixing, and if only one polarisation state is controlled (as in this case) this value is further reduced by half, being $\pi/8 \simeq 39.3\%$ – a value in good agreement with the experiments.

## 3.5 Discussion

The generation of high-NA, diffraction-limited foci is of great importance in the field of holographic micro-endoscopy exploiting MMFs, not just to further increase the attainable resolution of previously demonstrated imaging modalities, but also as the enabling principle for other techniques relying on high-NA foci with low aberrations, such as optical tweezers. Efforts in this direction have taken place over the past few years, by means of alternative fibre terminations as well as air-clad photonic-crystal fibres.

In this chapter, a new class of all-solid, step-index MMFs based on compound "soft-glasses", together with the system design and methodologies introduced, allowed generating foci with unprecendented output NAs. The system design differs from standard geometries by making use of immersion layers in the light coupling to the fibre, as well as relaying the holograms generated at the SLM directly onto the input fibre facet. This allowed implementing a set of holographic approaches to compensate for the strong MDL inherent to the new fibre type and harness the available NA almost completely. The focussing ability of the system reaches NAs exceeding 0.80 for 100 mm-long fibres, and up to $0.88 \pm 0.04$ through 20 mm-long fibres, an increase of $\approx$0.27 with respect to the highest value previously reported in the literature. Using Rayleigh's criterion for defining the spatial resolution (i.e. the radius of the first dark ring of the Airy disk), this corresponds to a resolution limit of $0.74 \pm 0.04\,\mu$m at the 1064 nm wavelength. Using shorter wavelengths can further increase the resolution, not just because the resolution limit scales inversely with the wavelength, but also because the NA of this MMF is increased in the visible region of the spectrum, reaching values up to 1.1 at 400 nm. It is worth noting, however, that the number of guided modes supported by the MMF increases substantially for shorter wavelengths, making the measurement of the TM more challenging. At 400 nm, the same fibre supports

approximately 15 000 modes, i.e. about 10 times the number of modes compared to the 1064 nm wavelength. Accordingly, the size of the TM is increased by $10^2$, making its measurement impractical using the LC-SLM used here. This could, in principle, be circumvented by using the alternative MEMS-based technology of light modulators, DMDs, which are capable of reaching modulations speeds two orders of magnitude higher.

# Chapter 4

# 3D Holographic Optical Tweezers through a Multimode Fibre

The previous chapter described how to generate high-NA focussed light outputs through a high-NA multimode fibre. In this chapter, such capability is exploited to demonstrate three-dimensional optical confinement and manipulation of small dielectric objects at the micrometre scale by means of holographic optical tweezers (HOT) delivered through the fibres.

The methodology and results of modelling the stability of the optical traps presented in this chapter are based on simulations by Martin Šiler, Institute of Scientific Instruments (Brno, Czechia).

The contributions from the author of this Thesis to the work presented in this chapter consisted of: (i) assessment of the working distance of fibre-based optical tweezers, (ii) implementation of the modifications to the experimental setup, (iii) implementation of the holographic methods for optical manipulation, and (iv) performing the demonstrations of optical manipulation of complex 3D arrangements of microparticles and of optical manipulation within hardly-accessible environments.

The contents of this chapter form part of the following publication: **I. T. Leite**, S. Turtaev, X. Jiang, M. Šiler, A. Cuschieri, P. St. J. Russell, and T. Čižmár, *Three-dimensional holographic optical manipulation through a high-numerical-aperture soft-glass multimode fibre*, Nature Photonics 12(1), 33–39 (2018).

## 4.1 Stability of the optical tweezers

In order to confirm whether the high-NA foci would be sufficient to allow optical confinement of dieletric microparticles, the following approach was used to

assess the minimum NA required for stable trapping.

An angular spectrum decomposition was used to describe the intensity profile close to the beam focus. The angular spectrum description of light focusing through an objective lens corresponds to the Debye approximation of the diffraction of a convergent spherical wave on a circular aperture [97, 98]. The components of the electric field vector polarised along the $x$ axis are given by:

$$E_x(x,y,z) = -\frac{i}{2}k\left(I_0 + I_2\frac{x^2-y^2}{x^2+y^2}\right), \tag{4.1}$$

$$E_y(x,y,z) = -ikI_2\frac{xy}{x^2+y^2}, \tag{4.2}$$

$$E_z(x,y,z) = -kI_1\frac{x}{\sqrt{x^2+y^2}}, \tag{4.3}$$

where

$$I_0(r,z) = \int_0^{\theta_{\max}} A(\theta)\sin\theta\,(1+\cos\theta)\,J_0(kr\sin\theta)\exp(ikz\cos\theta)d\theta, \tag{4.4}$$

$$I_1(r,z) = \int_0^{\theta_{\max}} A(\theta)\sin^2\theta\,J_1(kr\sin\theta)\exp(ikz\cos\theta)d\theta, \tag{4.5}$$

$$I_2(r,z) = \int_0^{\theta_{\max}} A(\theta)\sin\theta\,(1-\cos\theta)\,J_2(kr\sin\theta)\exp(ikz\cos\theta)d\theta, \tag{4.6}$$

and $r = \sqrt{x^2+y^2}$ denotes the radial distance from the optical axis $z$, $k = 2\pi n/\lambda$ is the wave vector ($n$ being refractive index of surrounding medium and $\lambda$ vacuum wavelength of the trapping beam), and $\theta_{\max}$ is the angular aperture of the focusing optics which is connected to the fibre numerical aperture by $\mathrm{NA}_{\mathrm{fibre}} = n\sin\theta_{\max}$. Furthermore, $J_\nu$ denotes the Bessel function of the first kind and $\nu$-th order, and the angular amplitude distribution in the aplanatic projection follows [97]

$$A(\theta) = A_0\sqrt{\cos\theta}. \tag{4.7}$$

The constant $A_0$ corresponds to the focusing of a plane wave; however, as the energy distribution of the beam is not uniform over all angles, an apodization function was employed, parametrised by the filling factor $f_0$ [98], i.e.

$$A(\theta) = A_0\exp\left(-\frac{1}{f_0^2}\frac{\sin^2\theta}{\sin^2\theta_{\max}}\right)\sqrt{\cos\theta}. \tag{4.8}$$

The circularly polarised beam was realised by the interference of two beams that are linearly polarised along the $x$ and $y$ axes with a mutual phase shift of $\pi/2$. $A_0$

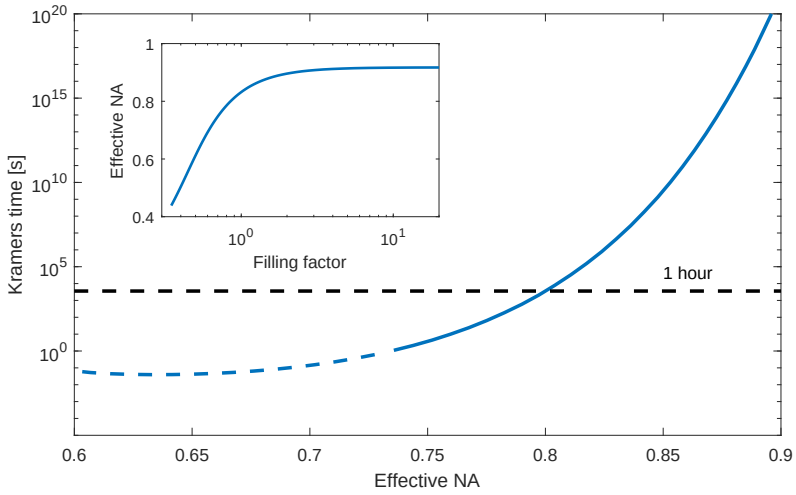


FIGURE 4.1: Kramers time of residence of a 1.5 µm-diameter silica particle in the optical trap as a function of trap effective NA, for a trapping power of 1 mW. The dashed portion of the curve depicts the region in effective NA where $\tau_K < 1$ s and the black dashed line marks 1 h limit. The inset figure shows the effective NA as a function of filling factor $f_0$.

is obtained from the beam power. The Airy disk diameter was determined for a wide range of $f_0$ using the procedure described previously in Section 3.4, and the effective NA obtained as a function of the filling factor, as shown in the inset of Fig. 4.1.

The next step was the calculation of the optical force, $F$, acting on a silica bead ($n_{\text{silica}} = 1.45$, 1.57 µm diameter) immersed in water and placed into various axial locations, $z$. This allowed confirming the existence of a trapping location as well as estimating the trap stiffness $\kappa = -\partial F/\partial z$ and the depth of the potential well $\Delta U$. No trapping location existed for filling factors $f_0 < 0.4$, which corresponds to effective NAs smaller than 0.6. The long term time stability of the optical trap can be evaluated by means of the Kramers time [99]:

$$\tau_K = \frac{2\pi\beta}{\sqrt{|\kappa\kappa_{\text{edge}}|}} \exp\left(\frac{\Delta U}{k_B T}\right), \tag{4.9}$$

where $\beta$ is the hydrodynamic drag, $\kappa$ the trap stiffness, $\kappa_{\text{edge}}$ the stiffness (force differential) at the trap edge and $k_B$ and $T$ the Boltzmann constant and thermodynamic temperature. Figure 4.1 shows the Kramers time as a function of the effective NA for a trapping power of 1 mW. For low NAs (under 0.74) the trapping depth was quite shallow and the particle escapes the trapping region by

Brownian motion in less than 1 s, highlighted as a dashed curve in Fig. 4.1. Additionally, the black dashed line marks the Kramers time of 1 h, the lower limit when it was considered that the optical confinement was stable enough to perform long-term observations of trapped objects, which corresponds to effective NAs larger than 0.80.

## 4.2 Working distance

The size of distal focal-point (FP) modes generated at the fibre facet is limited by the NA of the fibre. As seen in the previous chapter, the presence of mode-dependent loss (MDL) can reduce the effective NA of such foci, but by redistributing the power in the spectrum of input modes it is possible to compensate for this detrimental effect. Nevertheless, the effective NA of distal FP modes also depends on the location (both axial and transversal) where they are to be generated. If the calibration plane, for which the wavefront shaping procedure is perfomed, is set away from the distal fibre facet by a certain working distance, the accessible field-of-view increases, while the effective NA decreases [23, 30]. This trade-off can be understood considering that, regardless of the location of the calibration plane, the amount of spatial information that can be conveyed by the fibre (connected to the number of guided modes it sustains) remains the same.

The effective NA of FP modes in front of the fibre facet can be estimated under the ray-optics approximation, considering a highly multimode fibre (i.e. having a large $v$-number) with a core much larger than the wavelength. The collection efficiency of a point source is thus determined by the intersection of the acceptance cone of the fibre with the spherical sector by which the fibre core is seen from that point. Choosing the origin $(r,z) = (0,0)$ of the coordinate system at the centre of the fibre facet, the effective output NA is given by:

$$\mathrm{NA}\,(r,z) = n \sin\left(\frac{\alpha_1 + \alpha_2}{2}\right), \tag{4.10}$$

where $\alpha_1$ and $\alpha_2$ are the angles of the optical rays from a given point in space $(r,z)$ to the edges of the fibre core $(r,z) = (a,0)$ and $(r,z) = (-a,0)$, measured with respect to the optical axis, given by :

$$\alpha_1 = \begin{cases} \min\left\{\alpha_{\max}, \tan^{-1}\left(\frac{a-r}{z}\right)\right\} & , r < a \\ \max\left\{-\alpha_{\max}, \tan^{-1}\left(\frac{a-r}{z}\right)\right\} & , r \geq a \end{cases} \tag{4.11}$$

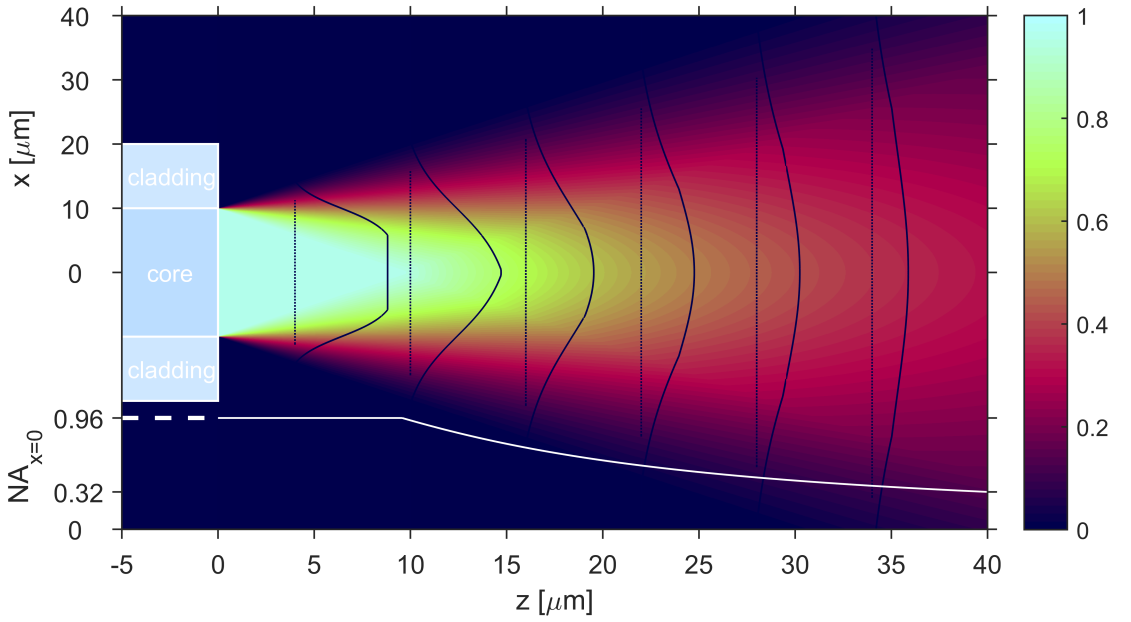


FIGURE 4.2: Numerical aperture of distal focused spot modes at varying working distances. The lower plot shows the evolution of the NA along the optical axis and the series of dark subplots illustrate the NA profiles across different axial planes in front of the fibre.

$$\alpha_2 = \begin{cases} \max\left\{-\alpha_{\max}, \tan^{-1}\left(\frac{a+r}{z}\right)\right\} & , r < -a \\ \min\left\{\alpha_{\max}, \tan^{-1}\left(\frac{a+r}{z}\right)\right\} & , r \geq -a \end{cases} \tag{4.12}$$

where it is taken into account that incidence angles $\alpha_1$ and $\alpha_2$ exceeding in magnitude the acceptance angle $\alpha_{\max} = \sin^{-1}\left(\mathrm{NA}_{\mathrm{fibre}}/n\right)$ are not coupled into the fibre.

Figure 4.2 shows the available NA in front of the output fibre endface, estimated in the ray-optics approximation using the parameters $\mathrm{NA}_{\mathrm{fibre}} = 0.96$ and core radius $a = 10\,\mu\mathrm{m}$ for the fibre and $n = 1.333$ (water) for the refractive index of the surrounding medium.

The lower plot shows the evolution of the on-axis NA with increasing distance $z$ from the fibre endface, given by:

$$\mathrm{NA}\left(r = 0, z\right) = \min\left\{\mathrm{NA}_{\mathrm{fibre}}, n \sin\left[\tan^{-1}\left(\frac{a}{z}\right)\right]\right\}, \tag{4.13}$$

which is constant with the value $\mathrm{NA}_{\mathrm{fibre}}$ up to the distance $a/\tan\alpha_{\max}$ and decreases as $na/z$ at large axial distances ($z \gg a$).

The available NA reaches the maximum value dictated by the fibre within the conical volume in front of distal fibre endface with base coinciding with the

fibre core and apex on the optical axis at a distance of approximately 10 µm from the fibre. Accordingly, the volume of maximum NA is approximately 1000 µm$^3$. The trapping experiments were performed with the calibration plane located at a distance $z \simeq 4$ µm from the fibre facet (represented in Fig. 4.2 by the left-most NA axial profile) to allow for access of the particles as well as depth of manipulation in the axial direction. At this working distance, the region of maximum NA is approximately 12 µm in diameter.

## 4.3 Methods

### 4.3.1 Experimental setup

The experimental system detailed in Subsection 3.3.1 was modified to allow an improved control over the power of the trapping beam, as well as to include a side-view imaging pathway. The resulting experimental setup is illustrated in Fig. 4.3.

A portion of the signal beam was diverted by nonpolarising beamsplitter cube BS towards a power detector PD, allowing to assess the optical power leaving the MMF. This required calibrating the transmittance of both BS and microscope objective MO2 at the 1064 nm wavelength.

Half-wave variable retarder HWVR was used to control the amount of power in the trap site (in closed-loop with feedback from PD), as it allowed introducing in the signal beam a polarisation component orthogonal to the polarisation axis of the LC-SLM with variable amplitude, whose power remained in the zero diffraction order and was thus filtered out by aperture APT1.

Dichroic mirror DCM placed in the optical path allowed coupling incoherent light from LED source LED1 into the fibre to provide uniform illumination on the trapped objects for *en face* imaging by CCD1. Short-pass filter SPF1 was placed to block the trapping beam. Lens L11 imaged aperture APT2 onto the back-focal plane of microscope objective MO1.

LED source LED2, lenses L12 and L13, diffuser DIFF, and aperture APT3 comprised a pseudo-Köhler illumination for side-view imaging by lens L14 onto camera detector CCD2. Short-pass filter SPF2 was used to filter-out scattered light from the trapping beam.

The trapping experiments were performed inside a water-filled sample cuvette manufactured in-house from microscope coverslips (thickness #1.5, 0.17 mm), as depicted in the inset of Fig. 4.3. In addition to supporting the

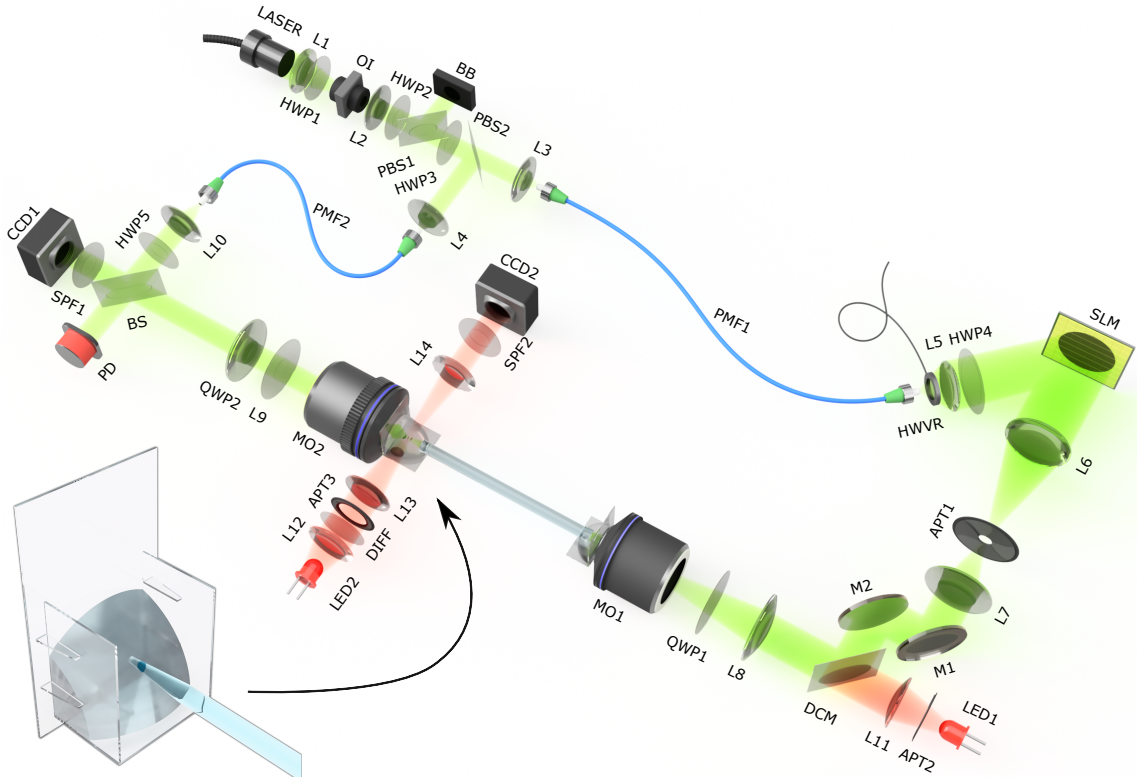


FIGURE 4.3: Experimental setup for holographic optical manipulation through a multimode fibre, including a side-view imaging pathway.

water droplet, the cuvette provided three flat surfaces, one in contact with microscope objective MO2 through a water-index-matching immersion layer, and the remaining two for side-view illumination and imaging. The cuvette was open on the top and on the side opposite to MO2 to facilitate access of the fibre. Additionally, the cuvette was held by a three-axis micrometre translation stage allowing its relative motion with respect to the fibre, whose position remained fixed.

The fibre segment used was approximately 65 mm in length. Based on the results shown in Fig. 3.8, such length should guarantee an effective output NA greater than the 0.80 value required for stable optical confinement (Section 4.1), provided MDL compensation is applied.

### 4.3.2 Holographic methods

#### Simultaneous generation of multiple tweezers

Trapping and manipulating assemblies of particles by optical tweezers requires generating multiple trap sites simultaneously [54, 100], or beam-steering between the multiple locations at rates typically greater than ≈10 kHz, e.g. by employing acousto-optic deflectors [101].

The generation of multiple diffraction-limited foci simultaneously at the output positions $(u_q, v_q)$, where $q = 1, \ldots, N$ is the index of each output mode ($N$ is the total number of output foci), can be achived by appling to the LC-SLM the phase-only information of the complex superposition of the complex modulations [27], i.e.:

$$H_N(x,y) = \arg\left(\sum_{q=1}^{N} \sqrt{a_q}\mathcal{F}^{-1}\left[h_{u_q,v_q}(x,y)\right]\right), \tag{4.14}$$

with $h_{u_q,v_q}$ obtained from Eq. (3.1), which includes MDL compensation, and $a_q$ are the required intensity contributions for the composition of output modes.

#### Relocation of the optical tweezers

**Lateral displacement of trap sites** The basis of output modes formed a square grid of diffraction-limited foci separated by ≈0.23 µm. Since this separation was much smaller than the spot size of the foci ($1/e^2$ diameter greater than 1 µm), by switching between the phase-only modulations at the LC-SLM generating two consecutive calibrated sites, i.e. from $(u', v')$ to $(u' \pm 1, v')$ or $(u', v' \pm 1)$, a trapped particle remained confined in the new location. In this way, a trapped particle could be displaced laterally to any calibrated location by sequentially generating all calibrated foci between the initial and final positions. Naturally, assemblies of particles confined by multiple tweezers could also be displaced independently and at the same time by sequentially applying phase-only modulations given by (4.14) to the LC-SLM, with each complex modulation $h_{u_q,v_q}$ being sequentially replaced by $h_{u_q \pm 1, v_q}$ or $h_{u_q, v_q \pm 1}$.

**Axial control of generated foci** Owing to the remarkable cylindrical symmetry of fibre-optic waveguides, the longitudinal component of the wavevector (i.e. the propagation constant) is very well conserved through the fibre (axial memory effect) [23]. Thus, a quadratic phase added to the spatial spectrum of the input

modes is preserved and, therefore, found in the spatial spectrum of the output modes, resulting in a defocus and axial displacement of the diffraction-limited foci. A given output focus located at $(u', v')$ can thus be repositioned axially by modifying the complex modulation Eq. (2.11) as:

$$h_{u',v'}\left(\frac{M}{2}+Mf_x+k,\frac{M}{2}+Mf_y+l\right)=t^{k,l}_{u',v'}\exp\left[ib\left(k^2+l^2\right)\right], \tag{4.15}$$

where $b$ is a scalar whose magnitude gives the amount of defocussing, and whose sign defines the direction of defocussing ($b > 0$ produces a negative defocus, towards the fibre facet, while $b < 0$ gives rise to a positive defocus away from the fibre facet). More generally, when generating multiple output FP modes simultaneously, while also pre-compensating the MDL, a defocus could be applied to each of them individually as:

$$h_{u_q,v_q}\left(\frac{M}{2}+Mf_x+k,\frac{M}{2}+Mf_y+l\right)=t^{k,l}_{u_q,v_q}\frac{\exp\left[ib_q\left(k^2+l^2\right)\right]}{\sqrt{I^{k,l}}}, \tag{4.16}$$

which, in combination with Eq. (4.14), resulted in the independent axial relocation of the multiple optical tweezers generated simultaneously.

### 4.3.3 Optical trapping procedures

The optical trapping experiments started with placing a segment of the MMF into the optical pathway, which is detailed in Fig 4.3. The first diffraction order signal of holographically modulated laser light was isolated in the proximal far-field plane and relayed through an oil-immersion medium into the proximal end of the fibre. A water-filled custom-made cuvette composed from 170 µm thick coverslips (inset of Fig. 4.3) was mounted in the system to immerse the distal end into the liquid. Water-immersion microscope objective MO2 was translated towards the cuvette from the opposite side with a water-index-matching medium being applied in-between the cuvette-objective interface. The optical signal leaving the objective's back aperture was further imaged on a CCD using a tube lens. With this configuration, the MDL and TM were measured by employing the holographic methods detailed in Subsection 3.3.2. A suspension of silica microspheres (Duke Standards$^{TM}$, $1.57 \pm 0.02$ µm diameter) was pipetted into the cuvette and let diffuse within the water medium. For the following procedures, the trapping wavelength was blocked using a dielectric short-pass filter and incoherent illumination of the sample was provided by an LED at a visible wavelength. For

the *en face* view, the illumination signal was delivered through the high-NA fibre (and the proximal microscope objective MO1), whereas for the side-view a stand-alone Köhler illumination pathway was provided. In all cases when the side-view imaging pathway was used, the water-immersion objective was displaced away from the cuvette to allow sufficient space for the side-view imaging lens L14. A single optical trap or an assembly of traps was generated via computer-controlled SLM modulation which, based on the *en face* view or side-view camera-feedback, was permanently adjusted manually from a LabView-based interface in order to confine the corresponding amount of particles diffusing into the vicinity of the distal end of the high-NA fibre.

To demonstrate holographic manipulation within complex, hardly-accessible environments, a semi-opaque cavity was mounted on a lateral wall of the custom-made cuvette. The particles were first trapped using the *en face* imaging pathway, and the cuvette containing the cavity was then manipulated with respect to the distal fibre end by a manual 3-D positioning stage.

## 4.4 Results

### 4.4.1 Trapping and manipulation of complex particle arrangements

The technique allowed both simultaneous generation of multiple trap sites and independent control of their position in all three dimensions. Figure 4.4a shows the *en face* view of nine silica particles trapped in a square-grid arrangement in front of the fibre endface. Incoherent light for illumination was delivered to the scene also by the fibre core, which is visible as a blurred bright disk in the background. The tilt and skew control of the particle array and the consequent change in axial distance from the fibre facet manifests as a change in brightness of the trapped particles.

In Fig. 4.4b, the three-dimensional dynamic control of the optical tweezers is demonstrated by trapping eight particles simultaneously in a rotating cube arrangement. The images show snapshots of a video recording of the rotating structure (full video available as Supplementary Video 1 at [102]).

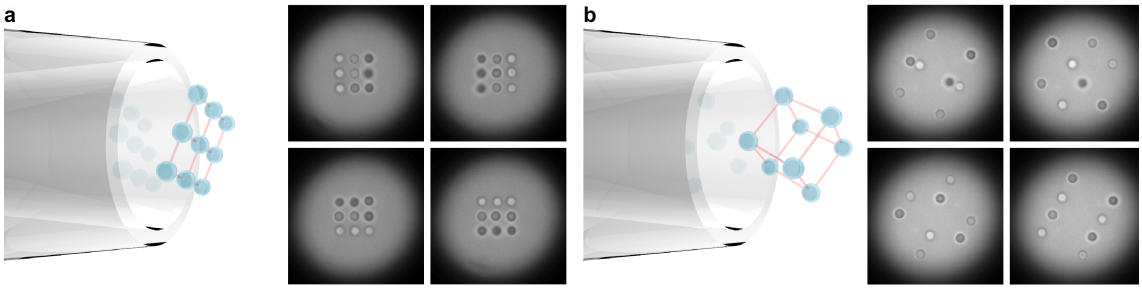


FIGURE 4.4: Multiple holographic tweezers trapping and manipulation of (**a**) nine particles in a square-grid arrangement and (**b**) eight particles forming a rotating three-dimensional cube. The difference in appearance among the particles arises from their varying axial positions relative to the focal plane of the imaging microscope objective (particles appearing "brighter" are at a greater distance from the fibre endface). Incoherent light for illumination is also delivered through the fibre core, which is visible as the blurred disk in the background. Scale bars, 5 µm.

### 4.4.2 Optical manipulation inside complex environments

Having a lateral footprint of 35 µm, the fibre-based HOT could allow access to optically inaccessible cavities through small channels. To verify this, a small semi-opaque tube of roughly polished poly(methylmethacrylate) (PMMA) with an open channel ≈125 µm wide was employed. Figure 4.5 shows side-view images of simultaneous optical manipulation of two particles, recorded while the fibre was inserted into the tube (see also Supplementary Video 4 available at [102]).

### 4.4.3 Resilience to fibre bending

In practical applications of HOT delivered *in vivo* by a MMF, a certain degree of bending may be unavoidable, for instance due to mechanical stress induced by the surrounding tissue or to the dynamic nature of living specimens (e.g. due to breathing, heart beating, etc.). To demonstrate the HOT's resilience to bending of the fibre, an experiment was conducted in which a 65 mm long fibre was subject to bending while trapping a silica microsphere. The bending occured in the unheld distal segment of the fibre (≈15 mm long) by means of a controlled pressure applied near the fibre endface by a motorised stage moving upwards, as depicted in Fig. 4.6. Notably, the particle remained confined by the HOT even when the fibre endface was translated by 2 mm, the maximum allowed by the conditions

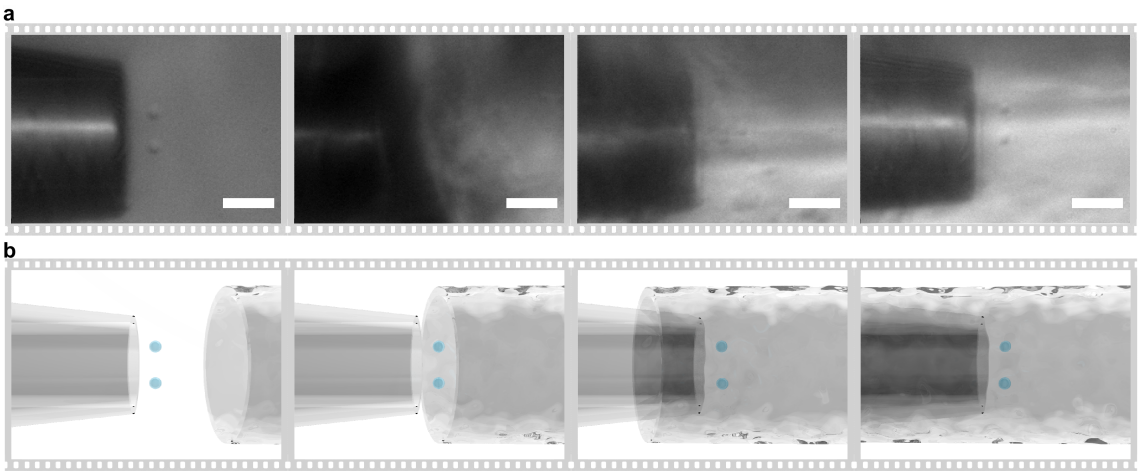


FIGURE 4.5: Optical manipulation of two particles inside a turbid cavity comprising a complex, hard-to-access environment. Scale bars, 10 µm.

of the experiment, thus inducing a radius of curvature of 5 cm. The full video recording is available at [102] as Supplementary Video 5.

## 4.5 Discussion

Fibre-based optical manipulation often relies on engineered terminations to achieve focussing [61]. In most cases, such optical traps are static, i.e. do not allow positioning of the confined objects with respect to the fibre, and lack confinement in the axial direction due to insufficient NA. Demonstrated fibre-based optical tweezers, providing three-dimensional confinement, relied on the combination of multicore fibres with micro-fabricated structures to combine light from such cores into a high-NA focus [62, 63, 103]. Yet, these approaches come with increased instrument footprints, and lack the flexibility offered by HOT.

This chapter showed the first demonstration of 3D holographic optical manipulation of micro-objects using a single-core fibre. Moreover, the lensless MMF probe allowed the delivery of HOT in a region spanning almost the entire area of the fibre core.

The versatility of the instrument was further demonstrated by simultaneous and dynamic 3D manipulation of large assemblies of microparticles, allowing the independent relocation of the tweezers with respect to each other and to the fibre. The footprint of the instrument could be made as small as 35 µm in diameter,

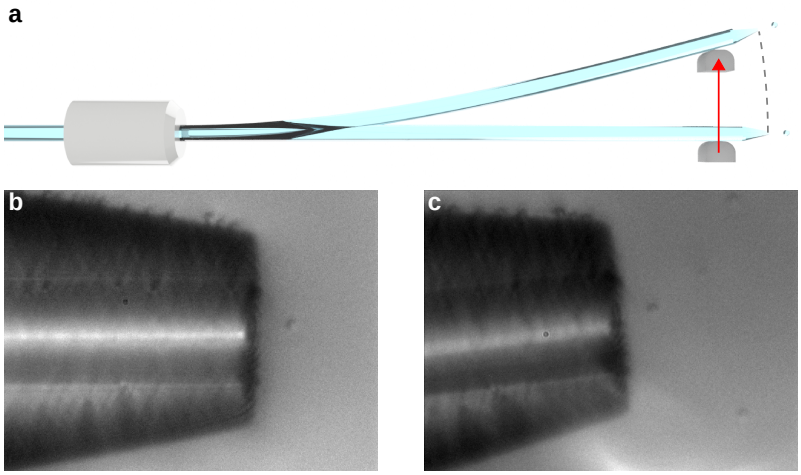


FIGURE 4.6: Resilience of HOT to fibre bending. **a,** A static HOT confining a silica microsphere (1.5 µm diameter) was delivered through a fibre with length 65 mm. The unheld distal portion of the fibre (15 mm long) was initially straight and was then progressively bent due to the force applied by a motorised stage moving upwards. **b,c,** Side-view images of the trapped particle in the initial, straight conformation of the fibre (**b**), and in the final, bent conformation (**c**), corresponding to a vertical displacement of 2 mm and a radius of curvature of 5 cm.

allowing to demonstrate the manipulation of micro-objects within a turbid cavity which was inaccessible to bulk optics. Optical manipulation inside such complex environments opens new perspectives for studies using HOT delivered through micro-endoscopes in complex environments, including studies *in vivo*.

A possible concern might relate to the influence of fibre bending in the quality of the optical traps. This was addressed by a demonstration suggesting that the HOT are sufficiently resilient for practical implementations, including *in-vivo* applications, where small deformations might be induced in the fibre during insertion of the endoscopic probe, or due to the dynamic nature of living tissue. Furthermore, it has been shown separately that such deformations can be corrected based on numerical modelling of light propagation through MMFs [38].

# Chapter 5

# Characterisation of the Optical Tweezers

This chapter is devoted to the study of the performance of the fibre-based holographic optical tweezers (HOT) demonstrated in the previous chapter.

Calibrating the optical tweezers encompasses measuring their stiffness for known values of the optical power, which usually requires knowing the trajectory described by the trapped objects due to Brownian motion. To this end, an algorithm for extracting the 3D trajectory of a trapped particle from high-speed recordings is introduced here. The performance of the HOT in terms of the stiffness versus power characteristics was studied for different lengths of the multimode fibre (MMF). Additionally, a method allowing the precise nano-scale relocation of the trap sites was developed, as this comprises a crucial aspect in view of practical applications in biophotonics. Lastly, the influence of temperature on defocussing of the HOT is also addressed.

The concept and methodologies of the particle tracking algorithm presented in this chapter was developed by Tomáš Čižmár (University of Dundee, United Kingdom), the doctoral advisor of this Thesis.

The contributions from the author of this Thesis to the work presented in this chapter consisted of: (i) performing the calibration of the HOT, (ii) implementation of the holographic methods for precise positioning of HOT, (iii) performing the experiments assessing positioning resolution of trapped microparticles, and (iv) contribution to the data analysis.

The contents of this chapter form part of the following publication: **I. T. Leite**, S. Turtaev, X. Jiang, M. Šiler, A. Cuschieri, P. St. J. Russell, and T. Čižmár, *Three-dimensional holographic optical manipulation through a high-numerical-aperture soft-glass multimode fibre*, Nature Photonics 12(1), 33–39 (2018).

## 5.1 Calibration of the optical tweezers

In aqueous media, optically confined particles are subject to Brownian motion so that recording their 3-D trajectories can be used to analyse the strength (stiffness) of the optical trap. Since fibre-based HOT is incompatible with the standard approach of back-focal-plane interferometry [104], an algorithm was developed to extract the particle's positions from high-speed video recordings.

### 5.1.1 Particle tracking using symmetry and principal component analysis

Video recordings of confined particles were obtained with the *en face* imaging pathway at a frame-rate of 1 kHz and field of view of $200 \times 40$ pixels. For each video recording of a trapped particle, a background recording (i.e. with no particles in the field of view) was also taken, whose time-averaged signal was subtracted from each frame of the particle recording in order to eliminate effects originating from non-uniformities in the illumination signal. A time-averaged frame of the whole record was used to determine the approximate lateral position of the particle, and all frames were cropped to a region of $32 \times 32$ pixels around it.

#### Tracking of the transverse position

Since the particles used were highly regular spheres, their images produced azimuthally invariant signals over a uniform background, as shown in Fig. 5.1a. To determine the lateral ($x$ and $y$) coordinates of the particle in a given frame of the video recording, the shift-property of the Fourier transform was employed to translate the particle's image to the centre of the frame, so the whole frame features the best horizontal and vertical symmetries (Fig. 5.1b). The shift-property of the Fourier transform is very suitable for this operation since, even for non-integer pixel shifts, it does not affect the spatial content of the images.

The optimisation procedure consisted in the following: The one-dimensional Fourier transform of each row of the image data was calculated, and then multiplied by a phase term $\exp\left(i2\pi\mathbf{x}^{d_x}/N\right)$, where $d_x$ is the horizontal shift to be applied in units of pixels, $\mathbf{x}$ is a vector of pixel indices $(-N/2, -N/2+1, \ldots, N/2-2, N/2-1)$ and $N$ is the size of the vector ($N = 32$). The inverse Fourier transform was calculated from the result to obtain each row of the spatially shifted frame. The optimisation procedure varied the amount of $d_x$ in order to obtain a

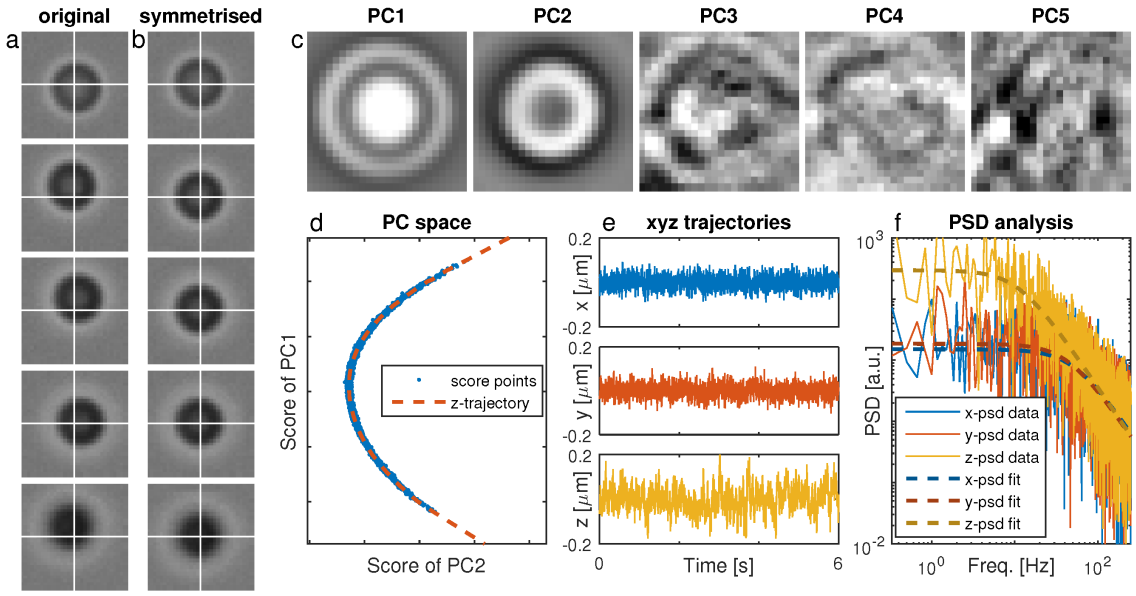


FIGURE 5.1: Particle tracking based on symmetry and principal component analysis. **a,** Sequence of original frames from a high-speed video recording the Brownian motion of an optically trapped microsphere. **b,** Symmetrised frames of **a**. **c,** First five principal components of the symmetrised record. **d,** $z$-coordinate trace in the score space of the two main principal components. **e,** Retrieved time evolution of all three Cartesian coordinates of the trapped particle. **f,** PSD and its Lorentzian fit (in logarithmic scale) for each coordinate.

frame yielding the minimum difference (least-squares-sum) from its mirror image. The value $d_x$ maximising the mirror symmetry of the images corresponds to the $x$ coordinate of the particle for the actual frame in pixel units. This same procedure was then applied to each column of the image to symmetrise the frame vertically and obtain the $y$ coordinate of the particle. Alternatively, the optimisation procedure could search for both lateral coordinates simultaneously using a two-dimensional Fourier transform; however, this was found to be more computationally demanding making the algorithm significantly slower.

The shift amount immediately yields the lateral $x$ and $y$ trajectories, which can be calibrated using the known magnification of the imaging pathway. This procedure also provides a stack of symmetrised video-frames where the shape of the particle's image changes only with axial position ($z$).

**Tracking of the axial position**

As there is only one degree of freedom dictating the changes in the particle's image shape, the $z$ coordinate can be extracted using principal component analysis (PCA), a multivariate algorithm commonly used to reduce the dimensionality of datasets. Changes to signals of individual pixels in symmetrised frames are, due to the axial motion of the particle, correlated. PCA transforms this multidimensional space of pixel signals into a set of orthogonal vectors (principal components) in such way that the first principal component contains the maximum variance of the data set, the second principal component contains the next most significant variance, and so on.

All symmetrised frames were reshaped into $1 \times N^2$ vectors comprising the columns of a two-dimensional matrix containing the whole (symmetrised) video recording. The Matlab inbuilt function "pca" was used to calculate the principal component (PC) vectors as well as the PC scores – i.e. the projections of each frame onto the PC vectors – for each frame of the recording. Figure 5.1c shows the first five principal component vectors, reshaped back into $32 \times 32$ pixels images.

Only the first two principal components (PC1 and PC2) feature azimuthal symmetry and are not overwhelmed by noise; therefore, it can be assumed that these variances carry most of the information about the axial position of the particle. The PC scores of these two principal components can be plotted against each other (see Fig. 5.1d), featuring a clear trace in the two-dimensional PC space which is associated with the axial motion. Each point in this trajectory corresponds to an individual frame of the video recording. The $z$ position can be found by parametrising and calibrating this score-space trajectory.

The first step in the parametrisation of the trajectory was searching for the "origin" point featuring the highest concentration of the score points in PC space. Secondly, the algorithm searched for a circular (soft-apertured) subspace whose centre is displaced from the "origin" by a (very small) fixed distance, also featuring the highest concentration of score points from all such subspaces at the fixed radius from the "origin". This provided the tangential vector to the $z$ trajectory. The "origin" point was then translated sequentially in small increments along the tangential vector, with each step including a correction to the tangential vector. Because the optimisation function searching for the optimal angle of the tangential vector has two local maxima for two opposite angles (corresponding to forward and backward displacements), a weighting term providing preferential movement in the forward direction (with respect to the previous iteration)

was included to prevent reversing the motion and cycling. In this way, the algorithm followed the trajectory in small increments until reaching a location where the concentration of score points is below a certain threshold. When one end of the trajectory was reached, the tangential vector was reversed and the "origin" point was sequentially moved backwards, while keeping record of its actual position in PC space. Additionally, the obtained $z$ trajectory was extrapolated at each end beyond the location of the score points and re-sampled in such way that the distance between neighbouring points was significantly smaller compared to the expected inaccuracy, estimated from the dispersion (thickness) of the score-points around the $z$ trajectory. This equidistant $z$ trajectory is represented as a dashed red curve in Fig. 5.1d. Finally, the closest point to the reconstructed $z$ trajectory was found for each score point, whose index was associated with the uncalibrated $z$ coordinate.

#### Calibration of the trajectory

The lateral coordinates, $x$ and $y$, can be calibrated directly from the known pixel size of the CCD detector (7.4 µm) and measured magnification of the imaging pathway ($65.7 \pm 0.7$). The axial ($z$) coordinate can be calibrated using the $x$ and $y$ trajectories via energy equipartition, by assuming that the Brownian motion at high frequencies is not affected by the trap, and therefore remains isotropic along all Cartesian coordinates. A typical particle trajectory is shown in Fig. 5.1e, where all three Cartesian coordinates are plotted against time.

### 5.1.2 Estimation of the optical trap stiffness

The stiffnesses of the optical tweezers were assessed using the *power spectrum analysis* of the trajectory of trapped particles, which is often regarded as the most reliable method for spherical particles [49, 104].

The power spectrum density (PSD) in each Cartesian direction (Fig. 5.1f) is calculated as the squared absolute value of the Fourier transform of the corresponding trajectory component, i.e. $\mathrm{PSD}_j = \left|\mathcal{F}\left(r_j\right)\right|^2$, where $r_j$ is the $j$-th component ($x$, $y$ or $z$) of the trajectory $\mathbf{r}\left(t\right)$. The corner frequencies $f_c$ can be extracted from the power spectra by fitting to a Lorentzian function:

$$\mathrm{PSD} = \frac{a}{f^2 + f_c^2}, \tag{5.1}$$

where $f$ is the frequency coordinate of the Fourier spectrum and $a$ and $f_c$ are parameters of the fit. The optical stiffness $\kappa$ can be recovered from the corner frequency parameter $f_c$ as:

$$\kappa = 2\pi\beta f_c, \tag{5.2}$$

where $\beta$ is the hydrodynamic drag given by [104]:

$$\beta = \frac{6\pi\nu a}{1 - \frac{9}{16}\frac{a}{h} + \frac{1}{8}\left(\frac{a}{h}\right)^3 - \frac{45}{256}\left(\frac{a}{h}\right)^4 - \frac{1}{16}\left(\frac{a}{h}\right)^5} \tag{5.3}$$

which already includes Faxen's law correction, $\nu$ is the viscosity of the medium, $a$ is the radius of the particle and $h$ is the distance from the particle's centre to the fibre facet.

Throughout the analyses of the optical stiffnesses, shown in the following section, the particles were confined at a distance of ≈4 µm away from the fibre. This value has been used as the estimate of the particle displacement from the fibre facet. However, increasing trapping power caused further axial relocation of the trap sites away from the fibre, as shown in Fig. 5.7c. The hydrodynamic drag constant $\beta$ was not corrected for this effect since, even in the most affected cases, the imprecision in the estimate of $h$ only caused a small inaccuracy to the resulting stiffness values (up to 5%).

## 5.2 Stiffness versus power characteristics

### 5.2.1 Methods

These experiments used the same apparatus in the final configuration described in Section 4.3.1, which is illustrated in Fig. 4.3. The optical trapping procedures were also identical to those detailed in Subsection 4.3.3, with a single HOT being generated at a distance of 4 µm from the distal fibre facet using the holographic methods introduced in Subsection 3.3.2 which include pre-compensation of the mode-dependent loss (MDL).

The power of the trapping beam was changed in a step-wise manner, by using the half-wave variable retarder HWVR in closed feedback with power detector PD. For each value of power, a video recording of the same trapped particle (1.5 µm-diameter silica microsphere) was taken at an acquisition rate of 1 kHz using the *en face* imaging pathway. In each time the HOT power was modified,

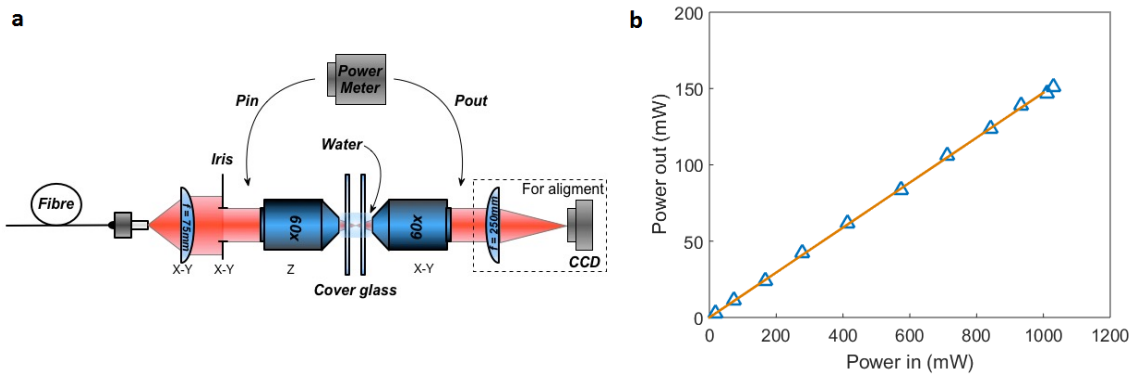


FIGURE 5.2: Calibrating the microscope objective transmission at the 1064 nm wavelength. **a,** Schematic of the experimental configuration. **b,** Transmitted power through two identical objectives as function of the input power.

the imaging microscope objective MO2 was re-positioned axially using a piezo-actuated $z$-translation mount due to the axial relocation of the trap site. The displacement of the trap site was found in this manner by maximising the image contrast of the trapped particle, and was logged for later analysis. To exclude the possibility of performance degradation by mechanical drift of the alignment components, the measurements were taken for increasing followed by decreasing trapping power with the same measurement of the transmission matrix (TM) of the fibre. In the end of the measurements, the particle was released and video recordings of the background were taken at all previously logged axial positions. This entire procedure was controlled by a Labview routine allowing faster and more reliable data acquisition. These experiments were repeated for five measurements of the TM and for several lengths of fibre, using the same fibre segment which was successively recleaved in increments of ≈25 mm.

### Output power calibration (transmittance of MO2 and BS)

In order to estimate the optical power leaving the output fibre facet at any given moment during the experiments, it was necessary to measure the transmittance of the imaging microscope objective MO2 as well as the fraction of power diverted by the non-polarising beamsplitter cube BS towards power detector PD, at the 1064 nm wavelength used.

The transmittance of MO2 was measured using two identical microscope objectives in the arrangement depicted in Fig. 5.2a. Two microscope coverslips and

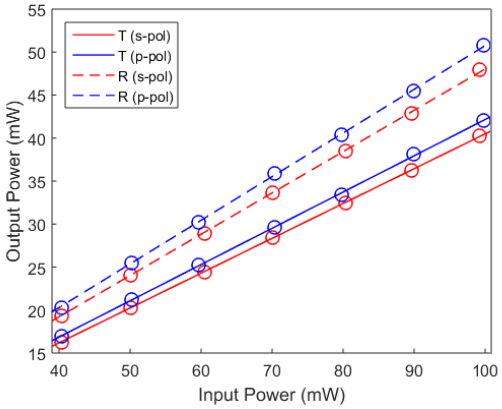


FIGURE 5.3: Calibrating beamsplitter cube at 1064 nm wavelength. Transmitted ($T$) and diverted ($R$) power by the non-polarising beamsplitter cube as function of input power.

water-index-matching immersion oil were placed in-between. The beam was expanded and collimated by a lens (75 mm focal length) to overfill the back-focal aperture of the first microscope objective. An iris diaphragm was placed in the path to exactly fill the back-focal aperture. A tube lens (250 mm focal length) and a CCD detector were used to guarantee the correct alignment of the second microscope objective. The input power was measured between the iris and the first microscope objective, whereas the output power was measured immediately after the second microscope objective. These measurements are plotted in Fig. 5.2b.

The transmitted and diverted power by beamsplitter cube BS was measured for both *s*- and *p*-polarisation states. A half-wave plate and a linear polariser were employed at the input facet of BS to control both the orientation of polarisation and the incident power. The power detector was placed in one of two positions: (1) to measure the diverted power and (2) to measure the transmitted and incident powers (the latter by removing the beamsplitter cube). A cage cube mount (Thorlabs CCM1-4ER) made it simple to insert and remove the beamsplitter cube during the measurements, which are shown in Fig. 5.3.

The transmittance of microscope objective MO2, given by the slope of the fitted line in Fig. 5.2b, was estimated as $(38.5 \pm 0.1)\,\%$. The fraction of diverted power by beamsplitter cube BS was estimated as $(48.0 \pm 0.5)\,\%$ for *s*-polarised light, and $(50.8 \pm 0.4)\,\%$ for *p*-polarised light. Therefore, in the presence of complete polarisation mixing in the multimode fibre, the diverted power by BS is $49.4\% \pm 0.6\%$ for unpolarised light. The power leaving the output fibre facet is thus $5.26 \pm 0.07$ times larger than that measured by power detector PD.

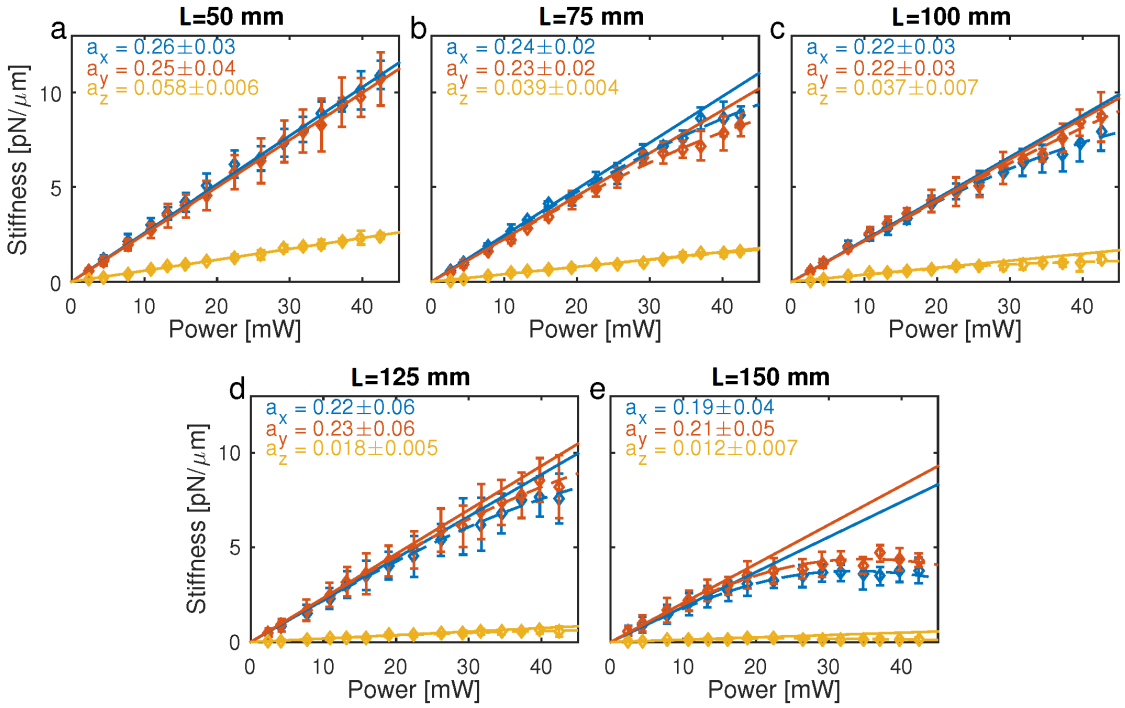


FIGURE 5.4: Trap stiffness for each coordinate as function of the total optical power leaving the distal fibre end, for various fibre lengths ($L$). The fitting parameter $a$ (in units of $\mathrm{pN\,\mu m^{-1}\,mW^{-1}}$) reveals the initial linear trend of the curves. Error bars represent standard deviations over five measurements.

### 5.2.2 Results

Figure 5.4 summarises the study of trap stiffness along each coordinate for varying fibre lengths. The same fibre segment was used throughout the experiment, re-cleaving it several times to shorten its length in increments of 25 mm. To verify that the axial confinement was indeed due to optical forces, the fibre was oriented horizontally so as to eliminate the gravitational effects in the axial direction. The trapped objects were silica microspheres of 1.5 µm in diameter and the wavelength was 1064 nm. Since the dependencies visibly depart from the ideal linear trend, the data sets have been fitted to:

$$\kappa = aP \exp\left(-\frac{P^2}{b^2}\right), \tag{5.4}$$

where $\kappa$ is the stiffness, $P$ is the output optical power, and $a$ and $b$ are two fitting parameters.

Increasing fibre lengths clearly degraded the trap stiffness, particularly in the

axial direction. At the same time, the power dependence also visibly departs from linearity, especially for longer fibres. Both these effects are connected to MDL. Even with MDL compensation the available NA was reduced (as shown in Fig. 3.8); moreover for larger fibres the MDL compensation intensifies the power of the lossy mode groups, which leads to a temperature increase due to optical absorption. This causes changes to the TM and consequently reduces the quality of the optical traps. Comparing these results with the state-of-art HOT systems based on high-NA microscope objectives, these fibre-based HOT are roughly one order of magnitude weaker. This is in good agreement with our expectations – the optical traps only carry about 33% of the output optical power (Fig. 3.8) and, although sufficient for 3-D confinement, the available NA is ≈20–30% lower.

## 5.3 Positioning precision

Practical applications of optical tweezers frequently require fine positioning of trapped objects with nanometric precision [50–53]. At first sight, this might seem inconsistent with the construction of the transmission matrix from output modes organised in a square grid of diffraction-limited foci spaced by ≈0.23 µm. Indeed, the lateral relocation of the optical tweezers detailed in Subsection 4.3.2 consisted in dividing the lateral trajectory into ≈0.23 µm steps by switching between consecutive pre-calibrated sites. This problem could be resolved by realising that any diffraction-limited focus at an arbitrary position on the distal fibre endface can also be expressed as a linear superposition of the distal (focal-point) FP modes. For instance, by weighting the relative amplitudes of two neighbouring FPs, it is possible to generate a focus anywhere between them.

Such a restriction does not apply to axial positioning, as this is achieved by adding an arbitrarily small amount of defocus to the proximal far-field, as previously discussed in Subsection 4.3.2.

### 5.3.1 Holographic methods

Since the separation between the calibrated sites of the grid of output modes was much smaller than the spatial extent (spot size) of each one of them, the fine positioning of a distal FP mode between such calibrated locations could be achieved by generating two consecutive modes simultaneously, say $(u', v')$ and $(u' + 1, v')$,

by applying to the LC-SLM the phase-only modulation:

$$H(x,y) = \arg\left(a\mathcal{F}^{-1}\left[h_{u',v'}\right] + (1-a)\, e^{i\delta}\mathcal{F}^{-1}\left[h_{u'+1,v'}\right]\right), \tag{5.5}$$

where $h_{u',v'}$ is the far-field complex modulation given by Eq. (3.1) and $\delta$ is the phase delay between the two output modes, which needs to be corrected for them to interfere constructively:

$$\delta = \arg\left(\sum_{k,l}\left(t^{k,l}_{u',v'}\right)^* \cdot t^{k,l}_{u'+1,v'}\right), \tag{5.6}$$

where $^*$ denotes the complex conjugate. The modulation in Eq. (5.5) results in a distribution of the optical field corresponding to a single FP whose central position can be finely tuned by the relative amplitude $a$ of the two output modes.

### 5.3.2 Effect on achievable output NA

In order to reposition the HOT with nanometric precision to locations between calibrated FP modes, the relative amplitudes of two neighbouring FPs generated simultaneously were weighted as described by Eq. (5.5). Naturally, this procedure works when the separation between the FPs is much smaller than their spot size, while as the FP separation approaches their size the generated focus broadens, translating into a decreasing NA and stiffness of the HOT. To verify the limits of this approach, the focus relocation was simulated for FP separations ranging from 0.1 µm to 0.8 µm using a TM calculated for a fibre having the same parameters as that used in the experiments. The resulting intensity distribution was fitted to an Airy disk distribution deformed elliptically, allowing to retrieve the actual position of the focus as well as its effective NA (in the direction of the major axis, i.e. parallel to the line segment connecting the two FPs) as it is relocated. The results of the simulations for the FP separations of 0.2 µm and 0.3 µm are shown in Fig. 5.5a,b, whereas the results for the whole range of FP separations are available at [102] as Supplementary Video 6.

These simulations were complemented with experimental measurements where the spacing between consecutive FPs was ≈0.23 µm. At each position, the intensity distribution of the relocated focus was reconstructed from three images taken at distinct exposure times (as detailed in Section 3.4) and fitted to an elliptical Airy disk as in the simulations. Figure 5.5c shows the experimental data averaged over five measurements. For the 0.23 µm FP separation used

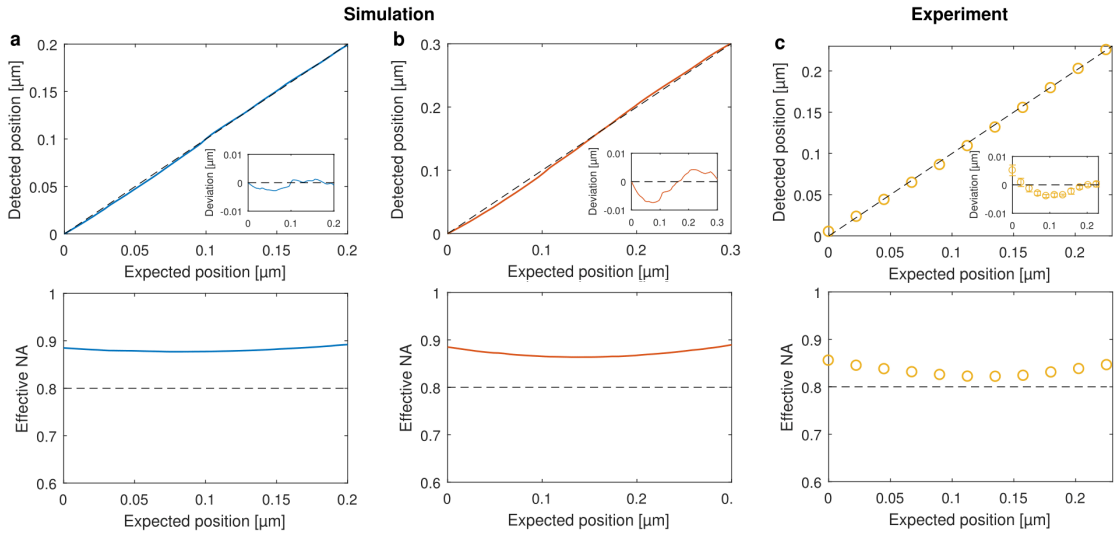


FIGURE 5.5: Detected central position and effective NA of a focus created by coherent superposition of two neighbouring FP output modes as a function of its expected central position. **a,b,** Simulated data using a FP separation of **(a)** 0.2 µm and **(b)** 0.3 µm. **c,** Experimental data with consecutive FP modes spaced by 0.23 µm. The errorbars in **(c)** are smaller than the data markers. The horizontal dashed line indicates the NA value of 0.8 required for stable optical confinement and the inset figures show the deviation between the detected and expected positions of the focus as it is relocated between the two FPs.

in this work, the effective NA was almost kept constant during the HOT fine positioning, and the total deviation from the expected trajectory was smaller than 5 nm. Moreover, the precision of each step along the trajectory was 1.8 nm for the step size used (23 nm). It is worth noting that the presence of MDL in the 65 mm-long fibre used in the measurements, not taken into account in the simulations, is responsible for a visibly smaller effective NA in the measurements when compared with the simulated data.

### 5.3.3 Results

To demonstrate the fine positioning, these principles were applied to relocate a trapped particle (1.5 µm silica microsphere) in a step-wise manner, both axially and laterally, while recording its position. Figure 5.6 reveals that even 5 nm lateral steps, approximately 50 times smaller than the separation between output modes, can still be resolved. Due to weaker localisation in the $z$ direction, the smallest resolvable axial steps are five times larger.

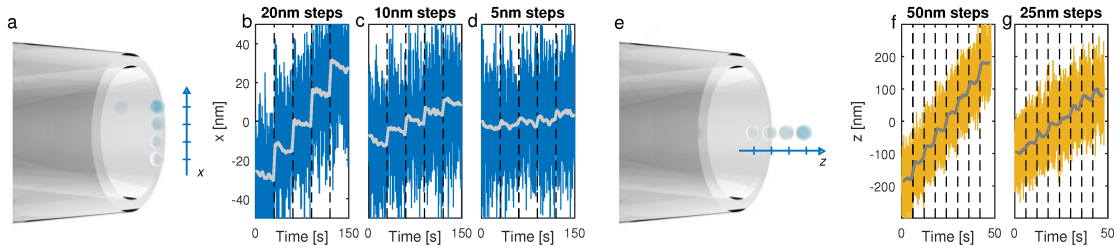


FIGURE 5.6: **a-d,** Sequential relocation of the trap site along the lateral direction, in increments of 20 nm (**b**), 10 nm (**c**), and 5 nm (**d**). **e-g,** Sequential relocation of the trap site along the axial direction in increments of 50 nm (**f**) and 25 nm (**g**).

## 5.4 Effect of temperature on defocus

Power absorption in the MMF leads to an increase in its temperature which modifies the measured TM. This was seen in the characterisation of the optical tweezers, where the increasing optical power causes the trap site to displace axially by a few micrometres (Fig. 5.7c). Remarkably, in the first instance the quality of trap is seen to be well preserved as the trap stiffness increases linearly with the optical power, especially in the case of fibres with lengths smaller than 100 mm (Fig. 5.4). This lead to the hypothesis that, in the first instance, optical absorption gives rise to a defocus of the FP modes, and further increasing power leads to the degradation of the TM.

In order to test this, the TM of a ≈170 mm-long fibre was measured under varying temperature. With respect to the system shown in Fig. 3.4, the setup was modified into an upright configuration with the fibre bent 180° between the two microscope objectives at the bottom. This allowed immersing ≈100 mm of the fibre in a thermal bath whose temperature was controlled in closed-loop and could be kept constant with a precision of 0.01 °C.

Comparing the several TM measurements at different temperatures with the one obtained at room temperature (21.84 °C) it was found that to generate the same distal FP modes, the proximal far-field is modified by a quadratic phase – a defocus – with magnitude proportional to the temperature difference. Figure 5.7a shows this phase difference, averaged for all distal FPs in each measurement of the TM, and compares it with a fitted quadratic phase. Figure 5.7b shows that the dependence of averaged defocus with temperature is very linear, having a slope of $\approx 0.19\lambda/°C$ for the fibre length used. A temperature increase can therefore be compensated to some extent by applying a defocus on the proximal field,

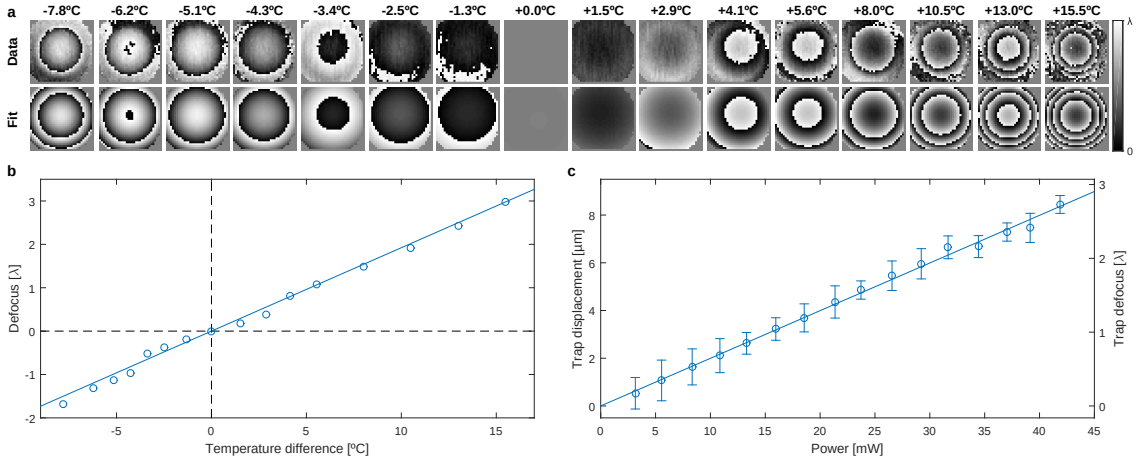


FIGURE 5.7: Effect of temperature on the transmission matrix. **a,** Phase difference in the proximal far-field with respect to the TM measurement at room temperature, and fit to a quadratic phase. **b,** Corresponding defocus (in units of wavelength) as a function of the temperature difference. **c,** Axial displacement of the trap site and corresponding defocus during the optical tweezers characterisation for a fibre with length 150 mm.

without the need for re-measuring the TM. Conversely, by retaining the same TM measurement without modifying the proximal field, such defocus will manifest in the distal field as an axial displacement of the FP modes generated, due to conservation of the longitudinal components of the wavevectors.

In order to link the defocus due to power absorption with the temperature increase, a study of the axial displacement of a confined particle as a function of the optical power was conducted using a fibre of similar length (150 mm). This dependence, shown in Fig. 5.7c, is also very linear with a slope of $\approx 0.065\lambda/\text{mW}$. Although the temperature is not distributed uniformly along the fibre, these two studies provide a coarse estimate that the fibre temperature increases by $\approx 0.3\,^{\circ}\text{C}$ per mW, for the fibre length used.

## 5.5 Discussion

The quantitative analyses presented in this chapter reveal that the performance of the fibre-based trapping system is not significantly lower than in standard geometries of optical tweezers relying on bulk objective lenses. The approaches introduced here also allow the independent positioning of trapped particles with nanometre-scale precision in all three dimensions. The particle confinement

strength and fine positioning control were both well maintained, suggesting that the system can be used without severe compromises. Both studies confirm that the trapping performance should indeed be sufficient for advanced applications in biomedical research.

The particle tracking method based on symmetry and principal component analysis allowed retrieving the 3D trajectory of trapped particles from 2D video records with sufficient precision, conveniently without the need for pre-calibrating their axial positions from pre-recorded off-focus images of a particle fixed onto a coverglass [105].

The effect of temperature on the transmission matrix of a MMF was also addressed. It was shown that, in a first instance, the quality of generated foci seems to be remarkably well preserved for temperature changes below 10 °C. Such changes in temperature, however, give rise to a defocus which translates to an axial displacement of the foci. This could be counteracted by applying an opposing defocus to the proximal far-field of the holographic modulations.

# Chapter 6

# In-vivo Deep-brain Fluorescence Imaging via a Multimode Fibre

This chapter demonstrates a system for high-speed fluorescence imaging through a multimode fibre (MMF), capable of acquiring 7-kilopixel images at a rate of 3.5 frames per second.

The MMF-based micro-endoscopy system was used to demonstrate deep-brain imaging *in vivo* in a mouse animal model, via endoscopic probes with the smallest footprint reported to date. Images taken within the visual cortex and hippocampus at depths larger than 2 mm allow identifying neuronal structures and reveal micrometre-sized details. The technique causes minimal damage to the tissue structures surrounding the fibre penetration volume, as shown by the post-mortem analysis of the brain sections.

All experiments using animal models shown in this chapter were performed by Tristan Altwegg-Boussac, Janelle Pakan, and Nathalie Rochefort at the University of Edinburgh (United Kingdom).

The contributions from the author of this Thesis to the work presented in this chapter consisted of: (i) design of the fluorescence imaging system, (ii) experimental assessment of imaging resolution, and (iii) validation of fluorescence imaging.

The contents of this chapter have been submitted for publication as: S. Turtaev, **I. T. Leite**, T. Altwegg-Boussac, J. M. P. Pakan, N. L. Rochefort, and T. Čižmár, *High-fidelity multimode fibre based endoscopy for deep-brain in vivo imaging*, arXiv:1806.01654 [physics.med-ph].

## 6.1 Methods

A DMD was the chosen modulator when devising this system, not only due to the large modulation rates offered, but also owing to its high performance in terms of beam-shaping fidelity, as demonstrated previously in Fig. 2.4. While high acquisition speeds bring clear practical benefits such as allowing prompt refocussing on objects of interest as well as minimising photobleaching (due to shorter exposure times to the excitation light), a higher power ratio in the excitation foci leads to enhanced image contrast by minimising fluorescence signals generated by the uncontrolled speckle background.

The system design was similar to that of configuration 3b (Fig. 2.1) used in the experiments presented in Chapter 2, making use of a Fourier-domain basis of input modes and an external phase reference. This design now included a dichroic mirror allowing the spectral separation of light emitted towards a fast bucket detector. The optical pathway for interferometric measurement of the TM was designed in a compact manner allowing its easy replacement by a motorised three-axis imaging stage accommodating a head-fixed animal under the imaging fibre in a stereotaxic arrangement.

### 6.1.1 Experimental setup

The system was designed in a modular manner, consisting of a laser, calibration, beam-shaping and sample modules, as depicted in Fig. 6.1. In the laser module, light from a single-frequency laser source emitting at 532 nm (CrystaLaser CL532-075-S) was divided into a signal and a reference beams, which were coupled to single-mode polarisation-maintaining fibres carrying them to the beam-shaping and calibration modules, respectively. The calibration module was used for the precise alignment of the MMF, as well as for measuring the transmission matrix (TM) of the system, being subsequently replaced by the sample module holding an anaesthetized animal.

Lenses L2, L3 and L4 relayed the far-field of the holograms generated at the DMD (ViALUX V7001, $1024 \times 768$ resolution) to the proximal facet of the MMF. An iris diaphragm was used in the Fourier plane of L2 to isolate the first diffraction order of the holograms, while blocking all remaining. The combination of lenses L2 and L3 (200 mm and 75 mm focal lengths, respectively) was chosen to underfill the aperture of aspheric lens L4 (8 mm focal length, 0.50 NA) in order to reduce its effective numerical aperture down to 0.23 to match that from the MMF.

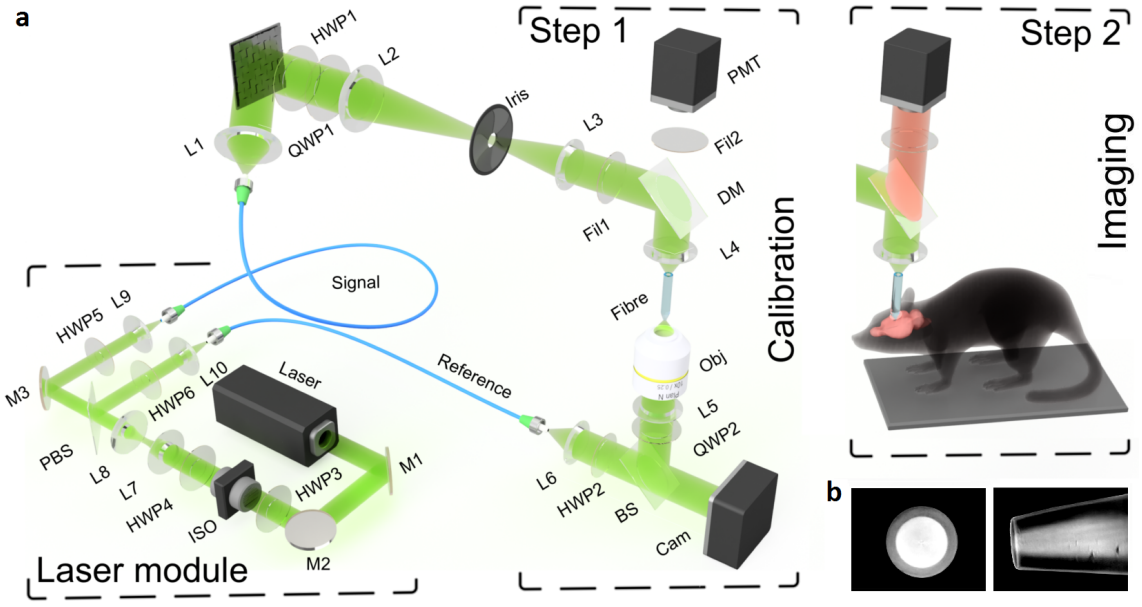


FIGURE 6.1: Multimode fibre-based fluorescence imaging system. **a,** Scheme of the setup. A calibration step precedes imaging. **b,** Flat-top termination of the MMF probe with 50 µm core diameter and 60 µm external diameter.

Dichroic mirror DM together with excitation filter Fil1 and emission filter Fil2 separated and spectrally purified the fluorescence signal collected back by the MMF. Photomultiplier tube PMT (Thorlabs PMT2101/M) measured the overall intensity of the fluorescence signal. Half-wave plate HWP1 and quarter-wave plate QWP1 provided the two degrees of freedom necessary to reach the purest circular polarisation state of the spatially-modulated signal at the input facet of the fibre.

Microscope objective Obj, in combination with tube lens L5 (150 mm focal length) imaged the selected focal plane onto CCD camera Cam (Basler piA640-210gm) with a 27.7× magnification. The reference beam was collimated by aspheric lens L6 (8 mm focal length, 0.50 NA) and combined with the signal beam using non-polarising beamsplitter cube BS. Quarter-wave plate QWP2 converted the polarisation state of the output speckle patterns to linear, and half-wave plate HWP2 aligned the polarisation axis of the reference signal in order to maximise the contrast of the interference patterns at the camera. Microscope objective Obj was mounted on a single-axis translation stage for precise focusing and displacement of the calibration plane with respect to the output fibre facet.

The MMF chosen as the endoscopic probe was a standard, commercially available fibre with 50 µm-diameter core and 0.22 NA (Thorlabs FG050UGA), identical to that used in the experiments described in Chapter 2. In order to minimise the tissue damage caused by compression during the penetration process, the fibre probe (2 cm in length) was post-processed into a flat-cone termination by polishing out the excess of cladding from 125 µm down to 60 µm external diameter, as shown in Fig. 6.1b, using the procedure described previously in Subsection 3.1.1.

### 6.1.2 Holographic methods

A Fourier-domain wavefront shaping approach making use of an external phase reference was employed, as described previously in Subsection 2.4.3. Being uniformly distributed, an external phase reference prevents the formation of "blind" spots in the field of view, which originate from the speckled nature of internal references [27]. The TM was measured interferometrically, as detailed in Subsection 2.4.1, using a basis of ≈3000 input modes. Despite the fibre sustaining ≈1050 waveguide modes for each polarisation state, the input modes were oversampled in order to reach the highest possible fraction of power contained in the foci produced, ≈75% in this case (Fig. 2.4). For each input mode, the interferometric response was sampled in steps of $\pi/2$ over just one phase cycle, i.e. $\delta\phi = \pi/2$ and $n = 4$ in Eq. (2.5).

The calibration plane was typically set to 5–15 µm working distances from the fibre facet, to minimise sample-induced aberrations. Additionally, for the MMF employed such working distances yield a nearly uniform NA matching that of the fibre, over a field of view having the same dimensions as the fibre core (Section 4.2). The basis of output modes consisted of a square grid of $100 \times 100$ points spaced by approximately 0.53 µm across the focal plane, which were conjugate to pixels of the CCD detector during the calibration procedure. This is smaller than the required sampling interval, given by $\lambda/2\mathrm{NA} \simeq 1.2\,\mu\mathrm{m}$, to guarantee that the spatial resolution of the reconstructed images was limited by diffraction, rather than sampling. Only the ≈7000 output modes falling within the ⌀50 µm circular area of the distal field of view were scanned during image acquisition, at the maximum refresh rate of the DMD modulator, yielding ≈3.5 images per second.

Images were reconstructed using the fluorescence signals collected and guided back by the MMF, upon laser-scanning of the samples with a focussed excitation beam. Such diffraction-limited foci were generated by means of binary

amplitude holograms based on the Lee approach [78], as given by Eqs. (2.11) and (2.13).

### 6.1.3 Animal methods

#### Animals

Data were acquired from five adult mice (5-6 months old). In four mice, a subpopulation of inhibitory neurons, Somatostatin-expressing (SST) neurons, was labelled with a red fluorescent marker (tdTomato) using a Cre-driver transgenic mouse line: Sst<tm2.1(cre)Zjh> (SST-Cre) [RRID: IMSR_JAX: 013044] (Jackson Laboratory, ME, USA) cross-bred with Rosa-CAG-LSL-tdTomato [RRID: IMSR_JAX: 007914] mice. In one mouse, another subpopulation of inhibitory neurons, (VIP) neurons, was labelled with the same red fluorescent marker (tdTomato) using a Cre-driver transgenic mouse line: Vip<tm1(cre)Zjh> (VIP-Cre) [RRID: IMSR_JAX: 010908] (Jackson Laboratory, ME, USA) cross-bred with Rosa-CAG-LSL-tdTomato [RRID: IMSR_JAX: 007914] mice. The animals were group housed (typically 2-4 mice), and both male and female mice were used in the experiments. All procedures were approved by the University of Edinburgh animal welfare committee and were performed under a UK Home Office project license.

#### Surgical procedures

For craniotomy, mice were anaesthetised with isoflurane (4% for induction and 1–2% for maintenance during surgery and throughout imaging) and mounted on a stereotaxic frame (David Kopf Instruments, CA, USA). Eye cream was applied to protect the eyes (Bepanthen, Bayer, Germany), analgesics and anti-inflammatory drugs were injected subcutaneously (Vetergesic, buprenorphine, $0.1\,\mathrm{mg\,kg^{-1}}$ of body weight, carprofen, 0.15 mg, and dexamethasone, 2 µg). A section of scalp was removed, and the underlying bone was cleaned before a craniotomy (around $2 \times 2\,\mathrm{mm}^2$) was made over the left primary visual cortex (V1, 2.5 mm lateral and 0.5 mm anterior to lambda). Cyanoacrylate glue (Locktite, UK) was applied to the surrounding skull, muscle, and wound margins to prevent further bleeding.

### 6.1.4 *In-vivo* imaging methods

The *in-vivo* imaging stage was placed below the fibre and consisted of a custom made frame with ear-bars, to keep the animal's head position fixed during the imaging procedure, and a fitted facemask for delivery of isoflurane anaesthesia (1–2%). Suitable body temperature was maintained via thermal bandage. The imaging stage was mounted on a three-axis motorised translation stage with servo-driven actuators (ThorLabs, USA), allowing precise positioning of the animal both laterally for targeting the craniotomy and axially for the control of the fibre penetration process. The endoscopic fibre probe was gradually lowered into the craniotomy, up to 1–4 mm into the brain tissue targeting deep cortical layers in V1 and ventrally through the hippocampus to the base of the brain. Images were collected at ≈3.5 frames per second at multiple regions throughout the tissue.

At the end of the imaging session, the animals were given an overdose of sodium pentobarbital (240 mg $kg^{-1}$) prior to transcardial perfusion with phosphate buffered saline (PBS) and then 4% paraformaldehyde. The fixed brains were then extracted and 50 µm thick coronal sections were made with a vibratome (Leica, Germany) to confirm the location of the fibre tract.

## 6.2 Results

### 6.2.1 Characterisation of the imaging system

Figure 6.2a demonstrates the high uniformity of the generated foci across the field of view, with the intensity of one of them shown in greater detail in logarithmic scale. These foci contained ≈75% of the total output power, and their peak intensities show an enhancement exceeding 3100 with respect to the average background level.

The imaging resolution was assessed using a negative USAF-1951 test target placed in proximity to the distal fibre endface. As shown in Fig. 6.2b, the line separations of 4 µm and 1.9 µm were imaged with contrasts of 85% and 30%, respectively. This is in good agreement with the resolution limit (≈1.5 µm using Rayleigh's criterion) dictated by the NA of the fibre and wavelength used.

Red fluorescent beads (4.0 µm in diameter) fixed on a microscope coverglass were used to validate the fluorescence imaging operation of the system, as shown in Fig. 6.2c. Due to the high sparsity of this sample, there is no noticeable impact from the limited power ratio on the contrast of the reconstructed image. In case of

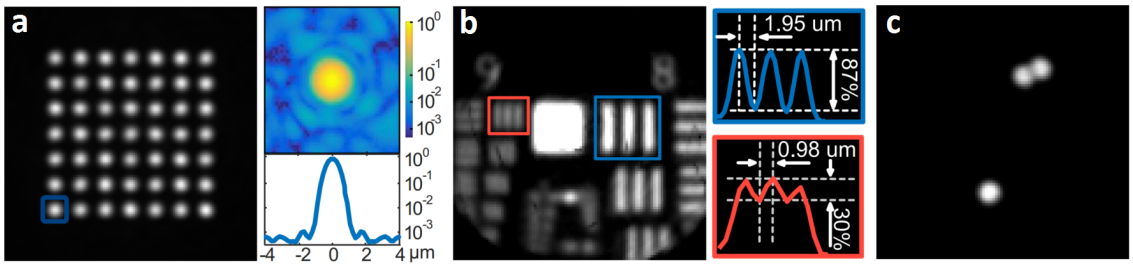


FIGURE 6.2: Characterisation of the fibre-based imaging system. **a,** Uniformity of foci generated across the fibre facet (left) and intensity distribution (top-right) and corresponding azimuthally-averaged profile (bottom-right) of the highlighted focal point, in logarithmic scale. **b,** Assessment of imaging resolution using a negative USAF-1951 test target, imaged in transmission. **c,** Validation of fluorescence imaging using 4 µm red fluorescent beads.

densely-labelled volumetric samples however, the uncontrollable speckle background of the excitation signal translates into lower signal-to-noise ratio and, as such, the power ratio becomes a crucial attribute of the imaging system.

### 6.2.2 *In-vivo* imaging of deep-brain tissues

The demonstration of *in-vivo* imaging capability deep within the brain of an anaesthetised animal was performed in transgenic mice with a subpopulation of inhibitory interneurons labelled with a red fluorescent marker (tdTomato). The insertion of the fibre probe into the primary visual cortex (V1) and deeper into the hippocampus of the mouse brain was made through a small craniotomy. The images shown in Fig. 6.3a,b were acquired at different depths within V1 (0.5 mm to 0.8 mm deep) and in the CA1 region and dendate gyrus of the hippocampus (≈1.5 mm and ≈2 mm deep). The resolution and contrast achieved *in vivo* allowed for the visual identification of both relatively large objects, such as cell soma (10 µm to 20 µm in diameter, Fig. 6.3a), and thin processes (typically 1 µm to 2 µm wide) with fine structures corresponding to synaptic boutons (Fig. 6.3b). Although the *in-vivo* measurements did not require high levels of exposure to excitation light, no adverse effect of photobleaching was observed during image acquisition, even when the output power was set to its maximum value of ≈2 mW (measured at the sample plane). The high acquisition frame rate of the system allowed the live recording of the labelled structures during fibre insertion (see Supplementary Video available at [106]).

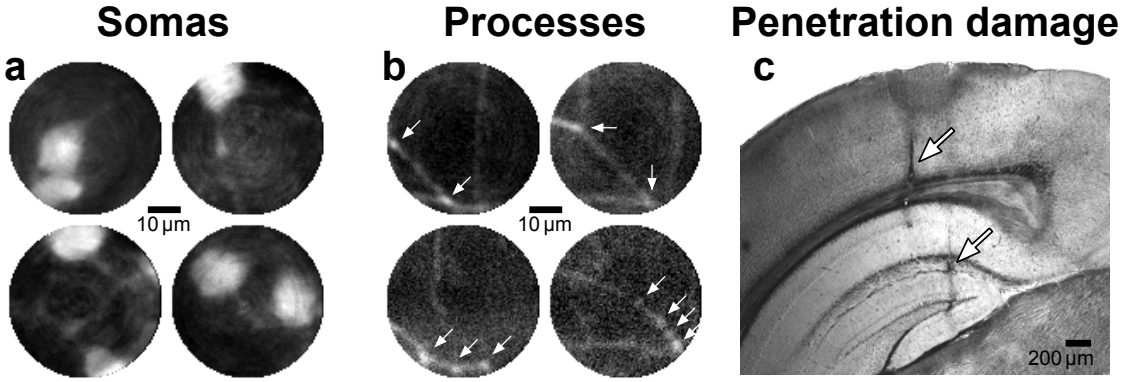


FIGURE 6.3: Deep-brain in-vivo fluorescence imaging through a multimode fibre. **a,b,** Images of somata (**a**) and processes (**b**) if inhibitory neurons observed via direct insertion of the MMF probe up to 2 mm to 3 mm deep into the brain tissue of a mouse animal model. The arrows indicate branching points and synaptic boutons. **c,** Post-mortem coronal brain section showing two fibre tracts caused by the MMF probe in the visual cortex and in the hippocampus. The width of each tract is less than 50 µm.

The impact of the minimally-invasive probe was assessed from a post-mortem section of a perfused brain after MMF-based imaging, shown in Fig. 6.3c. The fibre probe caused minimal damage *in vivo*, with both tracts resulting from the fibre penetration (in the visual cortex and hippocampus) being smaller than 50 µm in width.

## 6.3 Discussion

The MMF-based imaging system presented here allowed fluorescence imaging of deep-brain structures with micrometre-scale spatial resolution via the thinnest endoscopic probes to date, resulting in minimal damage to the tissue surrounding the fibre penetration area.

In anaesthetised transgenic mice with tdTomato fluorescent protein expression in a sparse sub-population of inhibitory interneurons, visually identifiable images of neuronal somas and processes were obtained both in the visual cortex and in the hippocampus, more than 2 mm from the surface of the brain. While in these experiments the imaging depth was limited to the regions of labelled tissue, with this technique the entire dorsal-ventral extent of the mouse brain (4 mm to 6 mm) can be covered, allowing imaging of even the most ventrally located nuclei in the brain.

In contrast with traditional micro-endoscopy systems, the achieved resolution was limited only by the NA of the fibre, being comparable with a standard 10× microscope objective. This is because the active holographic approaches inherently correct all aberrations in the entire optical path, including those caused by components and alignment imperfections.

Imaging immediately after insertion of the endoscopic probe, which is only possible due to its minuscule footprint, eliminates the need for a long postoperative recovery period, as well as the necessity of surgical removal of overlying tissue and implantation of an imaging element, such as a GRIN lens [107, 108]. Moreover, a robust cage construction enabled imaging spanning several hours, with the possibility of fibre re-insertion in different regions without the need for re-calibration.

The acquisition speed of the system was limited by the ≈23 kHz refresh-rate of the DMD modulator, resulting in 7-kilopixel images acquired at 3.5 frames per second. While this proved sufficient to allow adequate temporal resolution for fluorescence imaging in living tissues, observations of dynamic processes usually require acquisition rates greater than 10 Hz. Naturally, higher imaging speed could rely on the further development of faster modulators. For now, faster image acquisition is also possible by reducing the size of the images, either by decreasing spatial sampling or limiting the field of view. Another possibility is to restrict scanning to particular regions of interest within the field of view, for instance using foveated imaging [109].

The holographic methods employed here also allow scanning along multiple (pre-calibrated) focal planes at different working distances from the distal fibre endface, opening a route for volumetric imaging. In this work, the large axial dimension of the excitation foci (resulting from the low NA of fibre probe) did not allow to fully exploit this modality. Moreover, eliminating the out-of-focus light by means of confocal rejection of incoherent fluorescence signals is incompatible with this technology due to the dispersion properties of multimode waveguides. However, custom-made high-NA optical fibres such as that shown in the previous chapters can offer a significant improvement in axial resolution, and therefore provide a route for optical sectioning.

# Chapter 7

# Conclusions

This end chapter concludes the Thesis by summarising the results presented in the previous chapters, and discussing future research directions which could stem from this work.

## 7.1 Summary of the results

This Thesis presents new advancements in the topic of holographic micro-endoscopy using multimode optical fibres (MMFs), a perspective technology for devising minimally-invasive, light-based examinations with great detail deep inside living tissues.

The spatial resolution of such techniques is limited by the numerical aperture (NA) of the fibres, which dictates the maximum spatial frequencies allowed to propagate through. A new type of all-solid MMF was introduced, that due to a remarkably high refractive index contrast between the core and cladding materials, is able to offer an NA exceeding 0.9. A modified system design and new methodologies allowing measuring and compensating the adverse effect of mode-dependent loss present in these fibres were devised, enabling the almost complete exploitation of their full NA. High-resolution diffraction-limited foci were generated across such MMFs with unprecedented output NAs. In addition to improvements in imaging resolution, this has the potential to enable other high-NA techniques delivered by MMF probes.

In particular, such highly-focussed light outputs were shown to provide three-dimensional optical confinement of micrometre-sized dielectric objects by a single beam – optical tweezers. The wavefront shaping techniques employed, being inherently holographic, allowed the flexible control of the number of trap sites and their relocation across all three-dimensions independently. This was

demonstrated by the dynamic manipulation of complex 3D arrangements of microspheres using such holographic optical tweezers (HOT). The potential for applications in complex environments, such as studies *in vivo*, was further shown by HOT-manipulation inside a turbid cavity through a minuscule channel.

Quantitative analyses of the stiffnesses of the fibre-based HOT revealed that their performance does not lag significantly behind that of standard geometries relying on bulk objectives. Additionally, a methodology was developed allowing the fine relocation of trapped objects independently and in all three-dimensions with nanometre-scale precision. This is critically important for perspective applications *in vivo*, since alternative means of mutually positioning the optical traps with respect to the sample (e.g. with piezo-actuated stages, as commonly used *in vitro*) will no longer be feasible. Both results suggest that the performance of the fibre-HOT is indeed sufficient for applications in biomedical research.

Separately, a study was undertaken to assess the comparative performance in terms of beam-shaping fidelity in the typical regimes of complex photonics, for the two most commonly employed technologies for spatial modulation of light: nematic liquid-crystal spatial light modulators (LC-SLMs) and digital micromirror devices (DMDs). It was shown that, when employed in off-axis geometries and despite their limited modulation depth, DMDs outperform LC-SLMs not only in modulation rates but also in beam-shaping fidelity. This is especially significant when controlling light propagation through MMFs, as in such cases a significant portion of uncontrolled light arising from scattering in LC-SLMs leads to higher noise levels which corrupt the wavefront shaping procedures.

Finally, a highly-optimised fluorescence imaging system for MMF-based micro-endoscopy was demonstrated employing a DMD modulator. This system was used for deep-brain imaging *in vivo* in mice animal models, with minimal damage to the tissue. Images with 7-kilopixel resolution were acquired at 3.5 frames per second acquisition rates within the visual cortex and hippocampus brain regions, at depths exceeding 2 mm. These allowed the visual identification of neuronal structures such as somas and processes with resolvable details at the micrometre scale.

The results demonstrated in this Thesis pave the way to the implementation of numerous advanced techniques of biophotonics, particularly those relying on high-NA focussing, deep within the most sensitive tissues of living organisms through minimally-invasive, single-fibre probes.

## 7.2 Future work

Fibre-based HOT have the potential of bringing studies of biophotonics relying on optical tweezers to direct measurements *in vivo*. However, a few aspects remain to be solved. In this work, external imaging of trapped particles allowed tracking their 3D trajectories to calibrate the HOT. This approach is naturally incompatible with the deployment of fibre-HOT inside complex media, where no direct optical access to the trapped objects will be possible. The employment of fibre-HOT as, for instance, force transducers, will thus require an alternative means of particle tracking. While an imaging modality at a separate wavelength could be combined simultaneously with the HOT using the same fibre, particle tracking using images acquired in this way would either lack in spatial or temporal sampling, even with the faster modulators available today. The solution could rely on exploiting the light signals which are back-scattered by the particles, collected and guided back through the fibre towards the proximal side where they could be analysed, e.g. by means of a correlation filter.

High-resolution focussing through MMFs is broadly relevant beyond the applications of HOT, unlocking many new possibilities for modern biomedical research where current approaches frequently rely on tight focussing of laser light. This work also opens a route to the implementation of highly advanced imaging techniques and microscopy requiring high NA deep inside living tissues through minimally-invasive MMF probes.

The possibility of realising minimally-invasive observations within the deeper layers of tissues *in vivo* has been the main driver of the topic of holographic micro-endoscopy exploiting MMFs. The high-fidelity fibre-based fluorescence imaging system demonstrated constitutes one the first materialisations of such potential. This combined reliable wavefront shaping methods which had been previously shown with a careful optical design, allowing diffraction-limited resolution by the NA of the fibre, quality of foci approaching the theoretical limits, and the highest modulation rates currently available. Still, the latter poses a constraint between image acquisition rate, spatial resolution, and accessible field-of-view, which need to be compromised against each other. Thus, image acquisition through the MMF can be increased by reducing the spatial sampling (e.g. one could halve it during the experiments without the need for re-measuring the TM by scanning over every other two pre-calibrated distal foci), by limiting the field of view to smaller regions of interest, by a combination of both [109], or even by employing the concept of compressive sensing [110]. The system can also be

extended to multicolour imaging, by combining two or more excitation wavelengths and acquiring for each one a separate TM [111].

Future developments in the field will certainly build on the further progress in the technology of spatial light modulators. Faster modulation rates can allow accessing observation of dynamic processes at smaller time scales. On the other hand, the further development of already existing (but still low-resolution) MEMS modulators having "piston-like" individual elements [112, 113], could provide direct phase modulation with high modulation depths together with the large switching rates typically offered by MEMS systems, thus combining the advantages of both DMDs and LC-SLMs.

Further progress might also encompass the development of new holographic approaches capable of self-alignment to counteract drift of the optomechanical components responsible for the degradation of acquired TMs over time or, alternatively, devising wavefront shaping approaches capable of re-calibration using reflected light rather than in transmission, which would not require removal and re-implantation of the MMF probe. Advances will certainly rely also on the development of novel fibre types directly optimised for the purposes of holographic endoscopy. For instance, it has been recently shown that graded-index fibres having sufficiently high quality could be virtually immune to bending [114], which could open the way to *in-vivo* studies in freely-behaving animal models.

# Appendix A

# Waveguide modes of a step-index optical fibre

Here, the analytical expressions of the exact vector eingenmodes of an ideal step-index fibre are derived, as well as their characteristic equation [37, 115].

## A.1 The electromagnetic wave equation

Let us start by considering a linear, homogeneous and isotropic medium, characterised by the material constants $\epsilon$ and $\mu$, the electric permittivity and magnetic permeability. In the absence of sources of electromagnetic field (i.e. free charge and current), Maxwell's equations take the form:

$$\nabla \cdot \mathbb{E}(\mathbf{r}, t) = 0 \tag{A.1}$$

$$\nabla \cdot \mathbb{H}(\mathbf{r}, t) = 0 \tag{A.2}$$

$$\nabla \times \mathbb{E}(\mathbf{r}, t) = -\mu \frac{\partial}{\partial t} \mathbb{H}(\mathbf{r}, t) \tag{A.3}$$

$$\nabla \times \mathbb{H}(\mathbf{r}, t) = \epsilon \frac{\partial}{\partial t} \mathbb{E}(\mathbf{r}, t) \tag{A.4}$$

where $\mathbb{E}$ and $\mathbb{H}$ are the electric and magnetic vectors of the electromagnetic field, both dependent on position $\mathbf{r}$ and time $t$. Taking the curl of Eqs. (A.3) and (A.4) and using the vector identity:

$$\nabla \times (\nabla \times \mathbf{v}) = \nabla (\nabla \cdot \mathbf{v}) - \nabla^2 \mathbf{v}, \tag{A.5}$$

where $\nabla^2\mathbf{v} = \nabla\cdot(\nabla\mathbf{v})$:

$$\nabla(\nabla\cdot\mathbb{E}) - \nabla^2\mathbb{E} = -\mu\frac{\partial}{\partial t}(\nabla\times\mathbb{H}) \tag{A.6}$$

$$\nabla(\nabla\cdot\mathbb{H}) - \nabla^2\mathbb{H} = \epsilon\frac{\partial}{\partial t}(\nabla\times\mathbb{E}) \tag{A.7}$$

Noting that the first term on the left-hand side vanishes due to Eqs. (A.1) and (A.2), and by replacing the curls on the right-hand side with Eqs. (A.3) and (A.4), one obtains:

$$-\nabla^2\mathbb{E} = -\mu\frac{\partial}{\partial t}\left(\epsilon\frac{\partial\mathbb{E}}{\partial t}\right) \tag{A.8}$$

$$-\nabla^2\mathbb{H} = \epsilon\frac{\partial}{\partial t}\left(-\mu\frac{\partial}{\partial t}\mathbb{H}\right) \tag{A.9}$$

The two equations are identical, and can be re-arranged into:

$$\nabla^2\mathbb{F} - \epsilon\mu\frac{\partial^2}{\partial t^2}\mathbb{F} = 0, \tag{A.10}$$

where $\mathbb{F}$ represents either $\mathbb{E}$ or $\mathbb{H}$. Equation (A.10) is the *electromagnetic wave equation* for linear, homogeneous and isotropic media, in the absence of sources of field. The phase velocity is given by $1/\epsilon\mu = c/n$, where $c$ is the speed of light in vacuum and $n$ the refractive index of the medium.

## A.2 Solving the wave equation in cylindrical waveguides

Here, we consider a step-index optical fibre modelled as an infinitely long dielectric cylinder with radius $a$ and refractive index $n_1$ (the *core*), surrounded by a different dielectric medium of lower refractive index $n_2$ (the *cladding*) extending radially to infinity, i.e. a spatial distribution of refractive index:

$$n(\mathbf{r}) = \begin{cases} n_1 & , r < a \\ n_2 & , r \geq a \end{cases} \tag{A.11}$$

with $n_1 > n_2$.

We will search for field solutions of the wave equation Eq. (A.10), $\mathbb{E}(\mathbf{r}, t)$ and $\mathbb{H}(\mathbf{r}, t)$, with the form:

$$\mathbb{F}(\mathbf{r},t) = \mathbf{F}(r,\theta)\, e^{i(\omega t-\beta z)} \tag{A.12}$$

using a polar coordinate system suitable to the geometry of the problem, where $\mathbb{F}$ represents either $\mathbb{E}$ or $\mathbb{H}$, $\omega$ the (angular) frequency, $\beta$ the propagation constant, and $i$ the imaginary unit. Note that, in Eq. (A.12), $\mathbf{F}(r,\theta)$ denotes a complex amplitude which does not depend on the axial coordinate $z$, and that only the real part of $\mathbb{F}$ bears physical meaning. Such solutions for the field are invariant in the direction of propagation $z$, and are thus designated *propagagation-invariant modes* or *eigenmodes*.

The curl operator is expressed in cylindrical coordinates as:

$$\nabla\times\mathbf{v} = \left(\frac{1}{r}\frac{\partial v_z}{\partial\theta} - \frac{\partial v_\theta}{\partial z}\right)\hat{r} + \left(\frac{\partial v_r}{\partial z} - \frac{\partial v_z}{\partial r}\right)\hat{\theta} + \frac{1}{r}\left(\frac{\partial}{\partial r}(rv_\theta) - \frac{\partial v_r}{\partial\theta}\right)\hat{z}, \tag{A.13}$$

where $\mathbf{v} = v_r\hat{r} + v_\theta\hat{\theta} + v_z\hat{z}$, whereas the Laplacian operator in this coordinate system is expressed as:

$$\nabla^2 = \frac{\partial^2}{\partial r^2} + \frac{1}{r}\frac{\partial}{\partial r} + \frac{1}{r^2}\frac{\partial^2}{\partial\theta^2} + \frac{\partial^2}{\partial z^2} \tag{A.14}$$

For a vector field with the form (A.12) then:

$$\nabla\times\mathbb{F} = \left\{\left(\frac{1}{r}\frac{\partial F_z}{\partial\theta} + i\beta F_\theta\right)\hat{r} - \left(\frac{\partial F_z}{\partial r} + i\beta F_r\right)\hat{\theta} + \frac{1}{r}\left(F_\theta + r\frac{\partial F_\theta}{\partial r} - \frac{\partial F_r}{\partial\theta}\right)\hat{z}\right\} e^{i(\omega t-\beta z)} \tag{A.15}$$

where $\mathbf{F} = F_r\hat{r} + F_\theta\hat{\theta} + F_z\hat{z}$, and:

$$\frac{\partial\mathbb{F}}{\partial t} = i\omega\mathbf{F}e^{i(\omega t-\beta z)} \tag{A.16}$$

By replacing Eqs. (A.15) and (A.16) into Maxwell's equations (A.3) and (A.4),

a few algebraic manipulations on the resulting four scalar equations for the transverse components ($\hat{r}$ and $\hat{\theta}$), lead to:

$$E_r(r,\theta) = -\frac{i}{\omega^2\epsilon\mu-\beta^2}\left(\beta\frac{\partial E_z}{\partial r}+\frac{\omega\mu}{r}\frac{\partial H_z}{\partial\theta}\right) \tag{A.17}$$

$$E_\theta(r,\theta) = -\frac{i}{\omega^2\epsilon\mu-\beta^2}\left(\frac{\beta}{r}\frac{\partial E_z}{\partial\theta}-\omega\mu\frac{\partial H_z}{\partial r}\right) \tag{A.18}$$

$$H_r(r,\theta) = -\frac{i}{\omega^2\epsilon\mu-\beta^2}\left(-\frac{\omega\epsilon}{r}\frac{\partial E_z}{\partial\theta}+\beta\frac{\partial H_z}{\partial r}\right) \tag{A.19}$$

$$H_\theta(r,\theta) = -\frac{i}{\omega^2\epsilon\mu-\beta^2}\left(\omega\epsilon\frac{\partial E_z}{\partial r}+\frac{\beta}{r}\frac{\partial H_z}{\partial\theta}\right) \tag{A.20}$$

This means that the transverse components $E_r$, $E_\theta$, $H_r$ and $H_\theta$ of the electromagnetic field are determined by the longitudinal components $E_z$ and $H_z$. To find these, we replace Eq. (A.12) into the wave equation (A.10), to obtain for the longitudinal field components the well-known Helmholtz equation:

$$\left[\nabla_t^2+\left(k^2-\beta^2\right)\right]F_z(r,\theta)=0 \tag{A.21}$$

where $\nabla_t^2 = \nabla^2 - {}^{\partial^2}/_{\partial z^2}$, and $k$ is the magnitude of the wavevector $\mathbf{k}$ (or wavenumber), given by $k^2=\omega^2\epsilon\mu=(k_0 n)^2$, where $k_0$ is the wavenumber in free space.

To solve Eq. (A.21), we shall look for solutions with separable variables with the form:

$$F_z(r,\theta)=\psi(r)\,e^{il\theta}, \tag{A.22}$$

which, replaced into Helmoltz equation (A.21) yield:

$$\frac{\partial^2\psi}{\partial r^2}+\frac{1}{r}\frac{\partial\psi}{\partial r}+\left[\left(k^2-\beta^2\right)-\frac{l^2}{r^2}\right]\psi=0 \tag{A.23}$$

which is *Bessel's differential equation* of order $l$. Note that solutions (A.22) must satisfy the boundary condition $F_z(r,\theta)=F_z(r,\theta+2\pi)$, which means that $l$ is an integer (positive, negative or zero), and that Bessel's equation (A.23) has integer order.

In the core region ($r<a$), $k^2=k_0^2n_1^2$ ($n_1$ is the refractive index of the core, and $k_0={}^{\omega}/_{c}={}^{2\pi}/_{\lambda}$ the wavenumber in free space) and $k^2-\beta^2>0$. Defining for

convenience $u' = \sqrt{k_0^2 n_1^2 - \beta^2} > 0$, then Eq. (A.23) takes the usual form:

$$r^2 \frac{\partial^2 \psi}{\partial r^2} + r \frac{\partial \psi}{\partial r} + \left[ \left( u' r \right)^2 - l^2 \right] \psi = 0 \tag{A.24}$$

and, since it has integer order, it has the general solution:

$$\psi(r) = A_1 J_l \left( u' r \right) + A_2 Y_l \left( u' r \right) \tag{A.25}$$

where $J_l$ and $Y_l$ are the Bessel functions of the first and second kind, respectively, and $A_1$ and $A_2$ are complex coefficients.

In the cladding region ($r \geq a$), we have $k^2 = k_0^2 n_2^2$ ($n_2$ is the refractive index of the cladding) and $k^2 - \beta^2 < 0$. This means that the argument of Eq. (A.23) is purely imaginary. If we define $w' = \sqrt{\beta^2 - k_0^2 n_2^2} > 0$, we can re-write Eq. (A.23) in terms of a real argument:

$$r^2 \frac{\partial^2 \psi}{\partial r^2} + r \frac{\partial \psi}{\partial r} - \left[ \left( w' r \right)^2 + l^2 \right] \psi = 0 \tag{A.26}$$

which is known as *modified Bessel's differential equation* of (integer) order $l$, which has the general solution:

$$\psi(r) = B_1 I_l \left( w' r \right) + B_2 K_l \left( w' r \right) \tag{A.27}$$

where $I_l$ and $K_l$ are the modified Bessel functions of the first and second kind, respectively, and $B_1$ and $B_2$ are complex coefficients.

The solution $\psi(r)$:

$$\psi(r) = \begin{cases} A_1 J_l \left( u' r \right) + A_2 Y_l \left( u' r \right) & , r < a \\ B_1 I_l \left( w' r \right) + B_2 K_l \left( w' r \right) & , r \geq a \end{cases} \tag{A.28}$$

Physical solutions for the guided modes must be finite in the core and decay exponentially in the cladding. Considering the assimptotic behaviour of the Bessel functions $J_l$, $Y_l$, $I_l$, and $K_l$:

$$x \ll 1 : \begin{cases} J_l(x) \to \frac{1}{l!} \left( \frac{x}{2} \right)^l \\ Y_{l=0}(x) \to \frac{2}{\pi} \left( \log \frac{x}{2} + 0.5772 \ldots \right) \\ Y_{l \neq 0}(x) \to -\frac{(l-1)!}{\pi} \left( \frac{2}{x} \right)^l \end{cases} \tag{A.29}$$

$$x \gg 1 : \begin{cases} I_l(x) \to \sqrt{\frac{1}{2\pi x}} e^x \\ K_l(x) \to \sqrt{\frac{\pi}{2x}} e^{-x} \end{cases} \tag{A.30}$$

one concludes that the longitudinal field components must have $A_2 = B_1 = 0$. Thus:

$$\psi(r) = \begin{cases} AJ_l(u'r) & , r < a \\ BK_l(w'r) & , r \geq a \end{cases} \tag{A.31}$$

Introducing $u = au' = a\sqrt{k_0^2 n_1^2 - \beta^2}$ and $w = aw' = a\sqrt{\beta^2 - k_0^2 n_2^2}$, then:

$$u^2 + w^2 = a^2 k_0^2 \left(n_1^2 - n_2^2\right) \tag{A.32}$$

which defines a new parameter, known as *normalised frequency* (or $v$-number):

$$v = ak_0\sqrt{n_1^2 - n_2^2} = ak_0 \mathrm{NA} \tag{A.33}$$

where NA is the numerical aperture of the waveguide, and the previous relation can be written as:

$$u^2 + w^2 = v^2 \tag{A.34}$$

Thus, the solution (A.22) for the axial components becomes:

$$E_z(r,\theta) = \begin{cases} AJ_l(ur/a)\, e^{il\theta} & , r < a \\ BK_l(wr/a)\, e^{il\theta} & , r \geq a \end{cases} \tag{A.35}$$

$$H_z(r,\theta) = \begin{cases} CJ_l(ur/a)\, e^{il\theta} & , r < a \\ DK_l(wr/a)\, e^{il\theta} & , r \geq a \end{cases} \tag{A.36}$$

The remaining components can now be computed using Eqs. (A.17)–(A.20):

$$E_r(r,\theta) = \begin{cases} \left(\frac{a}{u}\right)^2 \left[-iA\beta\frac{u}{a}J_l'(ur/a) + Cl\frac{\omega\mu}{r}J_l(ur/a)\right] e^{il\theta} & , r < a \\ \left(\frac{a}{w}\right)^2 \left[iB\beta\frac{w}{a}K_l'(wr/a) - Dl\frac{\omega\mu}{r}K_l(wr/a)\right] e^{il\theta} & , r \geq a \end{cases} \tag{A.37}$$

$$E_\theta(r,\theta) = \begin{cases} \left(\frac{a}{u}\right)^2 \left[iC\omega\mu\frac{u}{a}J_l'(ur/a) + Al\frac{\beta}{r}J_l(ur/a)\right] e^{il\theta} & , r < a \\ \left(\frac{a}{w}\right)^2 \left[-iD\omega\mu\frac{w}{a}K_l'(wr/a) - Bl\frac{\beta}{r}K_l(wr/a)\right] e^{il\theta} & , r \geq a \end{cases} \tag{A.38}$$

$$H_r(r,\theta) = \begin{cases} \left(\frac{a}{u}\right)^2 \left[-iC\beta\frac{u}{a}J_l'(ur/a) - Al\frac{\omega\epsilon_1}{r}J_l(ur/a)\right] e^{il\theta} & , r < a \\ \left(\frac{a}{w}\right)^2 \left[iD\beta\frac{w}{a}K_l'(wr/a) + Bl\frac{\omega\epsilon_2}{r}K_l(wr/a)\right] e^{il\theta} & , r \geq a \end{cases} \tag{A.39}$$

$$H_\theta(r,\theta) = \begin{cases} \left(\frac{a}{u}\right)^2 \left[-iA\omega\epsilon_1 \frac{u}{a} J_l'\left(ur/a\right) + Cl\frac{\beta}{r} J_l\left(ur/a\right)\right] e^{il\theta} & , r < a \\ \left(\frac{a}{w}\right)^2 \left[iB\omega\epsilon_2 \frac{w}{a} K_l'\left(wr/a\right) - Dl\frac{\beta}{r} K_l\left(wr/a\right)\right] e^{il\theta} & , r \geq a \end{cases} \tag{A.40}$$

where $J_l'$ and $K_l'$ denote the derivatives of $J_l$ and $K_l$ with respect to their arguments.

These solutions must satisfy the boundary condition at the interface $r = a$ between the core and cladding which requires that the tangential components ($E_z$, $E_\theta$, $H_z$, and $H_\theta$) are continuous. This leads to the following set of equations:

$$AJ_l(u) = BK_l(w) \tag{A.41}$$

$$CJ_l(u) = DK_l(w) \tag{A.42}$$

$$i\omega\mu\frac{J_l'(u)}{u}C + l\beta\frac{J_l(u)}{u^2}A = -i\omega\mu\frac{K_l'(w)}{w}D - l\beta\frac{K_l(w)}{w^2}B \tag{A.43}$$

$$-i\omega\epsilon_1\frac{J_l'(u)}{u}A + l\beta\frac{J_l(u)}{u^2}C = i\omega\epsilon_2\frac{K_l'(w)}{w}B - l\beta\frac{K_l(w)}{w^2}D \tag{A.44}$$

which form a set of four homogeneous linear equations for the unknown coefficients $A$, $B$, $C$, and $D$:

$$\begin{bmatrix} J_l(u) & -K_l(w) & 0 & 0 \\ 0 & 0 & J_l(u) & -K_l(w) \\ l\beta\frac{J_l(u)}{u^2} & l\beta\frac{K_l(w)}{w^2} & i\omega\mu\frac{J_l'(u)}{u} & i\omega\mu\frac{K_l'(w)}{w} \\ -i\omega\epsilon_1\frac{J_l'(u)}{u} & -i\omega\epsilon_2\frac{K_l'(w)}{w} & l\beta\frac{J_l(u)}{u^2} & l\beta\frac{K_l(w)}{w^2} \end{bmatrix} \begin{bmatrix} A \\ B \\ C \\ D \end{bmatrix} = 0 \tag{A.45}$$

In order to obtain a non-trivial solution from (A.45), the determinant of the simultaneous equations must be set to zero. This leads to the *characteristic equation*, or *dispersion relation*:

$$\left[\frac{J_l'(u)}{uJ_l(u)} + \frac{K_l'(w)}{wK_l(w)}\right]\left[n_1^2\frac{J_l'(u)}{uJ_l(u)} + n_2^2\frac{K_l'(w)}{wK_l(w)}\right] = l^2\left(\frac{\beta}{k_0}\right)^2\left[\frac{1}{u^2} + \frac{1}{w^2}\right]^2 \tag{A.46}$$

whose solutions are the allowed modes with propagation constant $\beta(\omega)$. For a given wavelength (or equivalently, $\omega$) for each $l$ (the azimuthal order of the mode) there is, in general, a finite number of solutions, each of which labelled $m$, the radial order of the mode.

The dimensionless quantity $\beta/k_0$ is designated *effective refractive index*, $n_{\text{eff}}$. Since for guided modes $n_2 k_0 \leq \beta \leq n_1 k_0$, then this condition can be written simply as $n_2 \leq n_{\text{eff}} \leq n_1$.

Notice the implicit dependence in the dispersion relation on $\omega$ (or $\lambda$) through $k_0$, and on both $\beta$ and $\omega$ through the parameters $u$ and $w$:

$$u = a\sqrt{k_0^2 n_1^2 - \beta^2} = ak_0\sqrt{n_1^2 - n_{\text{eff}}^2} \tag{A.47}$$

$$w = a\sqrt{\beta^2 - k_0^2 n_2^2} = ak_0\sqrt{n_{\text{eff}}^2 - n_2^2} \tag{A.48}$$

Solutions satisfying the characteristic equation (A.46) make the homogeneous linear system (A.45) undetermined – otherwise one is left with the trivial solution $A = B = C = D = 0$. This means that one of these coefficients (say, $A$) is a free parameter – connected with the power carried by that particular mode – and all others can be expressed in terms of it. From Eqs. (A.41)–(A.44):

$$\frac{B}{A} = \frac{D}{C} = \frac{J_l(u)}{K_l(w)} \tag{A.49}$$

$$\frac{C}{A} = i\frac{\beta}{\omega\mu}s \tag{A.50}$$

$$\frac{D}{A} = \frac{D}{C}\frac{C}{A} = i\frac{J_l(u)}{K_l(w)}\frac{\beta}{\omega\mu}s \tag{A.51}$$

with $s$ defined as:

$$s = l\left[\frac{1}{u^2} + \frac{1}{w^2}\right]\left[\frac{J_l'(u)}{uJ_l(u)} + \frac{K_l'(w)}{wK_l(w)}\right]^{-1} \tag{A.52}$$

Replacing these in Eqs. (A.35)–(A.40) and using the following recurrence formulas for the Bessel functions:

$$J_l'(x) = \frac{1}{2}\left[J_{l-1}(x) - J_{l+1}(x)\right] \tag{A.53}$$

$$lJ_l(x) = \frac{x}{2}\left[J_{l-1}(x) + J_{l+1}(x)\right] \tag{A.54}$$

$$K_l'(x) = -\frac{1}{2}\left[K_{l-1}(x) + K_{l+1}(x)\right] \tag{A.55}$$

$$lK_l(x) = -\frac{x}{2}\left[K_{l-1}(x) - K_{l+1}(x)\right] \tag{A.56}$$

the field components can be re-written as:

$$E_z(r,\theta) = \begin{cases} A\frac{J_l(u/ra)}{J_l(u)}e^{il\theta} & ,r < a \\ A\frac{K_l(w/ra)}{K_l(w)}e^{il\theta} & ,r \geq a \end{cases} \tag{A.57}$$

$$E_r(r,\theta) = \begin{cases} -iA\frac{\beta a}{uJ_l(u)}\left[\frac{1-s}{2}J_{l-1}(ur/a) - \frac{1+s}{2}J_{l+1}(ur/a)\right]e^{il\theta} & ,r < a \\ -iA\frac{\beta a}{wK_l(w)}\left[\frac{1-s}{2}K_{l-1}(wr/a) + \frac{1+s}{2}K_{l+1}(wr/a)\right]e^{il\theta} & ,r \geq a \end{cases} \tag{A.58}$$

$$E_\theta(r,\theta) = \begin{cases} A\frac{\beta a}{uJ_l(u)}\left[\frac{1-s}{2}J_{l-1}(ur/a) + \frac{1+s}{2}J_{l+1}(ur/a)\right]e^{il\theta} & ,r < a \\ A\frac{\beta a}{wK_l(w)}\left[\frac{1-s}{2}K_{l-1}(wr/a) - \frac{1+s}{2}K_{l+1}(wr/a)\right]e^{il\theta} & ,r \geq a \end{cases} \tag{A.59}$$

$$H_z(r,\theta) = \begin{cases} iA\frac{\beta}{\omega\mu}s\frac{J_l(u/ra)}{J_l(u)}e^{il\theta} & ,r < a \\ iA\frac{\beta}{\omega\mu}s\frac{K_l(w/ra)}{K_l(w)}e^{il\theta} & ,r \geq a \end{cases} \tag{A.60}$$

$$H_r(r,\theta) = \begin{cases} -A\frac{\omega\epsilon_1 a}{uJ_l(u)}\left[\frac{1-s_1}{2}J_{l-1}(ur/a) + \frac{1+s_1}{2}J_{l+1}(ur/a)\right]e^{il\theta} & ,r < a \\ -A\frac{\omega\epsilon_2 a}{wK_l(w)}\left[\frac{1-s_2}{2}K_{l-1}(wr/a) - \frac{1+s_2}{2}K_{l+1}(wr/a)\right]e^{il\theta} & ,r \geq a \end{cases} \tag{A.61}$$

$$H_\theta(r,\theta) = \begin{cases} -iA\frac{\omega\epsilon_1 a}{uJ_l(u)}\left[\frac{1-s_1}{2}J_{l-1}(ur/a) - \frac{1+s_1}{2}J_{l+1}(ur/a)\right]e^{il\theta} & ,r < a \\ -iA\frac{\omega\epsilon_2 a}{wK_l(w)}\left[\frac{1-s_2}{2}K_{l-1}(wr/a) + \frac{1+s_2}{2}K_{l+1}(wr/a)\right]e^{il\theta} & ,r \geq a \end{cases} \tag{A.62}$$

where $s_1$ and $s_2$ are defined as:

$$s_{1,2} = \left(\frac{\beta}{n_{1,2}k_0}\right)^2 s = \left(\frac{n_{\text{eff}}}{n_{1,2}}\right)^2 s \tag{A.63}$$

For non-zero azimuthal order (i.e. $l \neq 0$), these modes have all six field components, and are known as *hybrid modes* (HE and EH). We can also observe that the modes are two-fold degenerate, since $\pm l$ yield the same $m$ solutions of the dispersion equation, and correspond to fields with helical wavefronts of opposite handedness.

### A.2.1 Transverse electric and transverse magnetic modes

We will now look at those modes with azimuthal order zero, which do not carry orbital angular momentum, and are thus azimuthally invariant. By setting $l = 0$, the characteristic equation (A.46) becomes:

$$\left[\frac{J_1(u)}{uJ_0(u)} + \frac{K_1(w)}{wK_0(w)}\right]\left[n_1^2\frac{J_1(u)}{uJ_0(u)} + n_2^2\frac{K_1(w)}{wK_0(w)}\right] = 0 \tag{A.64}$$

where we have made use of the recurrence relations $J_0' = -J_1$ and $K_0' = -K_1$. To satisfy the equality in Eq. (A.64), either one of the two factor must be zero – but

not simultaneously, as it corresponds the trivial solution where all fields are zero.

$$\frac{J_1(u)}{uJ_0(u)} = -\frac{K_1(w)}{wK_0(w)} \tag{A.65}$$

or:

$$\frac{J_1(u)}{uJ_0(u)} = -\left(\frac{n_2}{n_1}\right)^2 \frac{K_1(w)}{wK_0(w)} \tag{A.66}$$

**TM modes**

Let us start by examining the latter case, i.e. the family of modes satisfying characteristic equation (A.66). Since they must not satisfy (A.65), then the parameter $s$ defined by Eq. (A.52) is zero, the same holding for $s_1$ and $s_2$ given by Eq. (A.63). Setting $l$, $s$, $s_1$, and $s_2$ to zero in Eqs. (A.57)–(A.62) yields $E_\theta = H_z = H_r = 0$, and the non-zero field components become:

$$E_z(r,\theta) = \begin{cases} A\frac{J_0(u/ra)}{J_0(u)} & ,r < a \\ A\frac{K_0(w/ra)}{K_0(w)} & ,r \geq a \end{cases} \tag{A.67}$$

$$E_r(r,\theta) = \begin{cases} iA\beta\frac{a}{u}\frac{J_1(ur/a)}{J_0(u)} & ,r < a \\ -iA\beta\frac{a}{w}\frac{K_1(wr/a)}{K_0(w)} & ,r \geq a \end{cases} \tag{A.68}$$

$$H_\theta(r,\theta) = \begin{cases} iA\omega\epsilon_1\frac{a}{u}\frac{J_1(ur/a)}{J_0(u)} & ,r < a \\ -iA\omega\epsilon_2\frac{a}{w}\frac{K_1(wr/a)}{K_0(w)} & ,r \geq a \end{cases} \tag{A.69}$$

These modes are designated *transverse magnetic* (and labelled $\mathrm{TM}_{0m}$, where $m$ is the radial order of the mode) due to the fact that the magnetic vector $\mathbb{H}$ is orthogonal to the direction of propagation, i.e. $H_z = 0$.

**TE modes**

For the family of modes satisfying characteristic equation (A.65), we can find that the parameter $s$ becomes undetermined. This is because we have assumed in Eqs. (A.49)–(A.51) that the coefficient $A$ was different from zero. Also, if $A = 0$ then it follows from the continuity of the tangential components of the field, Eq. (A.41), that $B = 0$. By setting $A$, $B$, and $l$ to zero in Eqs. (A.35)–(A.40), we

obtain $E_r = E_z = H_\theta = 0$, and the non-zero field components:

$$E_\theta(r,\theta) = \begin{cases} -iC\omega\mu\frac{a}{u}\frac{J_1(ur/a)}{J_0(u)} & , r < a \\ iC\omega\mu\frac{a}{w}\frac{K_1(wr/a)}{K_0(w)} & , r \geq a \end{cases} \tag{A.70}$$

$$H_z(r,\theta) = \begin{cases} C\frac{J_0(ur/a)}{J_0(u)} & , r < a \\ C\frac{K_0(wr/a)}{K_0(w)} & , r \geq a \end{cases} \tag{A.71}$$

$$H_r(r,\theta) = \begin{cases} iC\beta\frac{a}{u}\frac{J_1(ur/a)}{J_0(u)} & , r < a \\ -iC\beta\frac{a}{w}\frac{K_1(wr/a)}{K_0(w)} & , r \geq a \end{cases} \tag{A.72}$$

Analogously to the previous case, this family of modes is designated *transverse electric* (and identified by $TE_{0m}$) owing to the fact that the $\mathbb{E}$ is perpendicular to the direction of propagation ($E_z = 0$).

# Bibliography


1. Balas, C. Review of biomedical optical imaging - A powerful, non-invasive, non-ionizing technology for improving in vivo diagnosis. *Meas. Sci. Technol.* **20,** 104020 (2009).
2. Gigan, S. Optical microscopy aims deep. *Nat. Photonics* **11,** 14–16 (2017).
3. Ntziachristos, V. Going deeper than microscopy : The optical imaging frontier in biology. *Nat. Methods* **7,** 603–614 (2010).
4. Čižmár, T. Exploiting multimode waveguides for in vivo imaging. *SPIE Newsroom*, 1–3 (2015).
5. Denk, W, Strickler, J. & Webb, W. Two-photon laser scanning fluorescence microscopy. *Science* **248,** 73–76 (1990).
6. Helmchen, F. & Denk, W. Deep tissue two-photon microscopy. *Nat. Methods* **2,** 932–940 (2005).
7. Maiti, S, Shear, J. B., Williams, R. M., Zipfel, W. R. & Webb, W. W. Measuring serotonin distribution in live cells with three-photon excitation. *Science* **275,** 530–532 (1997).
8. Horton, N. G. *et al.* In vivo three-photon microscopy of subcortical structures within an intact mouse brain. *Nat. Photonics* **7,** 205–209 (2013).
9. Hell, S. W. & Wichmann, J. Breaking the diffraction resolution limit by stimulated emission: stimulated-emission-depletion fluorescence microscopy. *Opt. Lett.* **19,** 780–782 (1994).
10. Dickson, R. M., Cubitt, A. B., Tsien, R. Y. & Moerner, W. E. On/off blinking and switching behaviour of single molecules of green fluorescent protein. *Nature* **388,** 355–358 (1997).
11. Betzig, E. *et al.* Imaging intracellular fluorescent proteins at nanometer resolution. *Science* **313,** 1642–1645 (2006).
12. Schermelleh, L., Heintzmann, R. & Leonhardt, H. A guide to super-resolution fluorescence microscopy. *J. Cell Biol.* **190,** 165–175 (2010).

13. Vellekoop, I. M. & Mosk, A. P. Focusing coherent light through opaque strongly scattering media. *Opt. Lett.* **32,** 2309–2311 (2007).

14. Vellekoop, I. M. & Mosk, A. P. Universal optimal transmission of light through disordered materials. *Phys. Rev. Lett.* **101,** 120601 (2008).

15. Popoff, S. M., Lerosey, G., Fink, M., Boccara, A. C. & Gigan, S. Image transmission through an opaque material. *Nat. Commun.* **1,** 81 (2010).

16. Bertolotti, J. *et al.* Non-invasive imaging through opaque scattering layers. *Nature* **491,** 232–234 (2012).

17. Horstmeyer, R., Ruan, H. & Yang, C. Guidestar-assisted wavefront-shaping methods for focusing light into biological tissue. *Nat. Photonics* **9,** 563–571 (2015).

18. Xu, X., Liu, H. & Wang, L. V. Time-reversed ultrasonically encoded optical focusing into scattering media. *Nat. Photonics* **5,** 154–157 (2011).

19. Judkewitz, B., Wang, Y. & Horstmeyer, R. Speckle-scale focusing in the diffusive regime with time reversal of variance-encoded light (TROVE). *Nat. Photonics* **7,** 300–305 (2013).

20. Zada, G., Liu, C. & Apuzzo, M. L. J. "Through the looking glass": Optical physics, issues, and the evolution of neuroendoscopy. *World Neurosurg.* **79,** S3–S13 (2013).

21. Di Ieva, A., Tam, M., Tschabitscher, M. & Cusimano, M. D. A journey into the technical evolution of neuroendoscopy. *World Neurosurg.* **82,** E777–E789 (2014).

22. Hopkins, H. H. & Kapany, N. S. A flexible fibrescope, using static scanning. *Nature* **173,** 39–41 (1954).

23. Čižmár, T. & Dholakia, K. Exploiting multimode waveguides for pure fibre-based imaging. *Nat. Commun.* **3,** 1027 (2012).

24. Choi, Y. *et al.* Scanner-free and wide-field endoscopic imaging by using a single multimode optical fiber. *Phys. Rev. Lett.* **109,** 203901 (2012).

25. Papadopoulos, I. N., Farahi, S., Moser, C. & Psaltis, D. High-resolution, lensless endoscope based on digital scanning through a multimode optical fiber. *Biomed. Opt. Express* **4,** 260–270 (2013).

26. Di Leonardo, R. & Bianchi, S. Hologram transmission through multi-mode optical fibers. *Opt. Express* **19,** 247–254 (2011).

27. Čižmár, T. & Dholakia, K. Shaping the light transmission through a multimode optical fibre: complex transformation analysis and applications in biophotonics. *Opt. Express* **19,** 18871–18884 (2011).

28. Papadopoulos, I. N., Farahi, S., Moser, C. & Psaltis, D. Focusing and scanning light through a multimode optical fiber using digital phase conjugation. *Opt. Express* **20,** 10583–10590 (2012).

29. Plöschner, M. *et al.* Multimode fibre: Light-sheet microscopy at the tip of a needle. *Sci. Rep.* **5,** 18050 (2015).

30. Gusachenko, I., Chen, M. & Dholakia, K. Raman imaging through a single multimode fibre. *Opt. Express* **25,** 13782–13798 (2017).

31. Loterie, D. *et al.* Digital confocal microscopy through a multimode fiber. *Opt. Express* **23,** 23845–23858 (2015).

32. Morales-Delgado, E. E., Psaltis, D. & Moser, C. Two-photon imaging through a multimode fiber. *Opt. Express* **23,** 32158–32170 (2015).

33. Morales-Delgado, E. E. *et al.* Three-dimensional microfabrication through a multimode optical fiber. *Opt. Express* **25,** 7031–7045 (2017).

34. Delrot, P., Loterie, D., Psaltis, D. & Moser, C. Single-photon three-dimensional microfabrication through a multimode optical fiber. *Opt. Express* **26,** 1766–1778 (2018).

35. Bianchi, S. & Di Leonardo, R. A multi-mode fiber probe for holographic micromanipulation and microscopy. *Lab Chip* **12,** 635–639 (2012).

36. Snyder, A. W. & Love, J. D. *Optical Waveguide Theory* (Chapman and Hall, London, 1983).

37. Okamoto, K. *Fundamentals of Optical Waveguides* (Academic Press, 2005).

38. Plöschner, M., Tyc, T. & Čižmár, T. Seeing through chaos in multimode fibres. *Nat. Photonics* **9,** 529–535 (2015).

39. Vos, W. L., Lagendijk, A. & Mosk, A. P. in *Light Localisation and Lasing: Random and Quasi-random Photonic Structures* (eds Ghulinyan, M. & Pavesi, L.) chap. 1 (Cambridge).

40. Mosk, A. P., Lagendijk, A., Lerosey, G. & Fink, M. Controlling waves in space and time for imaging and focusing in complex media. *Nat. Photonics* **6,** 283–292 (2012).

41. Conkey, D. B., Caravaca-Aguirre, A. M. & Piestun, R. High-speed scattering medium characterization with application to focusing light through turbid media. *Opt. Express* **20,** 1733–1740 (2012).

42. Cui, M. & Yang, C. Implementation of a digital optical phase conjugation system and its application to study the robustness of turbidity suppression by phase conjugation. *Opt. Express* **18,** 3444–3455 (2010).

43. Popoff, S. M. *et al.* Measuring the transmission matrix in optics: An approach to the study and control of light propagation in disordered media. *Phys. Rev. Lett.* **104,** 100601 (2010).

44. Popoff, S. M., Lerosey, G., Fink, M., Boccara, A. C. & Gigan, S. Controlling light through optical disordered media: Transmission matrix approach. *New J. Phys.* **13,** 123021 (2011).

45. Amitonova, L. V., Mosk, A. P. & Pinkse, P. W. H. Rotational memory effect of a multimode fiber. *Opt. Express* **23,** 20569–20575 (2015).

46. Morales-Delgado, E. E., Farahi, S., Papadopoulos, I. N., Psaltis, D. & Moser, C. Delivery of focused short pulses through a multimode fiber. *Opt. Express* **23,** 9109–9120 (2015).

47. Ashkin, A., Dziedzic, J. M., Bjorkholm, J. E. & Chu, S. Observation of a single-beam gradient force optical trap for dielectric particles. *Opt. Lett.* **11,** 288–290 (1986).

48. *Optical Tweezers - Methods and Applications* (eds Padgett, M. J., Molloy, J. E. & McGloin, D.) (CRC Press, 2010).

49. Jones, P. H., Maragò, O. M. & Volpe, G. *Optical Tweezers - Principles and Applications* (Cambridge University Press, 2015).

50. Fazal, F. M. & Block, S. M. Optical tweezers study life under tension. *Nat. Photonics* **5,** 318–321 (2011).

51. Svoboda, K. & Block, S. M. Force and velocity measured for single kinesin molecules. *Cell* **77,** 773–784 (1994).

52. Bustamante, C., Macosko, J. C. & Wuite, G. J. L. Grabbing the cat by the tail: Manipulating molecules one by one. *Nat. Rev. Mol. Cell Biol.* **1,** 130–136 (2000).

53. Bustamante, C., Bryant, Z. & Smith, S. B. Ten years of tension: single-molecule DNA mechanics. *Nature* **421,** 423–427 (2003).

54. Grier, D. G. A revolution in optical manipulation. *Nature* **424,** 810–816 (2003).

55. Dholakia, K. & Reece, P. Optical micromanipulation takes hold. *Nano Today* **1,** 18–27 (2006).

56. Padgett, M. & Di Leonardo, R. Holographic optical tweezers and their relevance to lab on chip devices. *Lab Chip* **11,** 1196–1205 (2011).

57. Zhong, M.-C., Wei, X.-B., Zhou, J.-H., Wang, Z.-Q. & Li, Y.-M. Trapping red blood cells in living animals using optical tweezers. *Nat. Commun.* **4,** 1768 (2013).

58. Johansen, P. L., Fenaroli, F., Evensen, L., Griffiths, G. & Koster, G. Optical micromanipulation of nanoparticles and cells inside living zebrafish. *Nat. Commun.* **7,** 10974 (2016).

59. Favre-Bulle, I. A., Stilgoe, A. B., Rubinsztein-Dunlop, H. & Scott, E. K. Optical trapping of otoliths drives vestibular behaviours in larval zebrafish. *Nat. Commun.* **8,** 630 (2017).

60. Constable, A, Kim, J, Mervis, J, Zarinetchi, F & Prentiss, M. Demonstration of a fiber-optical light-force trap. *Opt. Lett.* **18,** 1867–1869 (1993).

61. Ribeiro, R. S. R., Soppera, O., Oliva, A. G., Guerreiro, A. & Jorge, P. A. S. New trends on optical fiber tweezers. *J. Light. Technol.* **33,** 3394–3405 (2015).

62. Liberale, C. *et al.* Miniaturized all-fibre probe for three-dimensional optical trapping and manipulation. *Nat. Photonics* **1,** 723–727 (2007).

63. Berthelot, J. *et al.* Three-dimensional manipulation with scanning near-field optical nanotweezers. *Nat. Nanotechnol.* **9,** 295–299 (2014).

64. Guck, J, Ananthakrishnan, R, Moon, T. J., Cunningham, C. C. & Käs, J. Optical deformability of soft biological dielectrics. *Phys. Rev. Lett.* **84,** 5451–5454 (2000).

65. Guck, J. *et al.* Optical deformability as an inherent cell marker for testing malignant transformation and metastatic competence. *Biophys. J.* **88,** 3689–3698 (2005).

66. Kreysing, M. K. *et al.* The optical cell rotator. *Opt. Express* **16,** 16984–16992 (2008).

67. Kreysing, M. *et al.* Dynamic operation of optical fibres beyond the single-mode regime facilitates the orientation of biological cells. *Nat. Commun.* **5,** 5481 (2014).

68. Maurer, C., Jesacher, A., Bernet, S. & Ritsch-Marte, M. What spatial light modulators can do for optical microscopy. *Laser Photon. Rev.* **5,** 81–101 (2011).

69. Zhang, Z., You, Z. & Chu, D. Fundamentals of phase-only liquid crystal on silicon (LCOS) devices. *Light Sci. Appl.* **3,** e213 (2014).

70. Maurer, C., Schwaighofer, A., Jesacher, A., Bernet, S. & Ritsch-Marte, M. Suppression of undesired diffraction orders of binary phase holograms. *Appl. Opt.* **47,** 3994–3998 (2008).

71. Ren, Y.-X., Lu, R.-D. & Gong, L. Tailoring light with a digital micromirror device. *Ann. Phys.* **527,** 447–470 (2015).

72. Brown, B. R. & Lohmann, A. W. Complex spatial filtering with binary masks. *Appl. Opt.* **5,** 967–969 (1966).

73. Chandrasekaran, S. N., Ligtenberg, H., Steenbergen, W. & Vellekoop, I. M. Using digital micromirror devices for focusing light through turbid media. *Proc. SPIE* **8979,** 897905 (2014).

74. Goorden, S. A., Bertolotti, J. & Mosk, A. P. Superpixel-based spatial amplitude and phase modulation using a digital micromirror device. *Opt. Commun.* **22,** 17999–18009 (2014).

75. Akbulut, D, Huisman, T. J., van Putten, E. G., Vos, W. L. & Mosk, A. P. Focusing light through random photonic media by binary amplitude modulation. *Opt. Express* **19,** 4017–4029 (2011).

76. Caravaca-Aguirre, A. M., Niv, E., Conkey, D. B. & Piestun, R. Real-time resilient focusing through a bending multimode fiber. *Opt. Express* **21,** 12881–12887 (2013).

77. Čižmár, T., Mazilu, M. & Dholakia, K. In situ wavefront correction and its application to micromanipulation. *Nat. Photonics* **4,** 388–394 (2010).

78. Lee, W.-H. Binary computer-generated holograms. *Appl. Opt.* **18,** 3661–3669 (1979).

79. García-Márquez, J., López, V., González-Vega, A. & Noé, E. Flicker minimization in an LCoS spatial light modulator. *Opt. Express* **20,** 8431–8441 (2012).

80. Mitchell, K. J., Turtaev, S., Padgett, M. J., Čižmár, T. & Phillips, D. B. High-speed spatial control of the intensity, phase and polarisation of vector beams using a digital micro-mirror device. *Opt. Express* **24,** 29269–29282 (2016).

81. Yu, H., Lee, K. & Park, Y. Ultrahigh enhancement of light focusing through disordered media controlled by mega-pixel modes. *Opt. Express* **25,** 8036–8047 (2017).

82. Persson, M., Engström, D. & Goksör, M. Reducing the effect of pixel crosstalk in phase only spatial light modulators. *Opt. Express* **20,** 22334–22343 (2012).

83. Gissibl, T., Thiele, S., Herkommer, A. & Giessen, H. Two-photon direct laser writing of compact multi-lens objectives. *Nat. Photonics* **10,** 554–560 (2016).

84. Bianchi, S *et al.* Focusing and imaging with increased numerical apertures through multimode fibers with micro-fabricated optics. *Opt. Lett.* **38,** 4935–4937 (2013).

85. Papadopoulos, I. N., Farahi, S., Moser, C. & Psaltis, D. Increasing the imaging capabilities of multimode fibers by exploiting the properties of highly scattering media. *Opt. Lett.* **38,** 2776–2778 (2013).

86. Choi, Y., Yoon, C., Kim, M., Yang, J. & Choi, W. Disorder-mediated enhancement of fiber numerical aperture. *Opt. Lett.* **38,** 2253–2255 (2013).

87. Wadsworth, W. J. *et al.* Very high numerical aperture fibers. *IEEE Photonics Technol. Lett.* **16,** 843–845 (2004).

88. Issa, N. A. High numerical aperture in multimode microstructured optical fibers. *Appl. Opt.* **43,** 6191–6197 (2004).

89. Schuster, K. *et al. High NA fibers - A comparison of optical , thermal and mechanical properties of ultra low index coated fibers and air clad MOFs* in *Proc. 54th Int. Wire Cable Symp.* (Providence, 2005), 382–387.

90. Amitonova, L. V. *et al.* High-resolution wavefront shaping with a photonic crystal fiber for multimode fiber imaging. *Opt. Lett.* **41,** 497–500 (2016).

91. Savage, J. A. Materials for infrared fibre optics. *Mater. Sci. Reports* **2,** 101–137 (1987).

92. Monro, T. M. & Ebendorff-Heidepriem, H. Progress in microstructured optical fibers. *Annu. Rev. Mater. Res.* **26,** 467–495 (2006).

93. *SCHOTT Zemax catalogue 2017-02-20b*

94. Jiang, X *et al.* Single-mode hollow-core photonic crystal fiber made from soft glass. *Opt. Express* **19,** 15438–15444 (2011).

95. Jiang, X. *et al.* Supercontinuum generation in ZBLAN glass photonic crystal fiber with six nanobore cores. *Opt. Lett.* **41,** 4245–4248 (2016).

96. Ho, K.-P. & Kahn, J. M. Mode-dependent loss and gain: statistics and effect on mode-division multiplexing. *Opt. Express* **19,** 16612–16635 (2011).

97. Richards, B & Wolf, E. Electromagnetic diffraction in optical systems. II. Structure of the image field in an aplanatic system. *Proc. R. Soc. A Math. Phys. Eng. Sci.* **253,** 358–379 (1959).

98. Novotny, L. & Hecht, B. *Principles of Nano-Optics* (Cambridge University Press, Cambridge, 2006).

99. Kramers, H. Brownian motion in a field of force and the diffusion model of chemical reactions. *Physica* **7,** 284–304 (1940).

100. Dholakia, K & Čižmár, T. Shaping the future of manipulation. *Nat. Photonics* **5,** 335–342 (2011).

101. Capitanio, M., Cicchi, R. & Pavone, F. S. Continuous and time-shared multiple optical tweezers for the study of single motor proteins. *Opt. Lasers Eng.* **45,** 450–457 (2007).

102. https://www.nature.com/articles/s41566-017-0053-8{\#}Sec16.

103. Anastasiadi, G., Leonard, M., Paterson, L. & Macpherson, W. N. Fabrication and characterization of machined multi-core fiber tweezers for single cell manipulation. *Opt. Express* **26,** 3557–3567 (2018).

104. Neuman, K. C. & Block, S. M. Optical trapping. *Rev. Sci. Instrum.* **75,** 2787–2809 (2004).

105. Zhang, Z. & Menq, C.-H. Three-dimensional particle tracking with subnanometer resolution using off-focus images. *Appl. Opt.* **47,** 2361–2370 (2008).

106. https://drive.google.com/file/d/1Fm0G3TAIC49LVX6FaEiAtlefkWx1T2a5.

107. Attardo, A., Fitzgerald, J. E. & Schnitzer, M. J. Impermanence of dendritic spines in live adult CA1 hippocampus. *Nature* **523,** 592–596 (2015).

108. Sato, M., Kawano, M., Yanagawa, Y. & Hayashi, Y. In vivo two-photon imaging of striatal neuronal circuits in mice. *Neurobiol. Learn. Mem.* **135,** 146–151 (2016).

109. Phillips, D. B. *et al.* Adaptive foveated single-pixel imaging with dynamic supersampling. *Sci. Adv.* **3,** e1601782 (2017).

110. Duarte, M. F. *et al.* Single-pixel imaging via compressive sampling. *IEEE Signal Process. Mag.* **25,** 83–91 (2008).

111. Ohayon, S., Caravaca-Aguirre, A., Piestun, R. & DiCarlo, J. J. Minimally invasive multimode optical fiber microendoscope for deep brain fluorescence imaging. *Biomed. Opt. Express* **9,** 1492–1509 (2018).

112. López, D *et al. Two-dimensional MEMS array for maskless lithography and wavefront modulation* in *Smart Sensors, Actuators, and MEMS III* **6589** (2007), 65890S.

113. Lapisa, M., Zimmer, F., Niklaus, F., Gehner, A. & Stemme, G. *CMOS-integrable piston-type micro-mirror array for adaptive optics made of monocrystalline silicon using 3-D integration* in *Micro Electro Mechanical Systems, 2009. MEMS 2009. IEEE 22nd International Conference on* (2009), 1007–1010.

114. Boonzajer Flaes, D. E. *et al.* Robustness of light-transport processes to bending deformations in graded-index multimode waveguides. *Phys. Rev. Lett.* **120,** 233901 (2018).

115. Yeh, C. & Shimabukuro, F. I. *The Essence of Dielectric Waveguides* (Springer, 2008).